# Magneto-optical study of semimagnetic semiconductor Cd1-xMnxTe and its application to the study of intermediate-state flux pattern of type-I superconductor thin films

Takanori Okada



# THÈSE

**Spécialité: Physique des Solides**

**présentée par**

**Takanori OKADA**

**pour obtenir le titre de docteur de**

**l'Université Paris VI et de l'Université d'Osaka**

# Magneto-optical study of semimagnetic semiconductor $Cd_{1-x}Mn_xTe$ and its application to the study of intermediate-state flux patterns of type-I superconductor thin films

**Soutenue le 14 Février 2005 devant le jury composé de :**

| | | |
|---|---|---|
| **Mme.** | **Catherine GOURDON** | **Co-directrice de thèse** |
| **M.** | **Tadashi ITOH** | **Co-directeur de thèse** |
| **Mme.** | **Maria CHAMARRO** | **Examinatrice** |
| **M.** | **Shigemasa SUGA** | **Rapporteur** |
| **M.** | **Satoshi HIYAMIZU** | **Rapporteur** |

# Acknowledgements

This thesis contains two parts. The study reported in Part I was done at Graduate School of Engineering Science in Osaka University from March 2001 to May 2002 and from January to September 2003. The study in Part II was carried out at Groupe de Physique des Solides in Université Pierre et Marie Curie -Paris VI from June to December 2002 and from October 2003 to September 2004. The latter research work was done under the auspices of the Leading Student Exchange Support Program Scholarship (2002.6-2002.12) and that of the Japanese Consortium of "College Doctoral Franco-Japonais" (2003.10-2004.9), which were granted by the Japanese Ministry of Education, Culture, Sports, Science and Technology.

First of all I am grateful to my genuine appreciation to Professor Tadashi Itoh, my supervisor at Osaka University, for not only his imaginative advice and discussion but also continuing support and encouragement. He graciously gave me an opportunity to study semimagnetic semiconductor and proofread Part I of this thesis. In addition he also gave me a chance to take interested in going to Paris for the sake of learning the way of study in France.

I would like to express my sincere gratitude to Doctor Catherine Gourdon, my supervisor at Université Pierre et Marie Curie, for her discerning advice and discussion about not only experiments but also calculations. She kindly gave me an opportunity to study superconductors as well as semimagnetic semiconductors as an application device. The guidance of calculations and the proofreading of Part I and Part II of this thesis were supplied by her.

The study in Part II of this thesis was performed with also Doctor Vincent Jeudy, who was responsible for the design and fabrication of the cryostat. His helpful discussions and instruction of the experimental techniques are gratefully acknowledged. He gave me goodwill-advice for not only physical subjects but also measuring devices at Université Pierre et Marie Curie.

I wish to thank Professor Keiichi Edamatsu and Professor Masaaki Ashida for their helpful advice at Osaka University.

Many other members of Itoh laboratory and the laboratory in Groupe de Physique des Solides also provided me useful input.

Finally, I wish to express my heartfelt gratitude to Doctor Philippe Lavallard for proofreading Part I of this thesis and giving me valuable opportunity to work in Paris.

# Contents

# Part I

# Magneto-optical study of localized and bound excitons in semimagnetic semiconductor $Cd_{1-x}Mn_xTe$

# Chapter 1

# Introduction

A semimagnetic semiconductor, also called a diluted magnetic semiconductor, is a compound semiconductor with diluted magnetic ions. Semimagnetic semiconductor enables us to tune not only its lattice constant and band parameters but also magnetic characteristics by varying the composition of the material. Hence, this compound semiconductor is quite interesting to study as both semiconducting and magnetic materials. The most actively studied semimagnetic semiconductors are the ternary materials having magnetic ions in its cation sites, e.g. $A^{III}_{1-x}TM_xB^{V}$ (TM indicates transition metal) and $A^{II}_{1-x}TM_xB^{VI}$. For the past twenty years many researchers have devoted to study $A^{II}_{1-x}Mn_xB^{VI}$ including $Cd_{1-x}Mn_xTe$ [1][2].

Physical properties of semimagnetic semiconductors $A^{II}_{1-x}Mn_xB^{VI}$ are characterized by the combination of usual semiconductor mixed-crystal effects with special properties caused by the half-filled $3d$-shell of $Mn^{2+}$ cations. According to virtual crystal approximation the alloy potential should fluctuate, which is essential since it leads to the intrinsic localization of photoexcited excitons in these mixed compounds. The most important physical properties are based on the strong $sp$-$d$ exchange interaction between $5s$-electron or $5p$-hole band states and the $Mn^{2+}$ $3d$-electron states. Due to this exchange interaction the effective $g$-factor of $A^{II}_{1-x}Mn_xB^{VI}$ can be enhanced up to two orders of magnitude larger than that of $A^{II}B^{VI}$. Then this exchange interaction leads to magneto-optical effects such as giant Zeeman splitting of valence and conduction band[3][4][5][6], giant Faraday rotation[7][8][9][10][11][12][13], photo-induced magnetization[14][15][16], and formation of magnetic polarons[17][18][19][20]. In addition, lots of curious phenomena are reported, e.g. photomemory effect[21] and stimulated emission[22][23][24]. For that reason semimagnetic semiconductor alloys are used in practice as isolators, variable-

wavelength solid laser media, and infrared detectors.

The crystal structure of $A^{II}_{1-x}Mn_xB^{VI}$ semimagnetic semiconductor is zincblende or wurtzite type. Ternary alloys formed by substituting Mn for the group II element in the $A^{II}B^{VI}$ lattice retain the crystal structure of the parent $A^{II}B^{VI}$ compound. The lattice parameters of all semimagnetic semiconductor ternary alloys obey Vegard's law. $Cd_{1-x}Mn_xTe$ bulk crystal exhibits the zincblende type structure for $x \leq 0.77$. The lattice constant $a(x)$ of $Cd_{1-x}Mn_xTe$ is expressed as:

$$a(x) = 6.487 - 0.149x \qquad [\text{Å}]. \tag{1.1}$$

Above $x = 0.77$ $Cd_{1-x}Mn_xTe$ forms an eutectic.

Because of the tunability of its lattice parameter and its energy gap, the semimagnetic semiconductors are an excellent candidate for the fabrication of nanostructures[25][26] such as quantum wells[27][28][29], quantum wires[30][31], and quantum dots[30]. These nanostructures of the semimagnetic semiconductors are very interesting to study for its applications because the combination of strong confinement and *sp-d* exchange interaction may result in unusual magneto-optical properties[32]. In recent years, semimagnetic semiconductors have proven to be very useful in building an all-semiconductor platform for spintronics, e.g. the injection of spin-polarized electrons into a nonmagnetic semiconductor[33][34] or a light emitting diode[35].

## 1.1 Band structure

Generally the optical properties of $Cd_{1-x}Mn_xTe$ are characterized at the center of the Brillouin zone ($\Gamma$ point) because $Cd_{1-x}Mn_xTe$ is a direct transition semiconductor. Fig. 1.1 shows the vicinity of $\Gamma$ point of the band structure.

With zero magnetic field, the conduction band ($\Gamma_6$, $5s$ orbit) is twofold degenerate ($J = 1/2$). The spin-orbit coupling splits the valence band ($5p$ orbit) into two energy levels. The upper valence band is fourfold degenerate ($\Gamma_8$, $J = 3/2$) which is composed of heavy holes ($m_J = \pm 3/2$) and light holes ($m_J = \pm 1/2$), and the lower band is twofold ($\Gamma_7$, $J = 1/2$). The energy of spin-orbit interaction is $\Delta_{so} = E_{\Gamma_8} - E_{\Gamma_7} = 0.91$ eV (for CdTe). The energy of the forbidden gap $E_g(x)$ increases linearly with increasing Mn composition as:

$$E_g(4.2\text{K}) = E_{\Gamma_6} - E_{\Gamma_8} = 1.606 + 1.592x \qquad [\text{eV}]. \tag{1.2}$$

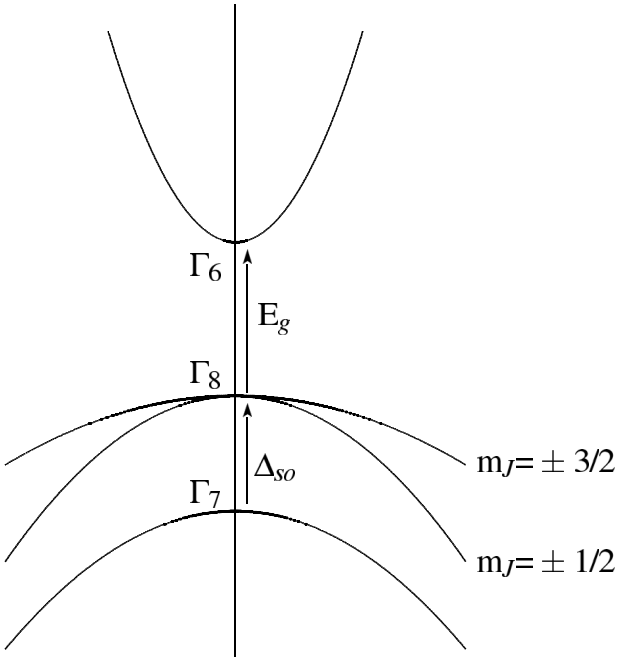


Figure 1.1: Schematic band structure in the vicinity of Γ point of $Cd_{1-x}Mn_xTe$ bulk crystal.

The binding energy of the exciton is 10 meV (for CdTe).

The electrons of the half-filled $3d^5$ are localized around the $Mn^{2+}$ ions. The ground state of the free ion is sixfold degenerate ($^6S_{5/2}$, $L=0$, $S=5/2$). In $Cd_{1-x}Mn_xTe$ $Mn^{2+}$ ions show a paramagnetic behavior[36][37] described by a Brillouin function. The Landé $g$-factor $g_{\mathrm{Mn}}=2$.

## 1.2 Exchange interaction of band electrons

The *sp-d* exchange interaction between the band electron spins (5*s* or 5*p* orbit) and the $Mn^{2+}$ spins (3*d* orbit) contributes to the giant Zeeman effect of valence and conduction band with magnetic field. Such interaction can be described phenomenologically by a Heisenberg type Hamiltonian $H_{sp-d}$[38] as:

$$H_{sp-d}=\sum_{\vec{R}_i} J^{sp-d}(\vec{r}-\vec{R}_i)\vec{S}_i\cdot\vec{\sigma}, \tag{1.3}$$

where $\vec{S}_i$ and $\vec{\sigma}$ are the spin operators of the $Mn^{2+}$ ion on the lattice site $\vec{R}_i$ and of the band electron at $\vec{r}$, respectively. $J^{sp-d}$ is the electron-ion *sp-d* exchange interaction energy and the summation is taken over all $Mn^{2+}$ ions. Since the electronic wave function is rather

extended, the electron can interact with a large number of $Mn^{2+}$ ions. Hence by usual mean-field approximation and virtual-crystal approximation, $\vec{S}_i$ can be replaced by the thermal average value $\langle\vec{S}\rangle$, and $J^{sp-d}(\vec{r}-\vec{R}_i)$ is substituted by $xJ^{sp-d}(\vec{r}-\vec{R})$. Therefore Eq. (1.3) is written as:

$$H_{sp-d} = x\sum_{\vec{R}} J^{sp-d}(\vec{r}-\vec{R})\langle\vec{S}\rangle\cdot\vec{\sigma}, \tag{1.4}$$

where the summation is taken over all fcc cation-sublattice sites $\vec{R}$. If the applied magnetic field $\vec{B}$ is in the $z$ direction, $\langle\mathbf{S}\rangle = \langle S_z\rangle$, then Eq. (1.4) is expressed as:

$$H_{sp-d} = x\sum_{\vec{R}} J^{sp-d}(\vec{r}-\vec{R})\langle S_z\rangle\cdot\sigma_z \quad \text{and} \quad \langle S_x\rangle = \langle S_y\rangle = 0, \tag{1.5}$$

where $\sigma_z$ is $z$ component of $\vec{\sigma}$. Since $H_{sp-d}$ has the same periodicity as CdTe lattice, the wave function for band electrons in $Cd_{1-x}Mn_xTe$ are expressed with that of CdTe. Then for $\Gamma_6$ conduction band[39],

$$\begin{aligned}
\left|\frac{1}{2},+\frac{1}{2}\right\rangle_{\Gamma_6} &= |S\uparrow\rangle \\
\left|\frac{1}{2},-\frac{1}{2}\right\rangle_{\Gamma_6} &= |S\downarrow\rangle,
\end{aligned} \tag{1.6}$$

for $\Gamma_8$ valence band,

$$\begin{aligned}
\left|\frac{3}{2},+\frac{3}{2}\right\rangle_{\Gamma_8} &= \frac{1}{\sqrt{2}}|(X+iY)\uparrow\rangle \\
\left|\frac{3}{2},+\frac{1}{2}\right\rangle_{\Gamma_8} &= \frac{1}{\sqrt{6}}i|(X+iY)\downarrow -2Z\uparrow\rangle \\
\left|\frac{3}{2},-\frac{1}{2}\right\rangle_{\Gamma_8} &= \frac{1}{\sqrt{6}}|(X-iY)\uparrow +2Z\downarrow\rangle \\
\left|\frac{3}{2},-\frac{3}{2}\right\rangle_{\Gamma_8} &= \frac{1}{\sqrt{2}}i|(X-iY)\downarrow\rangle,
\end{aligned} \tag{1.7}$$

and for $\Gamma_7$ valence band,

$$\begin{aligned}
\left|\frac{1}{2},+\frac{1}{2}\right\rangle_{\Gamma_7} &= -\frac{1}{\sqrt{3}}i|(X-iY)\uparrow -Z\downarrow\rangle \\
\left|\frac{1}{2},-\frac{1}{2}\right\rangle_{\Gamma_7} &= \frac{1}{\sqrt{3}}|(X+iY)\downarrow +Z\uparrow\rangle.
\end{aligned} \tag{1.8}$$

With the above base wave functions of band electron $|\vec{J},m_j\rangle$, the matrix elements are obtained as:

$$H_{sp-d}^{\Gamma_6} = \begin{pmatrix} A & 0 \\ 0 & -A \end{pmatrix}, \tag{1.9}$$

$$H_{sp-d}^{\Gamma_8} = \begin{pmatrix} 3B & 0 & 0 & 0 \\ 0 & B & 0 & 0 \\ 0 & 0 & -B & 0 \\ 0 & 0 & 0 & -3B \end{pmatrix}, \tag{1.10}$$

$$H_{sp-d}^{\Gamma_7} = \begin{pmatrix} B & 0 \\ 0 & -B \end{pmatrix}, \tag{1.11}$$

where $A = \frac{1}{2}N_0\alpha x\langle S_z\rangle$ and $B = \frac{1}{6}N_0\beta x\langle S_z\rangle$. $N_0\alpha$ and $N_0\beta$ are exchange integrals of $s$ and $p$ band, respectively. $N_0$ is the number of cations per unit volume. The coupling is ferromagnetic for $s$- and $d$-electrons and antiferromagnetic for $p$- and $d$-electrons. The exchange integrals for $Cd_{1-x}Mn_xTe$ are

$$\begin{aligned} N_0\alpha &= +0.22 \quad [\text{eV}] \\ N_0\beta &= -0.88 \quad [\text{eV}]. \end{aligned} \tag{1.12}$$

Therefore, the degeneracy of conduction and valence bands is lifted by the $sp$-$d$ exchange interaction with an applied magnetic field. This is called the "giant Zeeman effect". For example it can be calculated that the amplitude of Zeeman splitting for the valence band is 40 meV at $x = 0.2$ (see Appendix A.1).

The selection rule of interband transitions in Faraday geometry is $\Delta m_J = +1$ for circular polarization $\sigma^+$, and $\Delta m_J = -1$ for $\sigma^-$. The transition energies and relative oscillator strengths for $\Gamma_8 \rightarrow \Gamma_6$ in the presence of $sp$-$d$ exchange interaction are shown in Table 1.1. A schematic representation of the Zeeman splitting due to exchange interaction for electronic conduction band and heavy hole valence band is shown in Fig. 1.2 in case of zincblende symmetry.

The average value of $Mn^{2+}$ ion spins for $Cd_{1-x}Mn_xTe$ is given as:

$$\langle S_z\rangle = -S_{\text{eff}}(x)B_{5/2}\left(\frac{5}{2}\frac{g_{\text{Mn}}\mu_B B}{k_B(T+T_0)}\right), \tag{1.13}$$

where

$$B_{5/2}(u) = \frac{6}{5}\coth\left(\frac{6}{5}u\right) - \frac{1}{5}\coth\left(\frac{1}{5}u\right), \tag{1.14}$$

is the Brillouin function for spin $S = 5/2$ (see Appendix A.1), and

Table 1.1: Characteristics of $\Gamma_8 \to \Gamma_6$ transitions in the zincblende type semimagnetic semiconductor bulk crystal. $E_g$ is written in Eq. (1.2).

| Transition | Energy | Polarization | Probability |
|---|---|---|---|
| $\lvert\frac{3}{2},-\frac{3}{2}\rangle \to \lvert\frac{1}{2},-\frac{1}{2}\rangle$ | $E_g - \frac{1}{2}N_0(\alpha - \beta)x\langle S_z\rangle$ | $\sigma^+$ | 3 |
| $\lvert\frac{3}{2},-\frac{1}{2}\rangle \to \lvert\frac{1}{2},\frac{1}{2}\rangle$ | $E_g + \frac{1}{2}N_0(\alpha + \frac{1}{3}\beta)x\langle S_z\rangle$ | $\sigma^+$ | 1 |
| $\lvert\frac{3}{2},\frac{1}{2}\rangle \to \lvert\frac{1}{2},-\frac{1}{2}\rangle$ | $E_g - \frac{1}{2}N_0(\alpha + \frac{1}{3}\beta)x\langle S_z\rangle$ | $\sigma^-$ | 1 |
| $\lvert\frac{3}{2},\frac{3}{2}\rangle \to \lvert\frac{1}{2},\frac{1}{2}\rangle$ | $E_g + \frac{1}{2}N_0(\alpha - \beta)x\langle S_z\rangle$ | $\sigma^-$ | 3 |

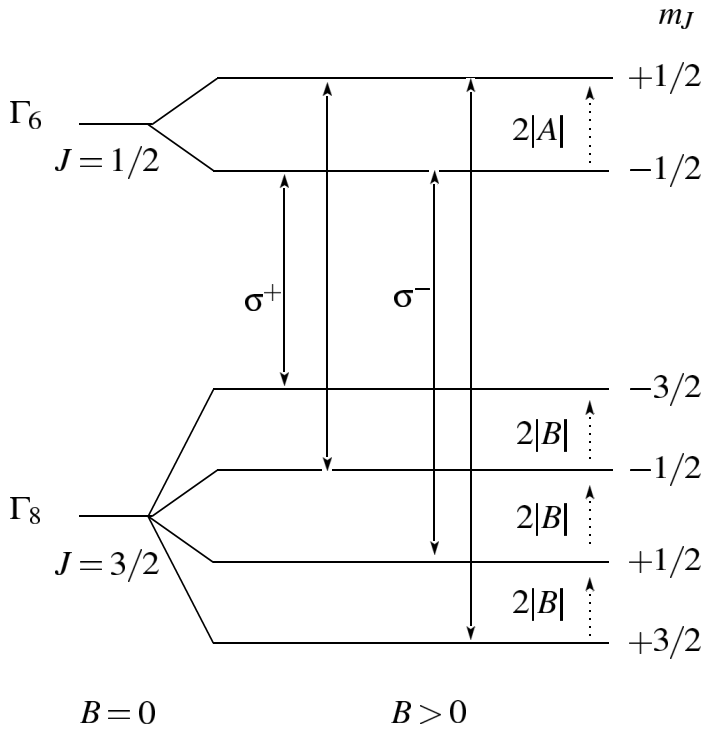


Figure 1.2: A schematic picture of the spin splitting of the top valence band ($\Gamma_8$) and the bottom conduction band ($\Gamma_6$) in Faraday geometry.

$$
\begin{aligned}
T_0(x) &= \frac{35.37}{1+2.752x}x \qquad [\mathrm{K}] \\
S_{\mathrm{eff}}(x) &= \frac{5}{2}[0.265\exp(-43.34x)+0.735\exp(-6.19x)],
\end{aligned}
\tag{1.15}
$$

are deduced from actual measurements of the Zeeman splitting in bulk alloys[40][41] (see Appendix A.2), $g_{\mathrm{Mn}}(=2)$ is the $g$-factor of $Mn^{2+}$, $\mu_B(=58\,\mu\mathrm{eV/T})$ is the Bohr magneton, $k_B(=86.17\,\mu\mathrm{eV/K})$ is the Boltzmann constant, $B$ is the value of magnetic field, and $T$ is the temperature. It is important to note that an antiferromagnetic $Mn^{2+}$- $Mn^{2+}$ exchange interaction can not be negligible in case of Mn composition $x > 0.05$. This exchange interaction is achieved with mediating by the two valence band holes[42]. These effects are taken into account in $T_0(x)$ and $S_{\mathrm{eff}}(x)$ (Eq. (1.15)) that are experimentally obtained. Moreover, for $x > 0.25$ at low temperature, the spin-glass phase appears[43][44][45]. Then Zeeman splitting value of the energy levels can be obtained with Table 1.1 and Eq. (1.12) - (1.15).

## 1.3 Magnetic polaron

In some paramagnetic materials the spins could be aligned to form ferromagnetic domains even in the absence of external magnetic field under certain physical conditions. Such ferromagnetically aligned spin of magnetic ions in the vicinity of carriers as illustrated in Fig. 1.3 is called as magnetic polaron (MP).

In case of semimagnetic semiconductor medium, electrons, holes, or excitons would play the role of carriers. An electron gains the total energy by aligning the surrounding magnetic spins. This is ascribed to exchange interaction expressed by Eq. (1.3). In optical experiment, MP formation due to exciton is mainly classified into two categories by different localization mechanisms. One is free/self-trapped exciton magnetic polaron or localized exciton magnetic polaron (EMP) by the alloy potential fluctuation (APF) which is caused by randomly distributed magnetic ions substituted in the host materials. The second is bound exciton magnetic polaron (BMP) to some impurities by Coulomb interaction. A large number of papers observing BMP have been published using various optical spectroscopic techniques, e.g. time-resolved photoluminescence[46]. EMP and

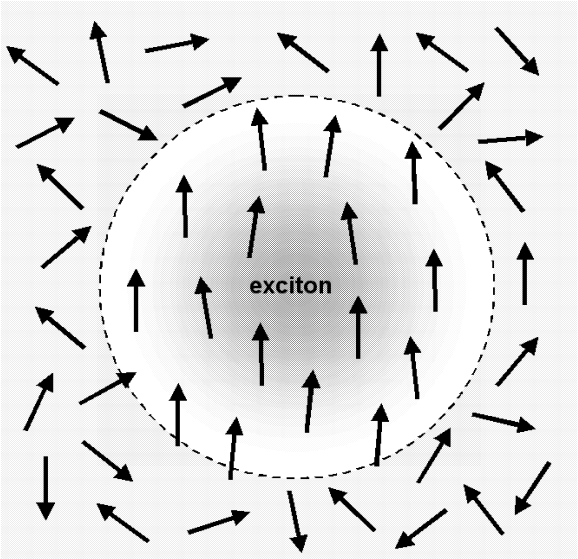


Figure 1.3: Schematic drawing of EMP. The description of EMP is explained in text. Exciton aligned the magnetic ion spins (arrow) inside the Bohr radius (dotted circle).

BMP are created by polarizing the magnetic ion spins inside the exciton coherence length (typically the Bohr radius) as sketched in Fig. 1.3.

The most interesting problem is the mechanism of exciton localization process induced by MP formation and APF. Many authors have discussed for this subject[47][48][49][50][51][52].

# Chapter 2

# Motivation and purpose

One of the outstanding problems that have recently gained attention is the photo-induced magnetic-phase transition in semimagnetic semiconductors including $Cd_{1-x}Mn_xTe$. The localization of excitons induces alignment of the magnetic spins inside the exciton's Bohr radius, resulting in the formation of EMP bound to alloy potential well or impurity. Due to this mechanism, it is theoretically predicted that large ferromagnetic regions should be generated under high power excitation. However, this phase transition has not yet been realized by optical pumping. Therefore it should be of utmost importance to reconsider the mechanism of exciton and/or bound MP formation. Especially a central problem of semimagnetic semiconductor is the mechanism of exciton localization process induced by MP formation and APF. For this reason $Cd_{0.8}Mn_{0.2}Te$ is suitable for the specimen because the localization energy due to MP effect would be large.

For the above reasons we studied the photoluminescence by varying several physical parameters. We first found that the dominant peak spectrum under band-to-band excitation contains two components in $Cd_{0.8}Mn_{0.2}Te$. Photoluminescence at higher energy than the excitation energy was also found at low temperature. By analogy with phonon-assisted transitions it will be called anti-Stokes photoluminescence in the following. This anti-Stokes photoluminescence is observed under excitation at energies lower than the dominant peak energy of the photoluminescence observed under band-to-band excitation.

The origin of two components of the photoluminescence under band-to-band excitation and the mechanism of the anti-Stokes photoluminescence are not fully understood yet. In order to make them clear we study the photoluminescence of $Cd_{0.8}Mn_{0.2}Te$ single crystal in detail. The purpose of our studies is to explain the process of exciton localiza-

tion and to apply its model to unique phenomena, e.g. anti-Stokes photoluminescence. The present work is in that direction.

# Outline

The outline of this study is as follows. Chap. 3 mentions the research plan and Chap. 4 describes the sample and experimental set-up used in this experiment. Chap. 5 is the central chapter of this Part. Sec. 5.1 presents the features of photoluminescence without magnetic field (Sec. 5.1.1) and unique profiles of the photoluminescence with magnetic field (Sec. 5.1.2) in $Cd_{0.8}Mn_{0.2}Te$. In these two sections it is shown that the photoluminescence consists of two components and we propose that they are due to recombination of EMP and $A^0$XBMP. Sec. 5.2 briefly reviews the calculation for Zeeman splitting of exciton and $A^0$X with *sp-d* exchange interaction in semimagnetic semiconductor single crystal. We also qualitatively notice the properties of $A^0$X in $Cd_{1-x}Mn_xTe$ (CdTe). Sec. 5.3 provides the comparison between the experimental results and theoretical predictions. We discuss the mechanism of the spectrum containing two components and deduce the physical exchange constant of deep $A^0$. Sec. 5.4 is devoted to the study of anti-Stokes photoluminescence. The characteristics of the anti-Stokes photoluminescence are explained as a function of excitation energy, excitation power, and magnetic field. It is very important to take into account the absorption of excitation light and reabsorption of anti-Stokes photoluminescence. Therefore this section is divided into two different situations; non-resonant excitation (Sec. 5.4.1) and resonant excitation (Sec. 5.4.2). Chap. 6 gives a summary of the results and significance of the studies.

# Chapter 3

# Research plan

In recent years a lot of studies for nano-structures in semimagnetic semiconductor have been performed. As one of the interesting phenomena in heterostructures containing $Cd_{1-x}Mn_xTe$ quantum well Faraday rotation may be further enhanced mainly due to the large excitonic oscillator strength and possibly the difference of oscillator strength for $\sigma^+$ and $\sigma^-$ circular polarizations. On the other hand the interesting phenomena in semimagnetic semiconductor bulk crystal, e.g. photo-induced magnetization for which we are looking, are also expected for application. In order to realize this aim it is necessary to grasp clearly the mechanism of exciton localization that is not yet solved essentially. The key to the solution of this problem is to elucidate the double peaks of photoluminescence in $Cd_{0.8}Mn_{0.2}Te$ bulk crystal. Besides the above context, other curious phenomena anti-Stokes photoluminescence are studied. Therefore we study the photoluminescence under band-to-band excitation and anti-Stokes photoluminescence under various physical parameters. In the study of semimagnetic semiconductor it is important to study the magnetic field dependence of the photoluminescence because of the existence of *sp-d* exchange interaction. For anti-Stokes photoluminescence it is essential to measure the excitation power and the excitation energy dependences in order to make its mechanism clear. Moreover, it is also important to compare the behavior of the anti-Stokes photoluminescence with that of the photoluminescence under band-to-band excitation. In addition, the study of anti-Stokes photoluminescence under resonant excitation is interesting. Accordingly our research plan consists as follows.

1. Setup and optimization of the optical systems.

2. Measurement of the temperature dependence of the photoluminescence under band-to-band excitation.

3. Measurement of the magnetic field dependence of the photoluminescence under band-to-band excitation and the anti-Stokes photoluminescence.

4. Measurement of the excitation power dependence of the anti-Stokes photoluminescence.

5. Measurement of the excitation energy dependence of the anti-Stokes photoluminescence.

6. Measurement of the photoluminescence behavior under resonant excitation.

7. Measurement of the time-resolved photoluminescence.

Through the analysis of the photoluminescence spectra, we will discuss the origin of the two components of the photoluminescence and the mechanism leading to anti-Stokes photoluminescence.

# Chapter 4

# Experiments

## 4.1 Sample

A single crystal of $Cd_{0.8}Mn_{0.2}Te$ was grown by Bridgman method. The samples were obtained by cleaving the middle part of a cylindrical $Cd_{0.8}Mn_{0.2}Te$ ingot perpendicular to its axes. The samples were chosen among those that exhibit a large dominant photoluminescence. The size is 2.5 mm $\times$ 2.5 mm $\times$ 0.5 mm. No surface treatment, e.g. polishing or etching in a bromine-methanol solution, was done.

The sample was fixed on the deoxidized copper plate (10 mm $\times$ 10 mm $\times$ 1mm) with Apiezon grease in order to get good thermal conductivity. The deoxidized copper plate was fixed on the sample holder with putting fresh indium between them. Here we have to note that the applied magnetic field was much more than the critical magnetic field of indium (28.3 mT). Therefore it was not possible that indium expels the magnetic field.

## 4.2 Optical system for measurements

Fig. 4.1 shows the optical setup for measurement of time-integrated photoluminescence.

Dye laser (dye solution is DCM) pumped by all lines of argon-ion laser is used as a light source to excite the sample for $\lambda_{ex}$ = 600 - 690 nm and Ti-Sapphire laser for $\lambda_{ex}$ = 690 - 900 nm. For band-to-band excitation the second harmonic of Nd:$YVO_4$ laser (532 nm) was also used as an excitation source. In case of reflection measurements the sample is illuminated with the white light of the tungsten lamp passing through the iris. In case of measurements with circular-polarized excitation source a polarizer and a quarter-wave plate are placed before the sample. The light source was put perpendicular to the surface of the sample. The spot size focused on the sample was 0.5 $mm^2$. All lenses in

the optical setup are achromatic. The power of the beam was limited to avoid heating of the sample.

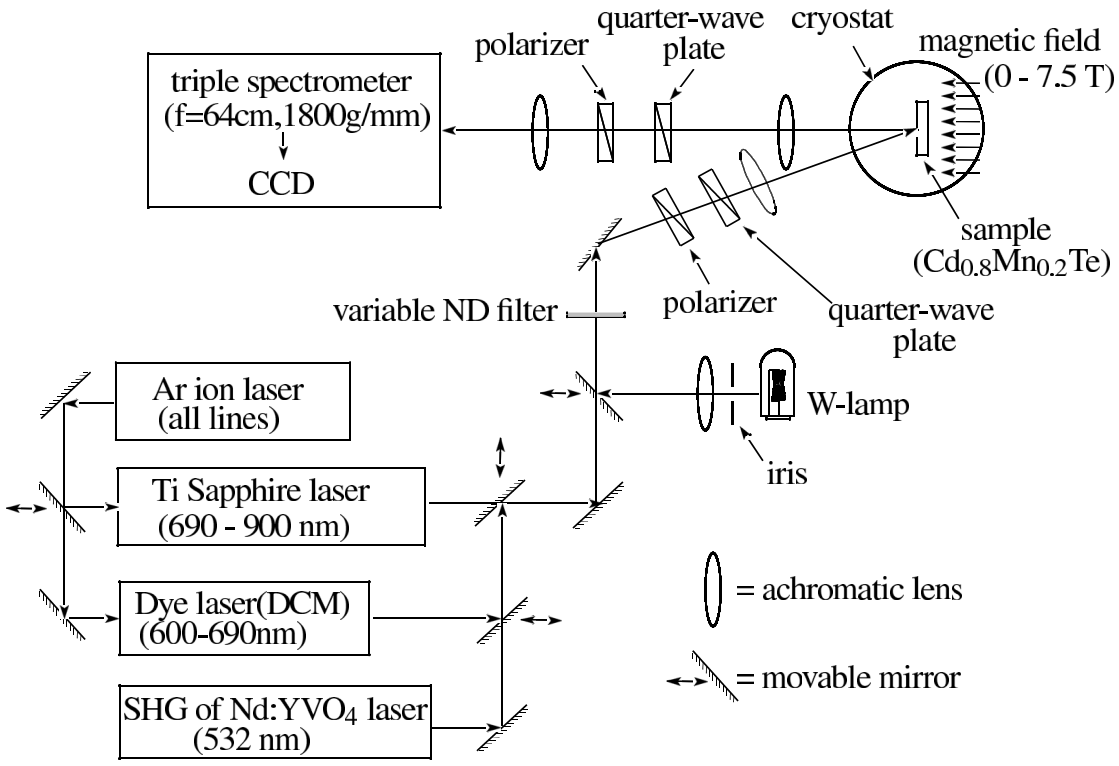


Figure 4.1: Experimental setup for measurement of time-integrated photoluminescence.

The sample was mounted inside the cryostat. This cryostat is equipped with a superconducting-coil magnet that can give a magnetic field up to 7.5 T parallel to the wave vector of light source (Faraday geometry). The temperature of a sample was adjustable from 300 K to 1.8 K with the continuous-flow liquid helium and a heater. The temperature was monitored with semiconducting sensor installed near the sample.

The backward photoluminescence from the sample passed through a quarter-wave plate and a polarizer in order to separate the $\sigma^+$, $\sigma^-$ circular polarization. The photoluminescence was recorded by using a CCD (charge-coupled device) array cooled to liquid-nitrogen temperature, after passing through a spectrometer (the focal length is 64 cm, the grating has 1800 grooves/mm). The triple-spectrometer can cut laser light in case of selective excitation measurements. The spectral resolution was better than 0.1 nm (0.3 meV). Since the spectrum is modified by the inhomogeneous sensitivity of CCD sensor

array and grating, a tungsten lamp was also used for the correction of photoluminescence intensity.

In Sec. 5.1.1 the time evolution of photoluminescence is reported, therefore the time-resolved experimental set up should be here mentioned briefly. The layout of optical components for time-resolved measurement is the same as shown in Fig. 4.1 except the light source and the detector. The time-resolved experiments are performed by using the second harmonic (the crystal is $LiB_3O_5$) of the 76 MHz mode-locked Ti-sapphire laser. As a detector a streak camera working in singlescan mode was used. The time resolution was 10 ps.

# Chapter 5

# Results and discussions

## 5.1 Photoluminescence under band-to-band excitation

In this section we show the photoluminescence of $Cd_{0.8}Mn_{0.2}Te$ under band-to-band excitation and discuss its new mechanism of MP. Universally the photoluminescence of $Cd_{0.8}Mn_{0.2}Te$ is reported to be due to recombination of localized EMP. However, the unique profile of photoluminescence indicates the mechanism is not so simple. Therefore we recall photoluminescence under band-to-band excitation with basic measurements.

### 5.1.1 Photoluminescence without magnetic field

First we show in Fig. 5.1 the profiles of the stationary photoluminescence spectra of EMPs (excitons) in $Cd_{1-x}Mn_xTe$ without magnetic field at various Mn compositions. The peak intensity is normalized with dominant peak intensity. $E_x$ is free exciton energy determined from the exciton-reflection spectrum.

In case of $x = 0$, namely, CdTe three photoluminescence lines, bound exciton to neutral acceptor ($A^0X$), bound exciton to neutral donor ($D^0X$), and free exciton can be observed. In case of mixed crystals with $Mn^{2+}$ ions the photoluminescence is dominated by two features attributed to recombination of $A^0X$BMP and EMP recombination at Mn compositions $x$ smaller than 0.1, while at $x = 0.2$ shows a peak arising from only EMP peak. Here it can be noted that few donor impurities exist in this sample. The photoluminescence spectrum of $Cd_{0.8}Mn_{0.2}Te$ shows peculiar behavior as a function of temperature.

Fig. 5.2 shows the stationary photoluminescence spectra of excitons under band-to-band excitation in $Cd_{0.8}Mn_{0.2}Te$ without magnetic field at various temperatures. The

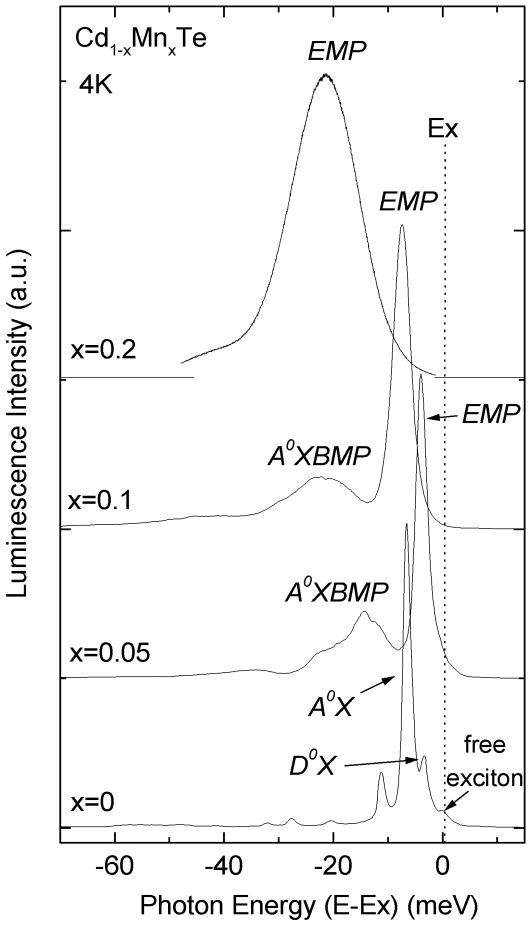


Figure 5.1: Stationary photoluminescence spectra of excitons in $Cd_{1-x}Mn_xTe$ without magnetic field at various Mn composition. The peak intensity is normalized with dominant peak intensity. *Ex* is free exciton energy determined from the exciton-reflection spectrum. The description of $A^0X$ and $D^0X$ is explained in text.

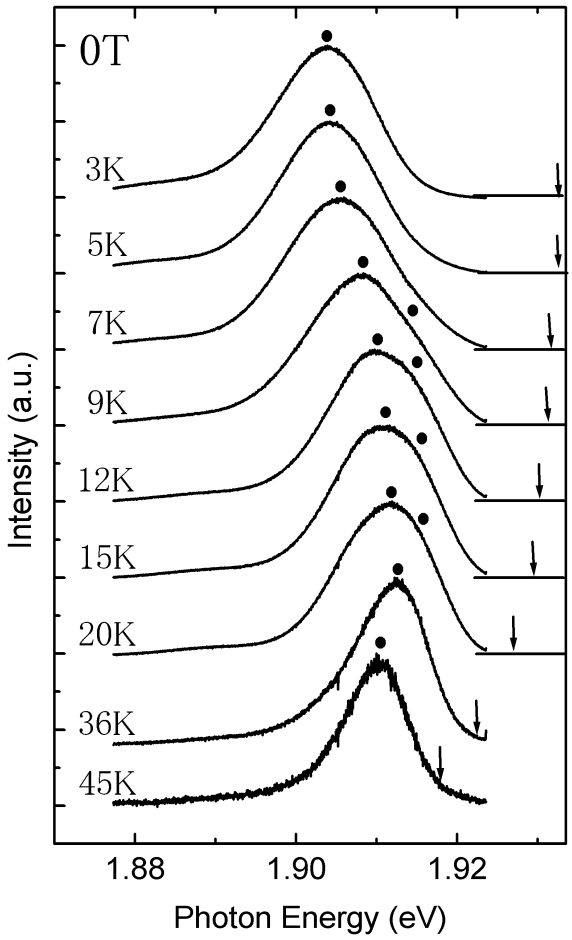


Figure 5.2: Stationary photoluminescence spectra of excitons in $Cd_{0.8}Mn_{0.2}Te$ without magnetic field at various temperatures. The vertical arrow indicates the free exciton energy. The peak intensity is normalized. The peaks shift towards higher energy due to disappearance of MP effect up to temperature 30 K.

vertical arrow indicates the free exciton energy, which is determined from the exciton-reflection spectrum. It can be seen that the peak is composed of two components at the temperature $\leq 30$ K as pointed out with closed circles.

There is also another evidence of two components in photoluminescence. Fig. 5.3 shows the time evolution of photoluminescence spectra without magnetic field at 4 K.

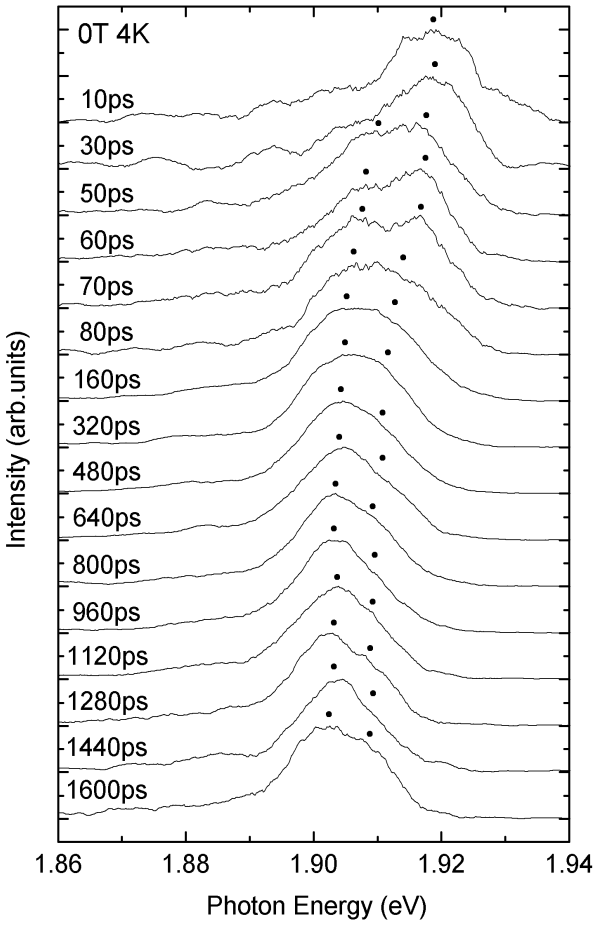


Figure 5.3: Time evolution of the photoluminescence spectrum in $Cd_{0.8}Mn_{0.2}Te$ without magnetic field. The peak intensity is normalized. In the first 40 ps, the shift of the lines is attributed to exciton localization and MP formation.

In the first 40 ps, the shift of the lines is attributed to exciton localization and MP formation. Doublet peaks can be observed at any time. Judging from Fig. 5.3 it is seen that these doublet peaks do not result from rapid energy shift of a single peak within its lifetime. We assume that there is an overlap of photoluminescence due to EMP and due to $A^0$XBMP explained as follows.

At $T = 4$ K the energy positions for each peak are reported as:[53]

$$\begin{aligned} E_{A^0XBMP} &= 1588.8 + 1440x \qquad (0 \leq x \leq 0.1) \\ E_{EMP} &= 1604.7 + 1397x \qquad (0.05 \leq x \leq 0.2) \end{aligned}$$

$$= \quad 1575.0 + 1536x \qquad (0.2 \leq x \leq 0.4). \tag{5.1}$$

$A^0$XBMP is, on trial, assumed to exist up to Mn concentration at $x = 0.2$ as shown in Fig. 5.4.

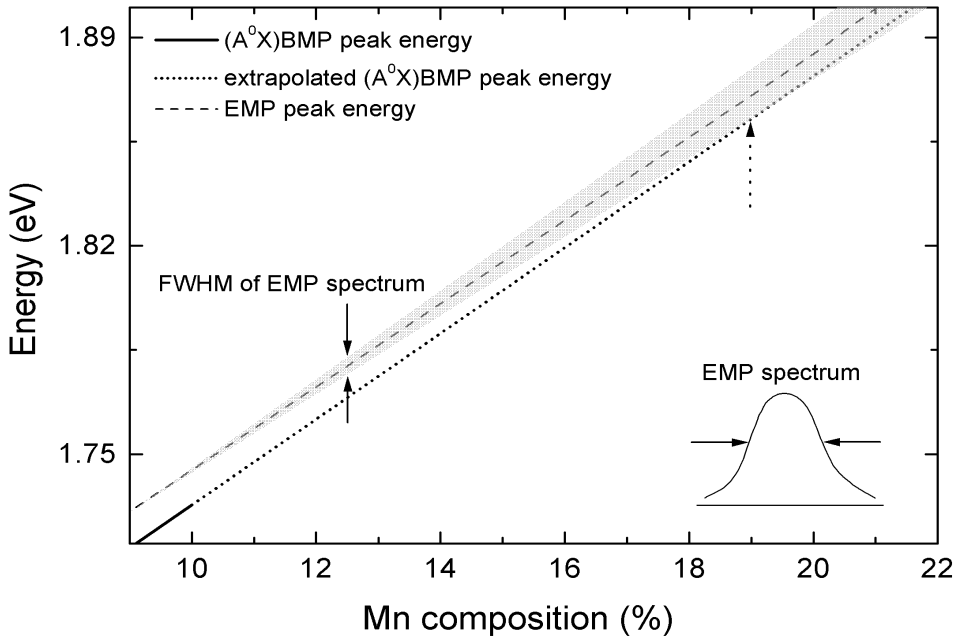


Figure 5.4: Mn composition dependence of peak positions of EMP (broken line) and $A^0$XBMP (solid and dotted lines) obtained from Eq. (5.1). The vertical width of gray region signifies the full width at half maximum of EMP spectrum for various Mn compositions.

It can be found that the energy position of lower side, where the intensity of EMP spectrum is half of maximum, corresponds to the peak position of $A^0$XBMP spectrum at Mn composition $x \cong 19\%$ indicated by dotted arrow in Fig. 5.4. When the width of $A^0$XBMP spectrum is taken into account, we should observe the double peaks in the photoluminescence spectrum at Mn composition slightly lower than 19%. Since this explanation is consistent with the experimental results it is reasonable to assure that there is overlap of EMP recombination and $A^0$XBMP recombination at Mn composition $x = 0.2$. Therefore the high energy peak would be due to EMP and the low energy peak due to $A^0$XBMP. Moreover from Fig. 5.3 the energy difference between $A^0$XBMP and EMP in photoluminescence is deduced about 7 meV.

### 5.1.2 Photoluminescence with magnetic field

Since $Mn^{2+}$ ions spins contribute to the magnetic properties of the sample it is very interesting to measure the photoluminescence with magnetic field. Fig. 5.5 shows the photoluminescence spectra at 5 K for various magnetic fields.

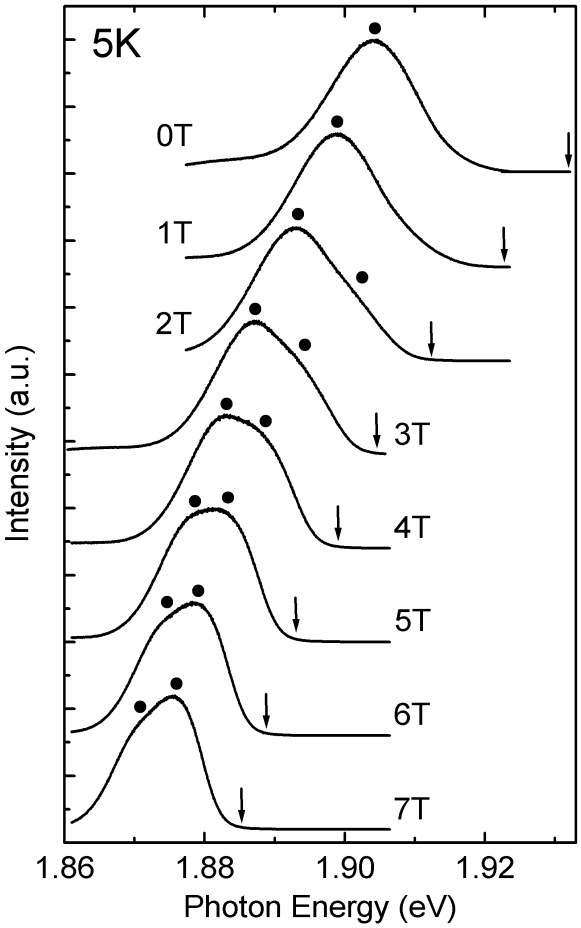


Figure 5.5: Stationary photoluminescence spectra of excitons in $Cd_{0.8}Mn_{0.2}Te$ at 5 K for various magnetic fields. The vertical arrow indicates the free exciton energy. The peak intensity is normalized. The peaks shift towards lower energy due to the large Zeeman splitting of energy levels.

It can be seen that doublet peaks appear more clearly with magnetic field. This tendency was observed at low temperature 3 K - 5 K. In order to clarify the origin of this doublet peaks we measure the circular polarization of photoluminescence with magnetic field. In the Faraday configuration, there are two magnetic subcomponents with the $\sigma^+$ and the $\sigma^-$ polarizations. Not only $\sigma^+$ but also $\sigma^-$ photoluminescence can be observed under band-to-band excitation as shown in Fig. 5.6.

The photoluminescence peak positions in $\sigma^+$ and $\sigma^-$ polarization are not the same with each other as shown in an inset of Fig. 5.6. For the exciton transition only $\sigma^+$ photoluminescence should appear since this transition comes from the lowest energy

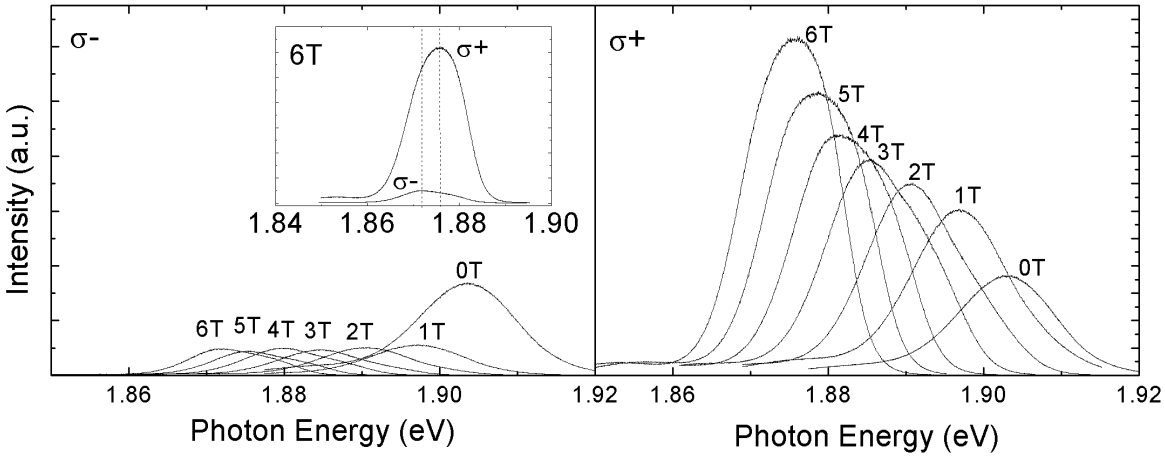


Figure 5.6: Photoluminescence evolution as a function of magnetic field for $\sigma^-$ (left) and for $\sigma^+$ (right). The inset shows the comparison of $\sigma^-$ and $\sigma^+$ lineshape at 6 T.

level of the exciton. In the following we shall demonstrate that $\sigma^+$ photoluminescence is due to exciton and $\sigma^-$ photoluminescence due to $A^0X$. These phenomena are not peculiar to this sample[54].

Here it has to be mentioned that the interpretation of the asymmetric or inhomogeneous photoluminescence as a function of temperature and magnetic field in $Cd_{1-x}Mn_xTe$ has been reported[75][76][77][78]. From a line-shape analysis it has been explained that the linewidth of photoluminescence should arise from the exciton localization by pinning to defect center and by APF. The former yields a symmetric Gaussian line shape, while the latter leads to an asymmetric line shape. Therefore, in conclusion the shape of the photoluminescence spectra is a symmetric Gaussian when the exciton is localized through the hole, i.e. MP effect, on the other hand, APF causing exciton one-particle localization results in the asymmetric Gaussian profile. However, as can be seen in previous figures the photoluminescence spectra are obviously composed of two components. Therefore it can be inferred that, at Mn composition $x \sim 0.2$ non-Gaussian shape photoluminescence is due to two contributions of exciton and $A^0X$.

## 5.2 Theoretical background

In order to make it clear quantitatively that $\sigma^+$ and $\sigma^-$ photoluminescence under band-to-band excitation are due to exciton and $A^0X$, respectively, we shall examine the comparison of experimental and theoretical results in Sec. 5.3. In this section we demonstrate theoretical calculations in detail.

### 5.2.1 Effect of sp-d exchange interaction on exciton

As already stated in Sec. 1.2 the transition energy between the valence band and conduction band is written as:

$$E_{\mathrm{tran}} = E_c - E_v = \begin{cases} E_{\mathrm{exe}} \pm \frac{1}{2} N_0(\alpha - \beta) x \langle S_z \rangle & \text{(electron - heavy hole)} \\ E_{\mathrm{exe}} \pm \frac{1}{2} N_0(\alpha - \frac{1}{3}\beta) x \langle S_z \rangle & \text{(electron - light hole),} \end{cases} \tag{5.2}$$

where $E_{\mathrm{tran}}$ and $E_{\mathrm{exe}}$ are transition energy and exciton energy without magnetic field, respectively. Fig. 5.7 shows the transition energy scheme, namely, $E_{\mathrm{tran}} - E_{\mathrm{exe}}$ dependence on the magnetic field at 4 K.

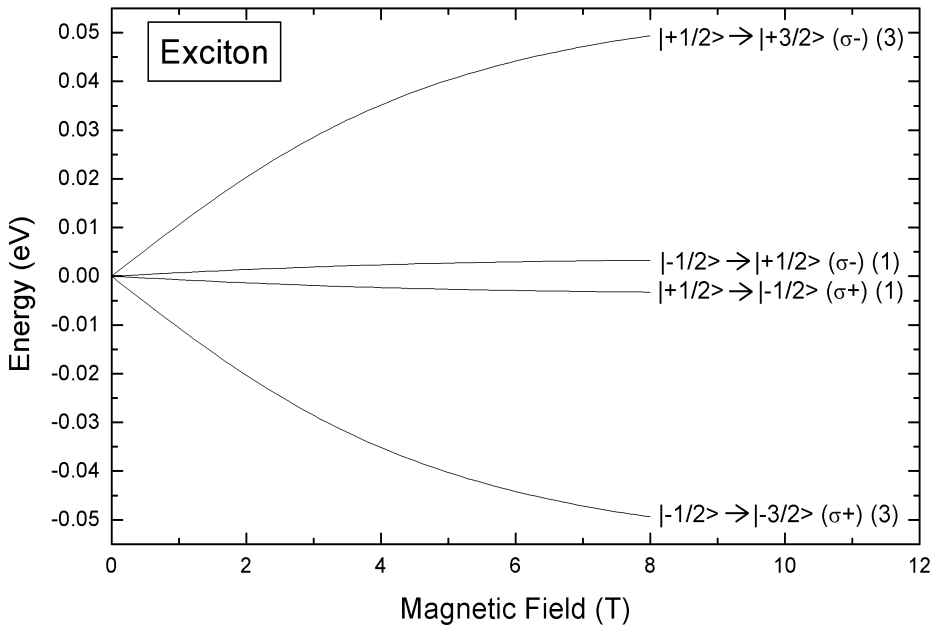


Figure 5.7: Level splitting of the exciton as a function of magnetic field at 4 K. $|m_s\rangle \rightarrow |m_j\rangle$ means transition from a $|m_s\rangle$ electron state in the conduction band to a $|m_j\rangle$ electron state of the valence band. The values in parentheses mean the ratio of oscillator strength.

Due to thermal distribution the photoluminescence should come from the transition $|-1/2\rangle \rightarrow |-3/2\rangle$ ($\sigma^+$). It is important to note that there is no consideration of localization on the APF and MP effect in these calculations.

### 5.2.2 Effect of sp-d exchange interaction on $A^0X$

In the 1980s many systematic studies of acceptor impurities in $Cd_{1-x}Mn_xTe$ have been carried out by photoluminescence experiments[55][56][57][58][59][60][61]. In CdTe, the main acceptor impurities have been determined to be Ag, Cu, Li, and Na[62][63]. The former two impurities are deep acceptors and the latter two are shallow acceptors. The $A^0X$ photoluminescence spectrum is attributed to exchange interactions between the bound particles, namely, two $\Gamma_8$ holes with angular momentum $j = \frac{3}{2}$, and one $\Gamma_6$ electron with angular momentum $j = \frac{1}{2}$. In terms of the *j*-*j* coupling scheme in cubic symmetry, the two $\Gamma_8$ holes are combined antisymmetrically to form $J_{jj} = 0$ ($\Gamma_1$) and 2 ($\Gamma_3 + \Gamma_5$) states[64]. Then the $A^0X$ states would be described by a total angular momentum $J = 1/2$ ($\Gamma_6$), $3/2$ ($\Gamma_8$), $5/2$ ($\Gamma_7 + \Gamma_8$) with additional coupling to the $\Gamma_6$ electron since $\Gamma_1 \times \Gamma_6 = \Gamma_6$, $\Gamma_3 \times \Gamma_6 = \Gamma_8$, $\Gamma_5 \times \Gamma_6 = \Gamma_7 + \Gamma_8$ in the $T_d$ point group. Experimentally, bound exciton states derived from the $J_{jj} = 0$ two-hole state appear to be the lowest energy for deep acceptors[65][66][67][68], while the converse situation is true for shallow acceptors[69][70][71]. Therefore the lowest $A^0X$ level for deep acceptor is $J = 1/2$ and for shallow acceptor is $J = 3/2$ and $J = 5/2$. The final acceptor state of the transition $A^0$ is the neutral acceptor state $J = 3/2$.

For hole in the $A^0$ level and for holes in the $A^0X$ level the quantity $N_0\beta$ is taken as positive (inverse of $N_0\beta$ for electron in valence band). This is in agreement with the polarization of the lowest energy Zeeman component $\sigma^-$.

#### Deep acceptor

The lowest energy level for $A^0X$ is $J = 1/2$ in case of deep acceptor. The final state of the transition is the neutral acceptor state $J = 3/2$. Hence, higher energy level of $A^0X$ is $|m_J\rangle = |+1/2\rangle$ ($m_{J_{jj}} = 0$, $m_e = 1/2$) and lower is $|-1/2\rangle$ ($m_{J_{jj}} = 0$, $m_e = -1/2$) for deep acceptor with magnetic field ($B//z$), where $m_J$, $m_{J_{jj}}$, and $m_e$ are $z$ component of total angular momentum, two-holes angular momentum, and electron angular momentum, respectively. The energy levels of $A^0$ and $A^0X$ are sketched in Fig. 5.8.

The transition energy of the deep $A^0X$ is shown in Fig. 5.9. For a bound hole in deep

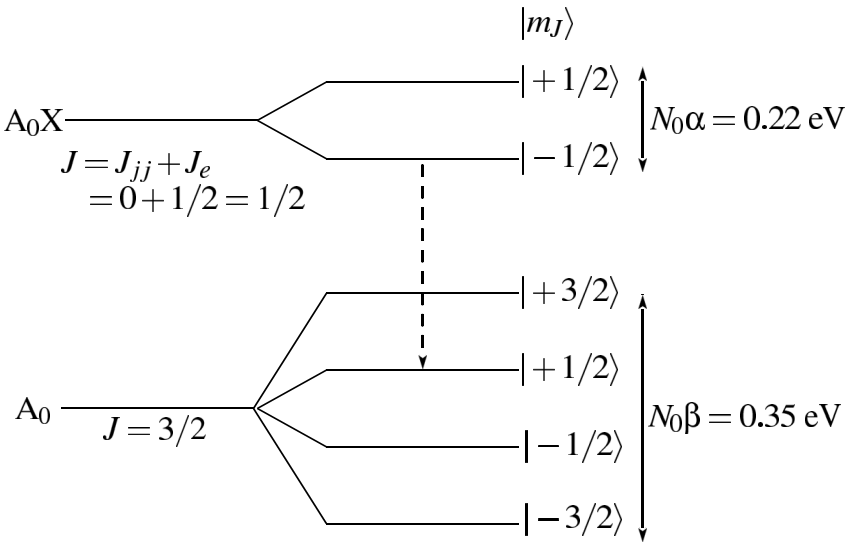


Figure 5.8: A schematic picture of the spin splitting of deep $A^0$ (ground state) and deep $A^0X$ (excited state) in a magnetic field. This considers only $J = 1/2$ as $A^0X$ state. A dotted arrow represents the lowest energy transition explained in text.

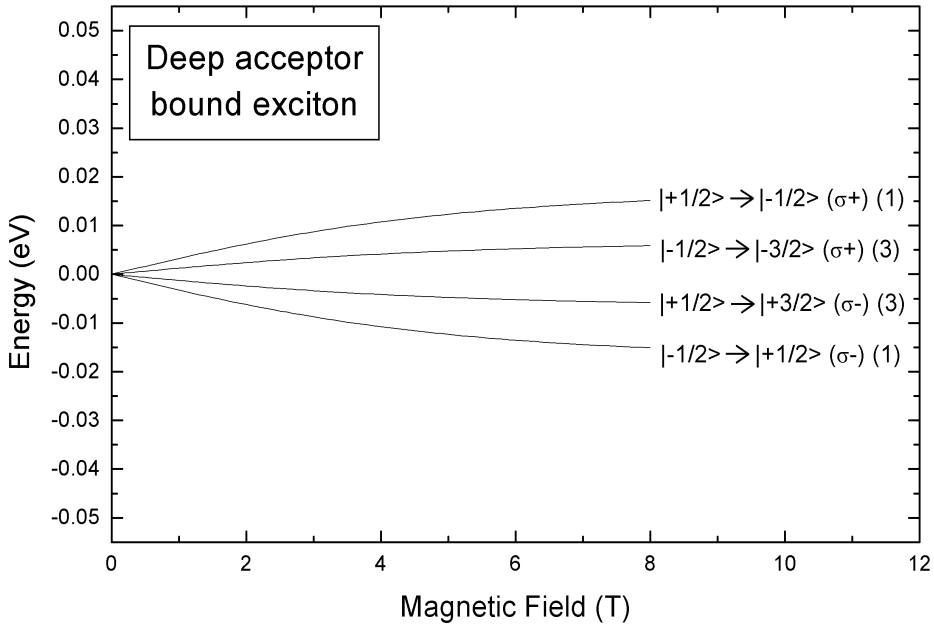


Figure 5.9: Transition energy of deep $A^0X \rightarrow$ deep $A^0$ as a function of magnetic field at 4 K. The quantity $N_0\beta$ is 0.35 eV. The values in parentheses mean the ratio of oscillator strength. This considers only $J = 1/2$ as $A^0X$ state.

$A^0$ the value $N_0\beta$ is not reported, therefore on trial, we take the quantity $N_0\beta = 0.35$ eV as explained later. The procedure of calculation for deep acceptor is same as for exciton. The lowest transition energy is, as a result, $|-1/2\rangle \rightarrow |+1/2\rangle$ ($\sigma^-$). It is noted that this considers only $J = 1/2$ level as $A^0X$ state. Actually it should be taken into account both $J_{jj} = 0$ and 2 levels as described at the end part of this section.

**Shallow acceptor**

For a bound hole in shallow $A^0$ we take a known quantity $N_0\beta = 0.65$ eV[72][73]. For a shallow acceptor, the lowest energy level of the $A^0X$ is $J = 3/2$ and $J = 5/2$. Hence, the highest energy level of the $A^0X$ is $|m_{J_{jj}}, m_e\rangle = |+2, +1/2\rangle$ and the lowest is $|-2, -1/2\rangle$. The final state of the transition is $A^0$ state $J = 3/2$. The energy levels of shallow $A^0$ and $A^0X$ are sketched in Fig. 5.10.

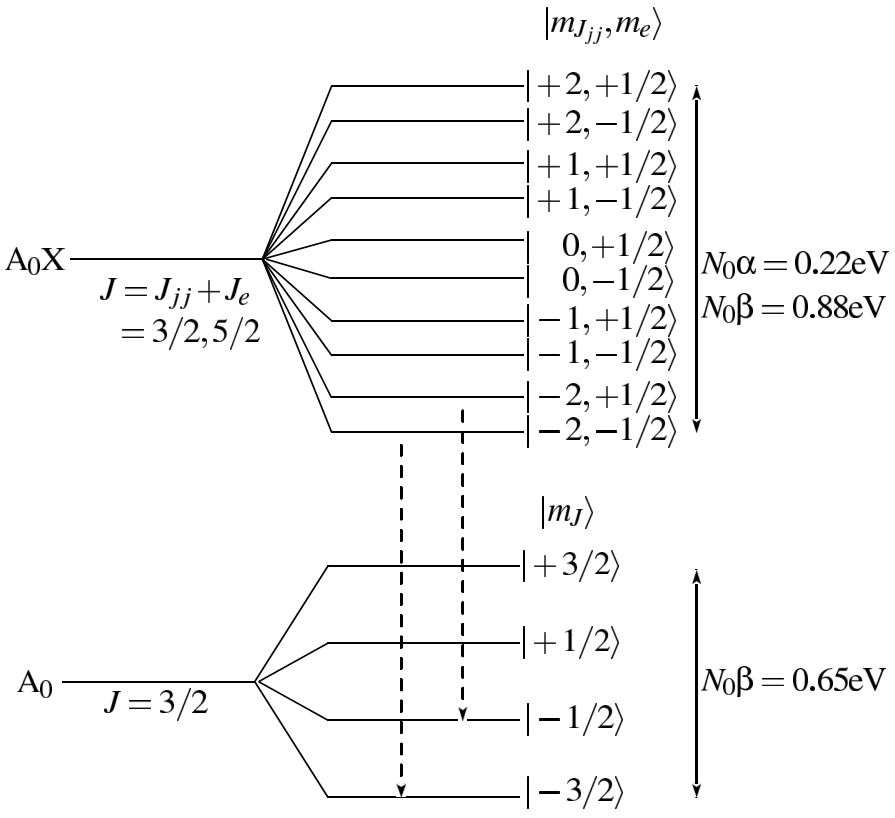


Figure 5.10: A schematic picture of the spin splitting of the shallow $A^0$ (ground state) and shallow $A^0X$ (excited state) in a magnetic field. This considers only $J = 3/2$ and $5/2$ as $A^0X$ states. Dotted arrows represent the lowest energy transition explained in text.

The procedure by which the transition energy for shallow acceptor is calculated is same as for exciton, moreover, the following matrix elements are also used in calculation for selection rule[63]:

$$\left\langle \pm\frac{3}{2}|P_{\pm}|\pm 2,\pm\frac{1}{2}\right\rangle = -\frac{1}{\sqrt{6}},\ \left\langle \pm\frac{1}{2}|P_{\pm}|\pm 2,\mp\frac{1}{2}\right\rangle = -\frac{1}{\sqrt{2}},\ \left\langle \mp\frac{1}{2}|P_{\pm}|\pm 1,\mp\frac{1}{2}\right\rangle = -\frac{1}{\sqrt{2}},$$

$$\left\langle \mp\frac{1}{2}|P_{\pm}|\ 0,\ \pm\frac{1}{2}\right\rangle = +\frac{1}{\sqrt{12}},\ \left\langle \mp\frac{3}{2}|P_{\pm}|\mp 1,\pm\frac{1}{2}\right\rangle = +\frac{1}{\sqrt{6}},\ \left\langle \mp\frac{3}{2}|P_{\pm}|\ \ 0,\ \mp\frac{1}{2}\right\rangle = -\frac{1}{2}, \tag{5.3}$$

where $P_{\pm}$ is the momentum operator for the $\sigma_{\pm}$ transition between $|m_{J_{jj}}, m_e\rangle$ $A^0X$ state and $\langle m_J|$ $A^0$ state. The transition energy of the shallow $A^0X$ is shown in Fig. 5.11.

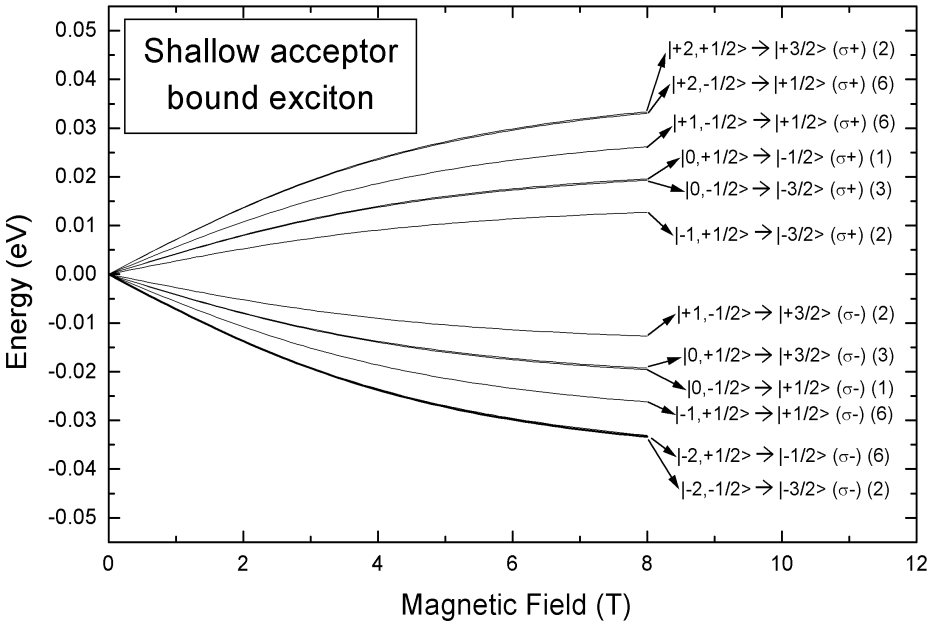


Figure 5.11: Transition energy of shallow $A^0X \rightarrow$ shallow $A^0$ as a function of magnetic field at 4 K. The values in parentheses mean the ratio of oscillator strength. This considers only $J = 3/2$ and $5/2$ as $A^0X$ states.

The procedure of calculation for shallow acceptor is the same as for deep acceptor and exciton. The lowest transition energy is, as a result, $|-2,+1/2\rangle \rightarrow |-1/2\rangle$ ($\sigma^-$) and $|-2,-1/2\rangle \rightarrow |-3/2\rangle$ ($\sigma^-$).

In the above consideration only $A^0X$ levels derived from the lowest $J_{jj}$ level are taken into account, e.g. $J = 1/2$ for deep $A^0X$ and $J = 3/2, J = 5/2$ for shallow $A^0X$. However, one should consider both levels derived from $J_{jj} = 0$ and 2. This is because the energy difference between $J_{jj} = 0$ and 2 is in the sub-meV. Since the Zeeman splitting is rather large as shown in Fig. 5.12 in high magnetic field, it does not matter whether the acceptor is deep or shallow for $A^0X$ state. At high magnetic field, for both deep and shallow $A^0X$, the lowest level is $|-2,-1/2\rangle$ of $A^0X$ state. It is important to note that any consideration of localization on the APF and MP effect are not yet carried out in these calculations.

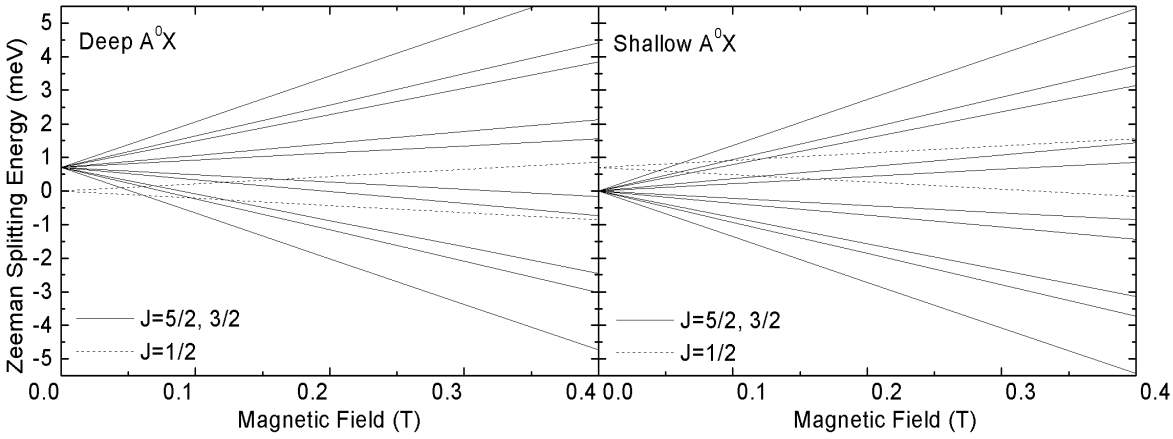


Figure 5.12: The comparison of Zeeman splitting for deep $A^0X$ and shallow $A^0X$ levels.

## 5.3 Comparison of experimental results and theoretical results

With Fig. 5.7 and 5.12 at high magnetic field $\sigma^+$ and $\sigma^-$ photoluminescence lines are interpreted as follows:

- $\sigma^+$ component: the lowest energy transition of exciton $\cdots |-1/2\rangle \rightarrow |-3/2\rangle$
- $\sigma^-$ component: the lowest energy transition of $A^0X$ $\cdots |-2,-1/2\rangle \rightarrow |-3/2\rangle$.

Note that due to thermalization in the $A^0X$ states only $|-2,-1/2\rangle \rightarrow |-3/2\rangle$ transition could be considered.

Fig. 5.13 shows the comparison of experimental results and calculation results. At low magnetic field, the MP effect should be considered. The localization energy due to MP is known to be 15 meV for exciton as obtained from photoluminescence excitation studies in Fig. 5.14. Therefore we assume that the exciton energy without MP effect is 15 meV higher than the photoluminescence line. The theoretical result is in good agreement for exciton ($\sigma^+$), if we assume that the MP exists till a magnetic field up to 4 T. From the energy difference between the reflectivity peak and the exciton energy position without MP, we deduce a localization energy of APF equal to 11 meV. There is no report on the binding energy of $A^0X$ without MP localization, namely, the energy difference between free exciton and $A^0X$ in $Cd_{1-x}Mn_xTe$. From comparison with data in CdTe we suppose that the $A^0X$ peak without MP is 7 meV below the calculated result of exciton[56]. This value is same as one obtained experimentally in Sec. 5.1.1.

From the comparison between the calculated energy position of the $A^0X$ line and the experimental position of the $\sigma^-$ component as a function of magnetic field, we take the value $N_0\beta = 0.35$ for a bound hole in deep $A^0$ state explained as follows. As mentioned in Sec. 5.2.2 the lowest energy transition between $A^0X$ and $A^0$ is $|-2,-1/2\rangle \rightarrow |-3/2\rangle$. For holes in $A^0X$ the quantity $N_0\beta$ should be the same as for a free hole (0.88 eV) because the Bohr radius of holes in $A^0X$ is expanded in space very much. As mentioned before, for a bound hole in shallow $A^0$ the quantity $N_0\beta$ is known to be 0.65 eV. Suppose calculation is carried out with $N_0\beta = 0.65$ eV, the theoretical result is beyond reason. On the other hand, for a bound hole in deep $A^0$ the value $N_0\beta$ is not reported because binding energy for a hole bound to deep acceptor is too complicated to calculate. However, we can qualitatively estimate that the quantity $N_0\beta$ of a bound hole in deep $A^0$ should be

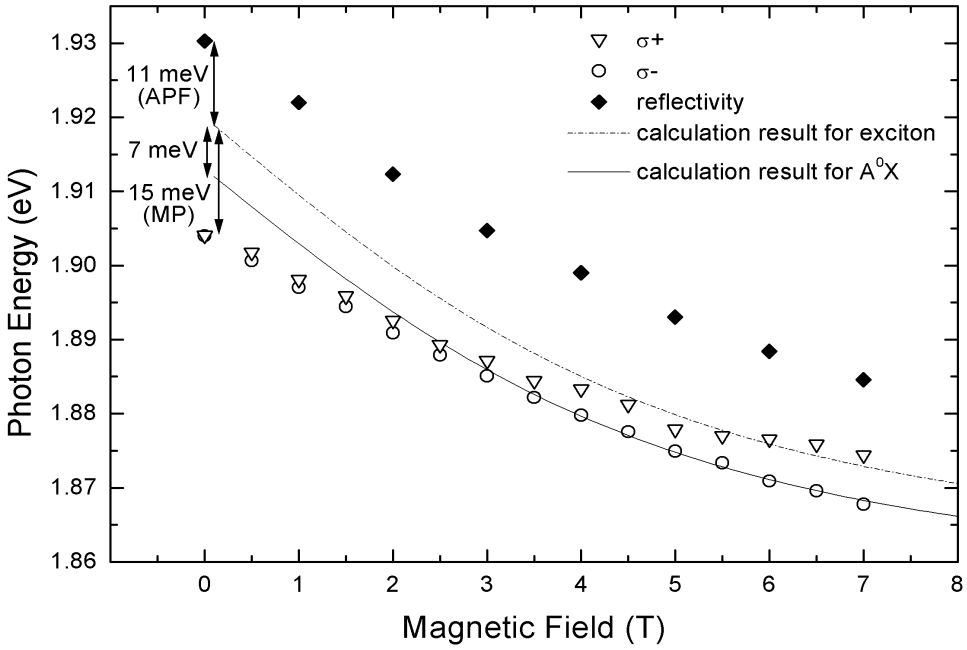


Figure 5.13: The comparison of the photoluminescence peak position with the calculated position as a function of magnetic field at 4 K. Since MP and APF effect are not considered in the calculation, the calculated position is not in good agreement with photoluminescence line at low magnetic field. The values of localization energy due to APF and MP are 11 meV and 15 meV, respectively. The binding energy of $A^0X$ without MP localization is considered to be 7 meV.

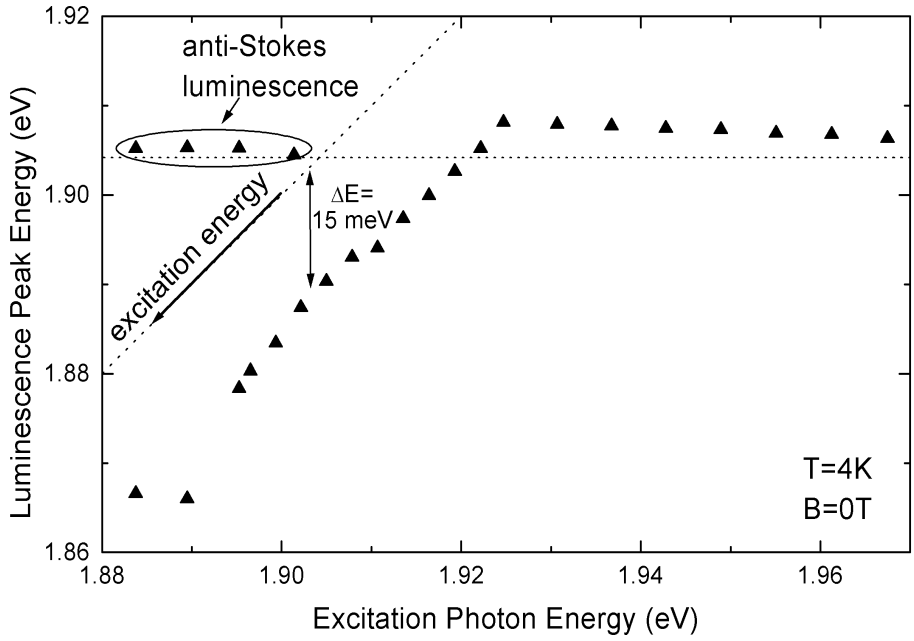


Figure 5.14: The peak position of the photoluminescence as a function of excitation photon energy. Anti-Stokes photoluminescence is explained later (Sec. 5.4).

smaller than 0.65 eV. The reason is that the binding energy of a hole bound to deep acceptor should be much larger than that of a hole bound to shallow acceptor. Since the larger the binding energy is the smaller the Bohr radius is, The number of Mn ion spins with which a hole bound to deep acceptor can interact is less than that to shallow acceptor. In case of quantitative discussion we should consider also spin-orbit interaction. By fitting procedure, if we assume that the MP exists till a magnetic field up to 3 T, it is found that there is good agreement when $N_0\beta = 0.35$ eV for a bound hole in deep $A^0$ as shown in Fig. 5.13. It is reported that the quantity $N_0\beta$ of confined holes in $Cd_{1-x}Mn_xTe$ quantum well or quantum dot can be half value of bulk crystal[74]. Hence the 0.35 eV is not irrelevant.

In addition to above Zeeman effect, the diamagnetic effects should be observed, however, it is explained to be negligible as follows. For the $A^0X$ complex, there would be two types of diamagnetic effects being proportional to $B^2$ where $B$ is the magnitude of the applied magnetic field. One is a diamagnetic splitting effect in the $A^0$ state $J = 3/2$ which splits the gravity center of the $m_J = \pm 1/2$ components apart from the $m_J = \pm 3/2$ components, and another is a diamagnetic shift effect in both $A^0X$ and $A^0$ states. These effects are negligibly small in $Cd_{1-x}Mn_xTe$ because the Zeeman shift and inhomogeneous broadening of photoluminescence width due to fluctuation is quite large.

## 5.4 Anti-Stokes photoluminescence

In this section we show the unique phenomena under selective excitation or under excitation at energies lower than the dominant photoluminescence peak energy.

In order to examine the photoluminescence of semimagnetic semiconductors in detail, the method of selective (resonance) excitation is useful because we can measure the energies of MP effect directly[47]. As shown in Fig. 5.13 with decreasing excitation energy the constant Stokes shift can be found. This is the localization energy due to MP effect. Concerning the intensity of photoluminescence, with decreasing excitation energy, it abruptly decreases under excitation at 1.91 eV. Furthermore, an anti-Stokes photoluminescence line which is located on the higher energy side of the excitation energy, appears under excitation at energies lower than the dominant photoluminescence peak energy obtained for band-to-band excitation as shown in Fig. 5.15.

The three narrow peaks on a lower energy line of the lowest spectrum are known to be MnTe $LO_1$ (24.49 meV), CdTe $LO_2$ (20.25 meV), and CdTe $TO_2$ (17.68 meV) Raman Stokes lines[2]. The anti-Stokes photoluminescence can be also observed under non-selective excitation energies well below the photoluminescence peak energy as shown in the bottom spectrum of Fig. 5.16. The photoluminescence in top figure is ascribed to the recombination of localized EMP.

Fig. 5.17 shows the excitation energy dependence of the anti-Stokes photoluminescence. The anti-Stokes photoluminescence in this material[80] as well as in various semiconductors[81][82][83] has been reported. In case of non-resonant excitation the intensity does not change very much with excitation photon energy. Regarding peak position and width the value is almost constant, namely, the profile in the photoluminescence spectrum does not change very much as a function of excitation energy. At excitation energy higher than 1.85 eV (resonant excitation) the photoluminescence intensity abruptly increases with increasing excitation energy. This is not due to laser-scattered light, because the intensity decreases before the cut point as shown in Fig. 5.18. First we consider the non-resonant case.

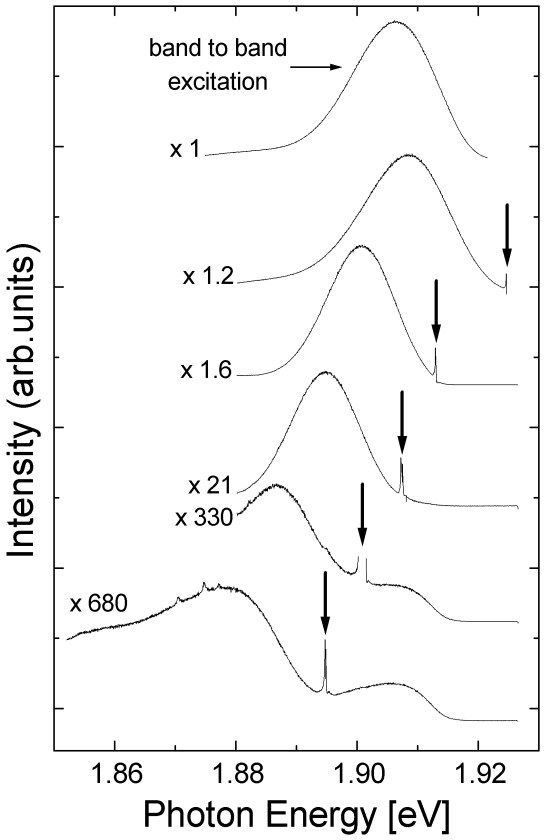


Figure 5.15: Stationary photoluminescence spectra of excitons in $Cd_{0.8}Mn_{0.2}Te$ without magnetic field at 4 K under selective excitation at different energies. The peak intensity is normalized.

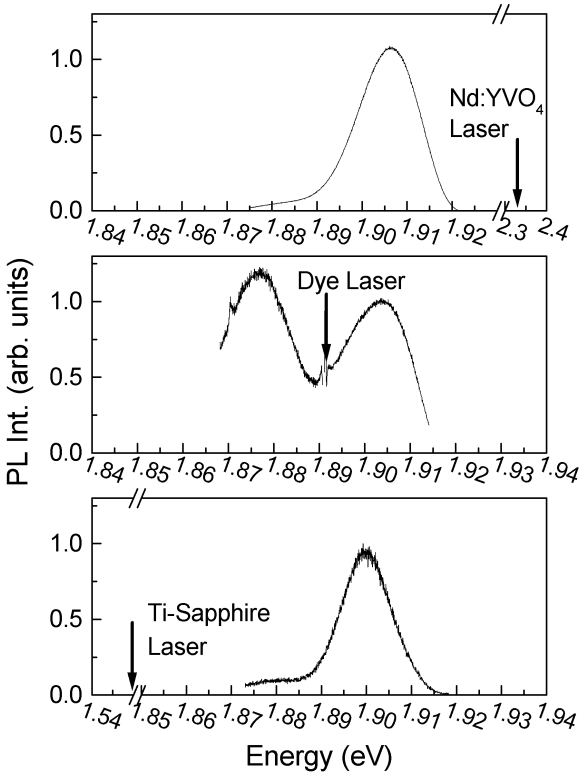


Figure 5.16: Stationary photoluminescence spectra of $Cd_{0.8}Mn_{0.2}Te$ at 4 K under band-to-band excitation (top), selective excitation (middle) and excitation at energies much lower than the dominant photoluminescence peak energy (bottom). The peak intensity is normalized.

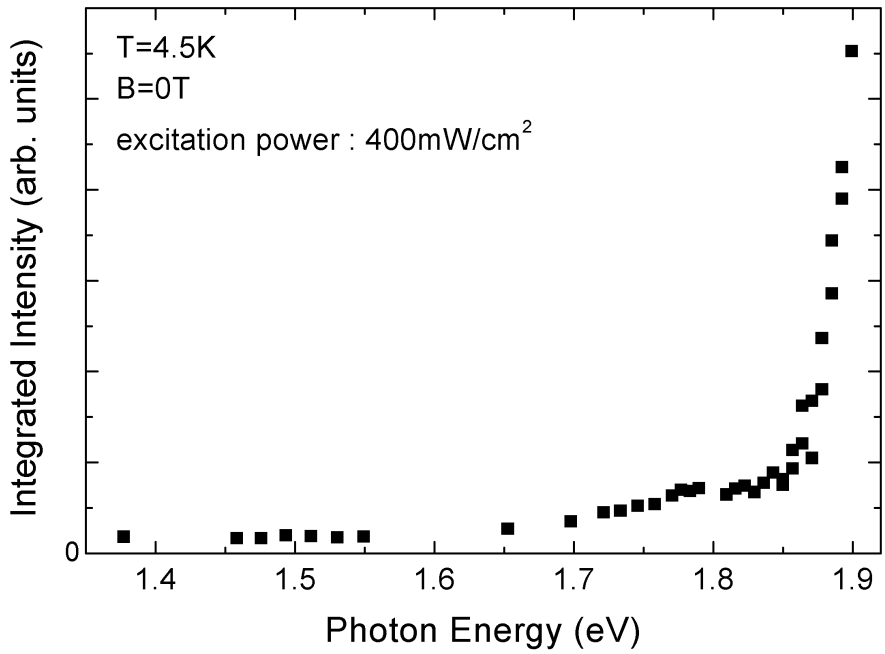


Figure 5.17: Excitation photon energy dependence of integrated intensity of anti-Stokes photoluminescence without magnetic field.

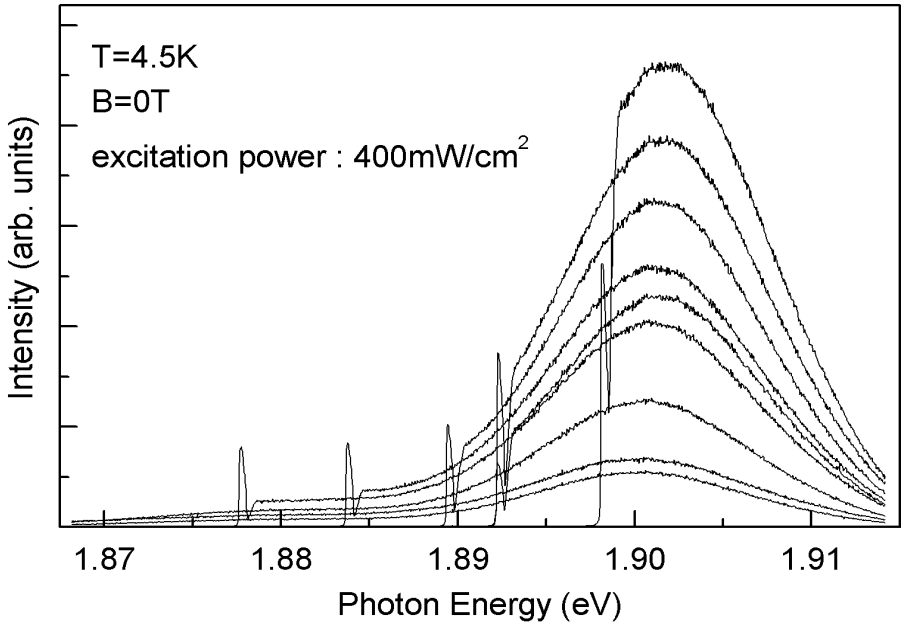


Figure 5.18: Anti-Stokes photoluminescence evolution with various excitation energies.

### 5.4.1 Non-resonant excitation

The spectrally integrated anti-Stokes photoluminescence intensity versus excitation power $Cd_{0.8}Mn_{0.2}Te$ with $x = 0.2$ is shown in Fig. 5.19.

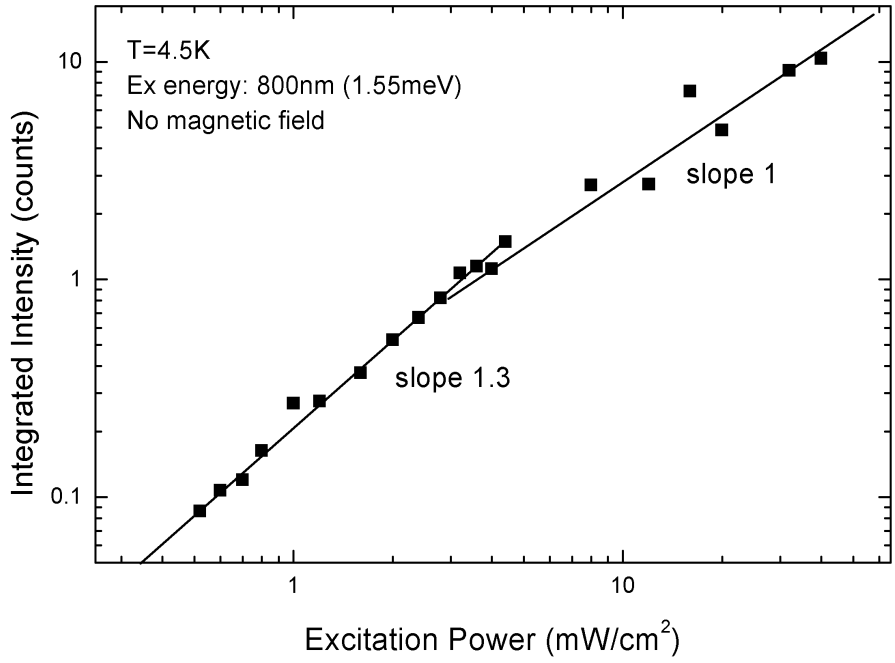


Figure 5.19: The excitation power dependence of integrated anti-Stokes photoluminescence lines at 4.5 K and zero magnetic field for $Cd_{0.8}Mn_{0.2}Te$ with $x = 0.2$. Excitation energy is 800 nm (1.55 eV).

We also analyzed the intensity of the peak as a function of excitation power, in the high energy side of photoluminescence line where reabsorption process is not negligible as well as in the low energy side. All the data show the same tendency as Fig. 5.19. The excitation power dependence in Fig. 5.19 reveals two straight lines having slopes of 1.3 and 1 for intensity below and above 4 mW/cm$^2$, respectively. From general arguments the microscopic mechanisms leading to anti-Stokes photoluminescence are Auger recombination, thermal activation by the absorption of phonons, and contribution of two or more photons in the optical excitation process[79]. There are two explicit mechanisms for the latter two-photon excitation process. First, the intermediate state is not real, i.e. the lifetime of an excitation in this virtual state is limited by the inverse energetic distance to the

next real state (two-photon absorption process). Secondly, two-step absorption process, where the intermediate state is real and a relaxation of the excitation to lower-lying real states may occur before absorption of the second photon. Since all experiments have been performed at 4K (0.34 meV), thermal activation can be excluded. Furthermore, both two-photon absorption and Auger recombination can be ruled out, since they would exhibit a quadratic or cubic dependence on excitation density for the entire power regime, respectively. Therefore we assume that the mechanism of anti-Stokes photoluminescence is a two-step absorption process. The intermediate states would be very localized states in the tail of the density of states due to APF. Then density of state is small and they are easily saturated by light. This explains that the slope changes from 1.3 to 1 in Fig. 5.19.

Since the anti-Stokes photoluminescence line shape is modified by reabsorption deep in the sample it is very important to consider the absorption of excitation light and re-absorption of anti-Stokes photoluminescence. For low energy excitation the excitation light penetrates deep in the sample and anti-Stokes photoluminescence is very much re-absorbed. Intensity of anti-Stokes photoluminescence $I_{AS}$ is expressed with reabsorption coefficient as:

$$I_{AS} \propto I_{B.to.B} \int_0^\infty (\alpha_{\rm exc}(\lambda_{\rm exc}) + \beta I) \exp\{-(\alpha_{\rm exc}(\lambda_{\rm exc}) + \beta I + \alpha(\lambda_{\rm exc})x\} \exp(-\alpha(\lambda)x)\, dx, \tag{5.4}$$

where $\alpha_{\rm exc}(\lambda_{\rm exc}) + \beta I$ is absorption coefficient of excitation light in the presence of excitons, $\alpha(\lambda_{\rm exc})$ and $\alpha(\lambda)$ are the one photon absorption coefficients at excitation and luminescence wavelength, respectively. $\beta I$ is the non-linear effect of excitation absorption, $I_{B.to.B}$ is photoluminescence intensity under band-to-band excitation. Then

$$\frac{I_{B.to.B}}{I_{AS}} \propto \frac{\alpha_{\rm exc}(\lambda_{\rm exc}) + \beta I + \alpha(\lambda_{\rm exc}) + \alpha(\lambda)}{\alpha_{\rm exc}(\lambda_{\rm exc}) + \beta I}. \tag{5.5}$$

In this experiment the excitation power is not large, then $\beta I$ can be neglected. The value $\alpha_{\rm exc}(\lambda_{\rm exc})$ and $\alpha(\lambda_{\rm exc})$ are much smaller than $\alpha(\lambda)$ in case of low excitation energy (non-resonant excitation). Then

$$\frac{I_{B.to.B}}{I_{AS}} \propto \frac{\alpha(\lambda)}{\alpha_{\rm exc}(\lambda_{\rm exc})}. \tag{5.6}$$

The ratio $I_{B.to.B}/I_{AS}$ in logarithm plot is given in Fig. 5.20 for three different excitation wavelengths at $B = 0$. As expected the curves are more or less parallel. They represent the absorption coefficient of the material in the region of the anti-Stokes luminescence, i.e. in the region of localized exciton states. The relationship Eq. (5.6) is not completely

valid at low photon energy (excitation energy is 1.777 eV) in Fig. 5.20 because there is some saturation of the excited localized states (intermediated state in two-step process) in band-to-band excitation.

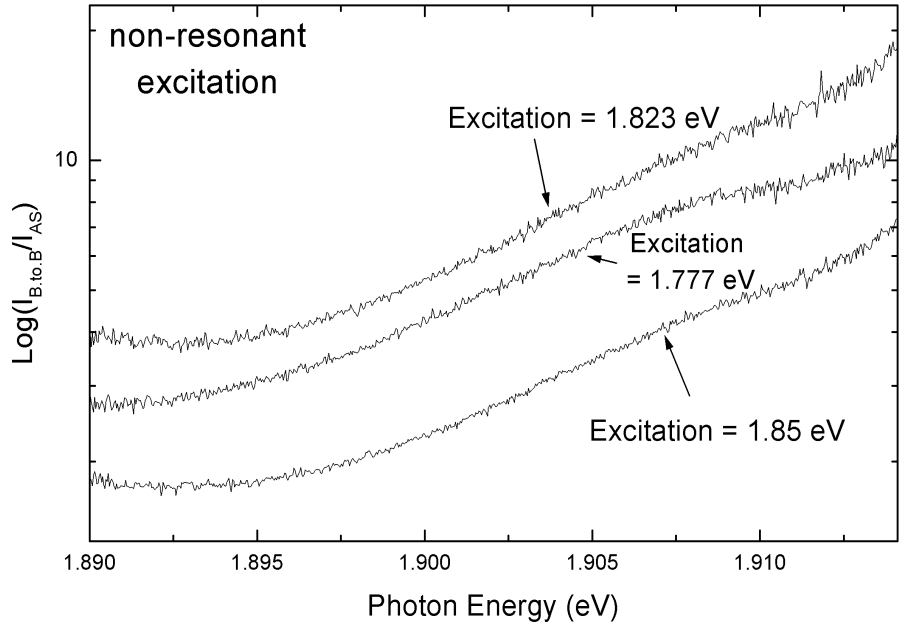


Figure 5.20: The logarithm plot of ration $I_{B.to.B}/I_{AS}$ as a function of photon energy in case of low energy non-resonant excitation for anti-Stokes photoluminescence.

It is interesting to study anti-Stokes photoluminescence with magnetic field since *sp-d* exchange interaction remarkably contributes to the physical process. Now we shall see how reabsorption effect can explain the behavior of anti-Stokes photoluminescence in a magnetic field and that this behavior is consistent with the existence of localized excitons and acceptor bound excitons. Fig. 5.21 demonstrates a typical magnetic field evolution of the anti-Stokes photoluminescence lines in $Cd_{0.8}Mn_{0.2}Te$. The anti-Stokes photoluminescence exhibits peculiar behavior with external magnetic field compared with photoluminescence under band-to-band excitation in Fig. 5.6. It can be seen that $\sigma^+$ anti-Stokes photoluminescence intensity decreases with the magnetic field, contrary to the behavior of the $\sigma^+$ line in case of band-to-band excitation, as shown in Fig. 5.22.

In order to understand the reabsorption effects of anti-Stokes photoluminescence with magnetic field the ratio $I_{B.to.B}/I_{AS}$, which is proportional to $\alpha(\lambda)$, is given in Fig. 5.23 with different magnetic fields. As expected there is a shift of the absorption coefficient edge with magnetic field. When magnetic field increases, the energy difference between

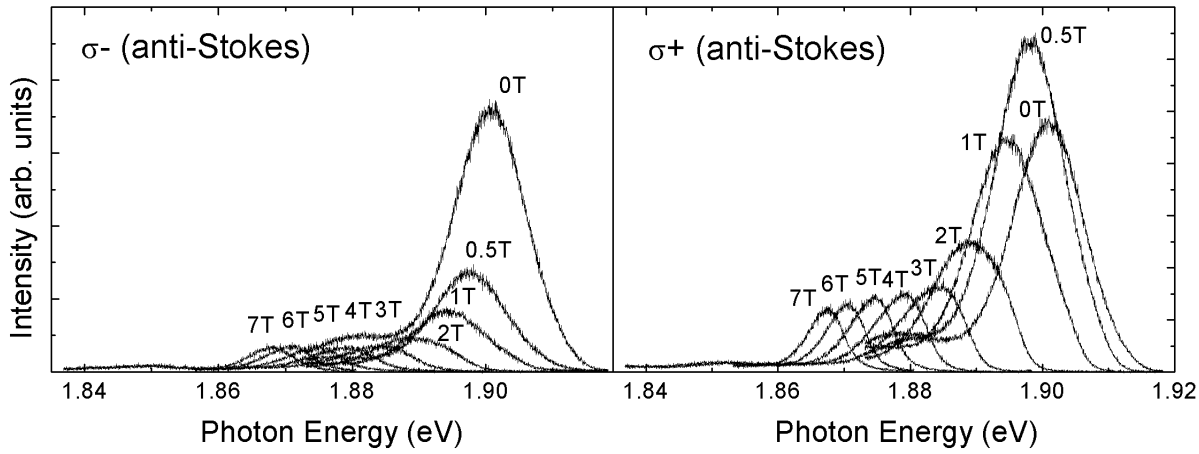


Figure 5.21: The anti-Stokes photoluminescence evolution as a function of magnetic field for $\sigma^-$ (left) and for $\sigma^+$ (right) photoluminescence. Excitation energy is 800 nm (1.55 eV).

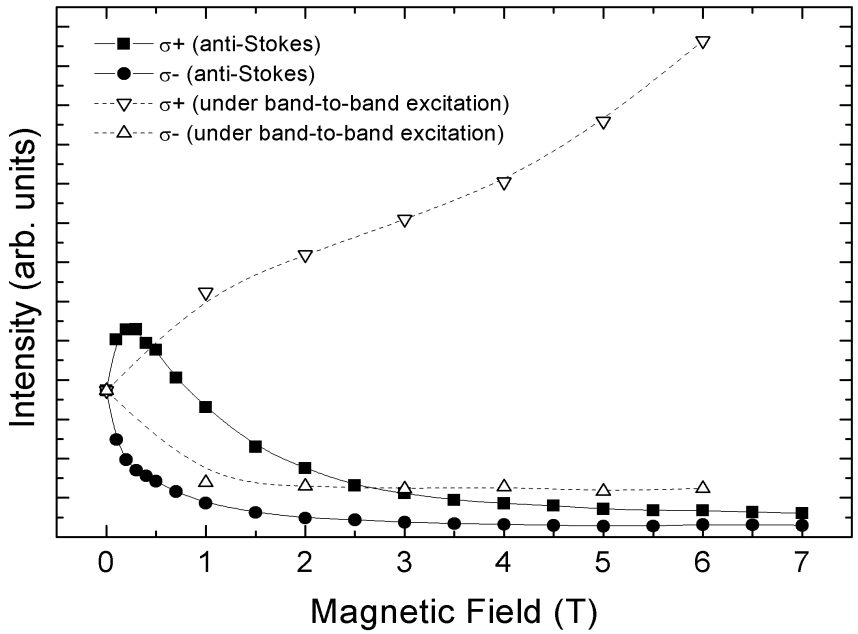


Figure 5.22: Magnetic field dependence of anti-Stokes photoluminescence intensity and photoluminescence intensity under band-to-band excitation.

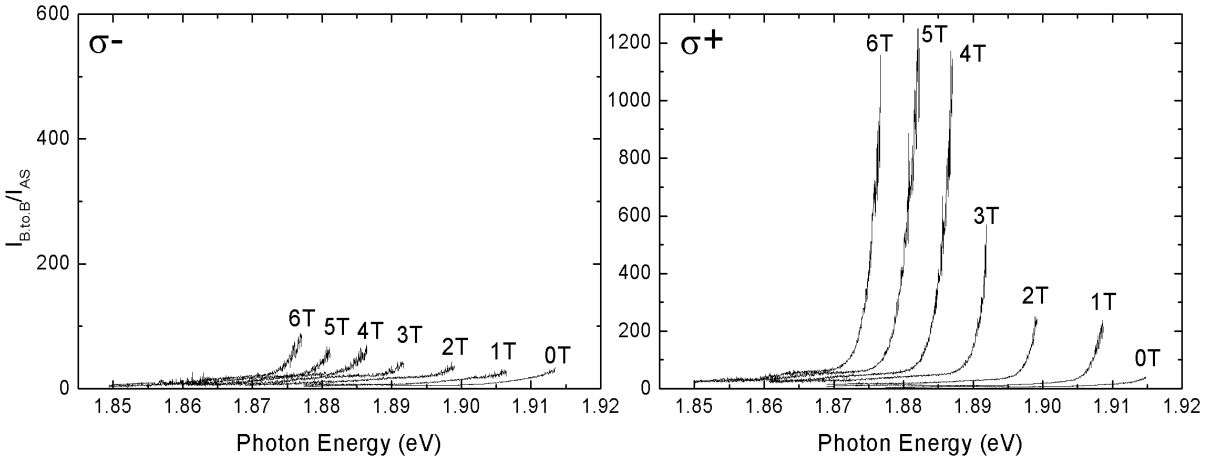


Figure 5.23: $I_{B.to.B}/I_{AS}$ with various magnetic fields for $\sigma^-$ (left) and for $\sigma^+$ (right) photoluminescence. This quantity is proportional to the absorption coefficient at photoluminescence energy in the anti-Stokes line (see text).

exciton absorption line and photoluminescence line decreases because the MP effect vanishes. Therefore the high energy level of the localized exciton line is more reabsorbed. This increasing reabsorption effect with the magnetic field explains well the decrease of $\sigma^+$ anti-Stokes photoluminescence intensity. From this analysis of anti-Stokes photoluminescence we can conclude that $\sigma^+$ is the tail of localized exciton emission. The high energy side of the $\sigma^+$ anti-Stokes photoluminescence line is much reabsorbed. As shown in Fig. 5.23 it can be seen that the absorption is much weaker for the $\sigma^-$ than for $\sigma^+$ polarization besides the usual shift of absorption edge with magnetic field. Since the $\sigma^-$ component of anti-Stokes photoluminescence is only weakly reabsorbed, it comes from the $A^0$XBMP located at the lower energy than that of the EMP.

Then we can consider the anti-Stokes photoluminescence intensity, width and peak position for $\sigma^+$ and $\sigma^-$ polarization. Fig. 5.24 shows the normalized degree of circular polarization as a function of magnetic field. At low magnetic field, the reabsorption for each polarization is weak as shown in Fig. 5.23. They correspond to transitions from EMP and $A^0$XBMP, respectively. At high magnetic field, only the tail of the $\sigma^+$ transition can be observed superimposed on the $\sigma^-$ transition as shown in Fig. 5.25. For $B <$ 2 T, where the anti-Stokes photoluminescence shows peculiar behavior compared with photoluminescence under band-to-band excitation, the lines are not much reabsorbed;

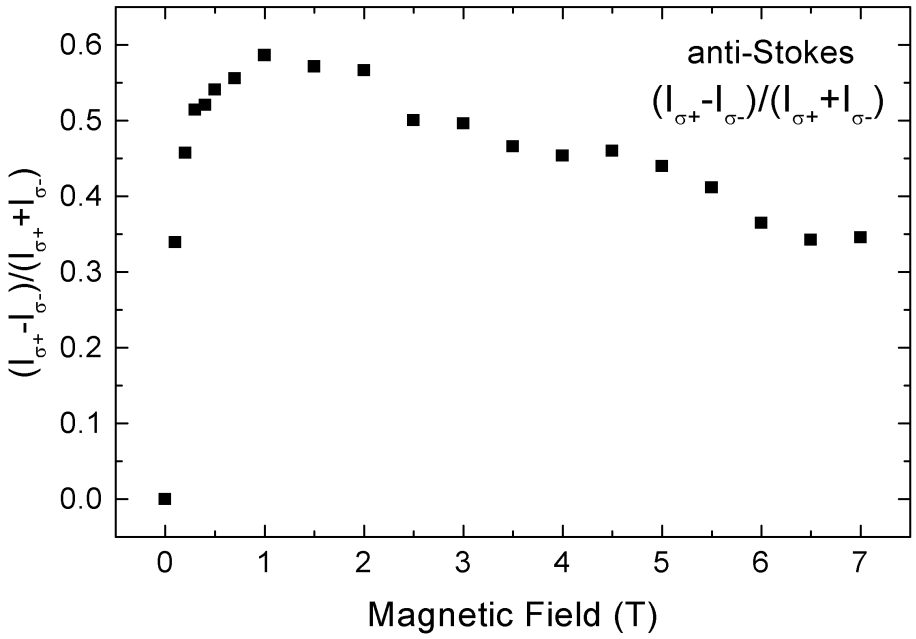


Figure 5.24: Normalized degree of circular polarization as a function of magnetic field.

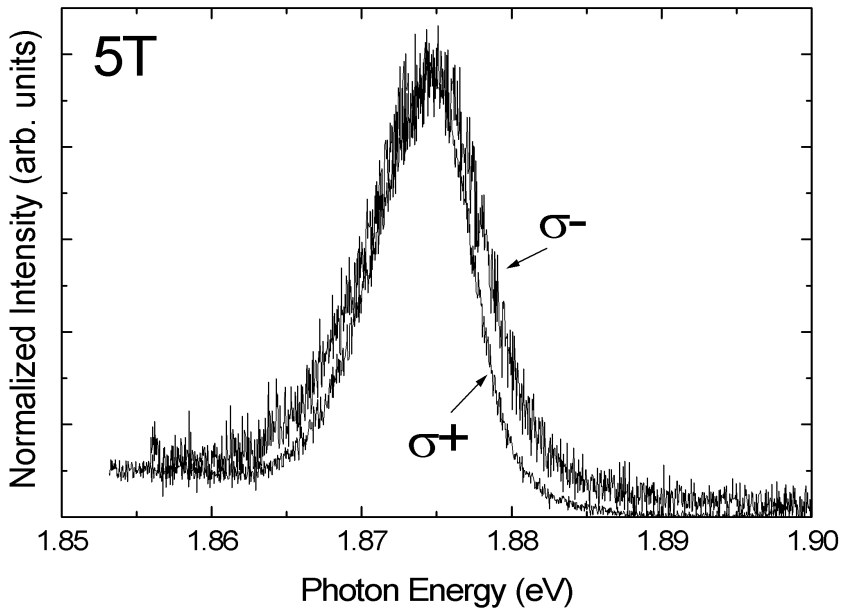


Figure 5.25: $\sigma^+$ and $\sigma^-$ circular polarized anti-Stokes spectra with magnetic field 5 T. Excitation energy is 800 nm (1.55 eV). The peak intensity is normalized.

besides, the width with low magnetic field is larger than that with high magnetic field as shown in Fig. 5.26. As shown in Fig. 5.26 the contribution $\sigma^+$ of the EMP transition is

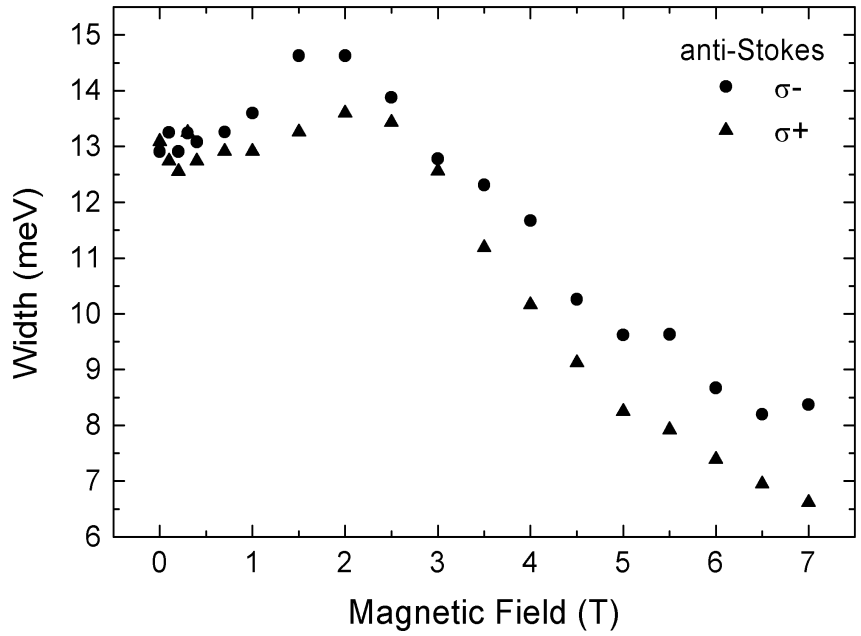


Figure 5.26: The width of $\sigma^+$ and $\sigma^-$ anti-Stokes photoluminescence as a function of magnetic field.

most important with low magnetic field. Due to these reabsorption processes the energy position in anti-Stokes photoluminescence is lower than that in photoluminescence under band-to-band excitation at even low magnetic field as shown in Fig. 5.27.

It can be seen that the peak position of $\sigma^+$ and $\sigma^-$ polarized photoluminescence under band-to-band excitation gradually become different with increasing magnetic field. This would be explained to be the effect of the Zeeman splitting and disappearance of MP effect. On the other hand for anti-Stokes photoluminescence the two polarized line peaks always appear in energy lower than that under band-to-band excitation at same energy with each other. This would be ascribed to the absorption of excitation light and reabsorption of anti-Stokes photoluminescence as well as above-mentioned two effects.

### 5.4.2 Resonant excitation

Fig. 5.28 shows the photoluminescence spectral evolution for various excitation powers under resonant excitation.

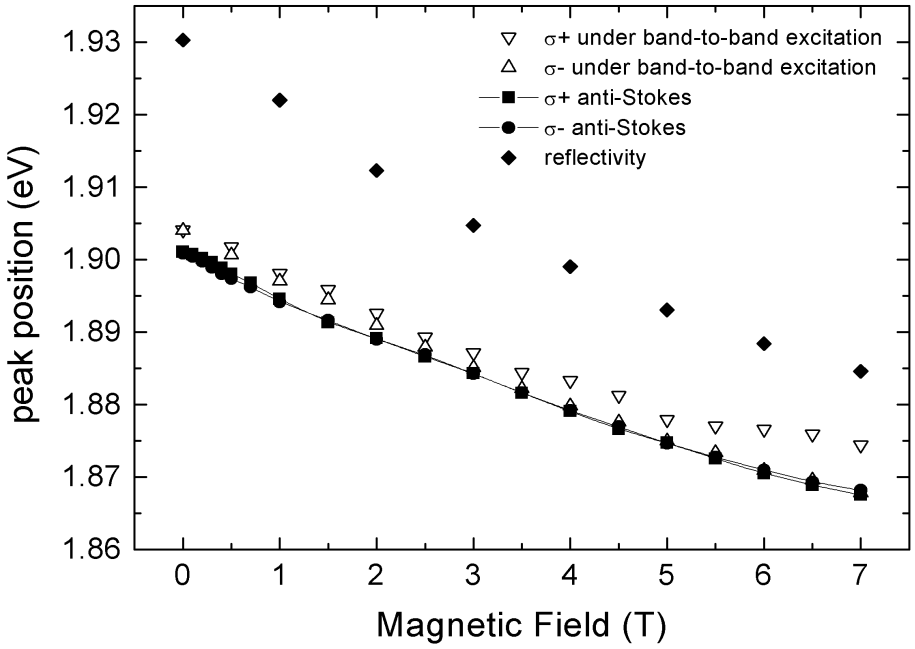


Figure 5.27: $\sigma^+$ and $\sigma^-$ peak position dependence on magnetic field for anti-Stokes photoluminescence and photoluminescence under band-to-band excitation.

In case of resonant excitation we can see not only anti-Stokes photoluminescence line but also another photoluminescence line that appear at lower energy side than the excitation energy. The behavior of this photoluminescence resembles that of the photoluminescence under band-to-band excitation. In Fig. 5.28 with increasing excitation power the peak positions of anti-Stokes and Stokes photoluminescence lines shift towards high energy. It can not be observed the dependence of these photoluminescence intensity and shape on the polarization of excitation light and photoluminescence. This is probably that the spin-memory is too small to measure compared with APF and MP effects. Especially the spin-memory of hole would vanish very quickly. Let us first discuss selective excitation in the band of localized exciton states. The photoluminescence line at lower energy than that of the excitation light is attributed to the localized EMP. By increasing excitation power we assume that partly the localized states with large spatial size and at high content of Mn would be saturated. As a result the contribution of only low energy MP is decreased in the photoluminescence line. Consequently the line is shifted towards

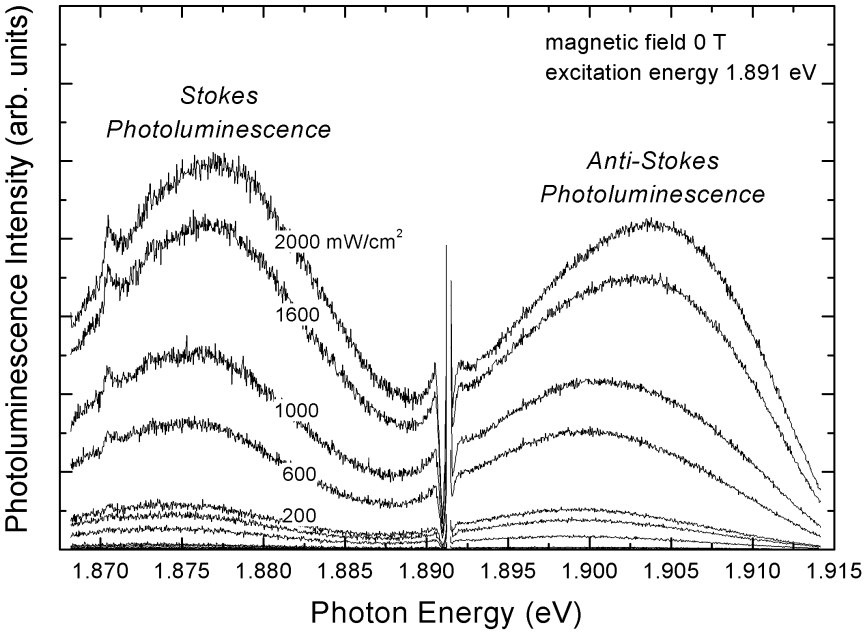


Figure 5.28: Stokes and anti-Stokes photoluminescence under resonant excitation at various excitation power.

high photon energy.

The anti-Stokes line is, as in non-resonant excitation, due to a two step process. It results from the superposition of the $A^0$XBMP and EMP lines. When increasing excitation power there is a saturation of the $A^0$X and the localized states of exciton with large spatial size and at high content of Mn. As a result, a shift of the line towards high energy could be occurred.

Let us consider the influence of reabsorption in the condition of resonant excitation. In this case, $\alpha_{exc}(\lambda_{exc})$ can not be neglected in Eq. (5.5) ( $\alpha(\lambda_{exc})$ and $\beta I$ are still negligible.). Then Eq. (5.5) can be written as

$$\frac{I_{B.to.B}}{I_{AS}}(\lambda) = C\frac{\alpha_{exc}(\lambda_{exc}) + \alpha(\lambda)}{\alpha_{exc}(\lambda_{exc})} = C\left(1 + \frac{\alpha(\lambda)}{\alpha_{exc}(\lambda_{exc})}\right), \tag{5.7}$$

where $C$ is arbitrary constant. Now $\alpha_{exc}(\lambda_{exc})$ can be obtained as follows. When $\lambda \cong \lambda_{exc}$,

$$\frac{I_{B.to.B}}{I_{AS}}(\lambda \cong \lambda_{exc}) = C\left(1 + \frac{\alpha(\lambda \cong \lambda_{exc})}{\alpha_{exc}(\lambda_{exc})}\right) = 2C. \tag{5.8}$$

Therefore we can get:

$$\frac{\alpha(\lambda)}{\alpha_{exc}(\lambda_{exc})} = 2\frac{I_{B.to.B}}{I_{AS}}(\lambda)\cdot\frac{I_{AS}}{I_{B.to.B}}(\lambda_{exc}) - 1. \tag{5.9}$$

In Fig. 5.29 Eq. (5.9) is plotted. As expected the curves are more or less parallel. They represent the absorption coefficient of the material in case of the selective excitation.

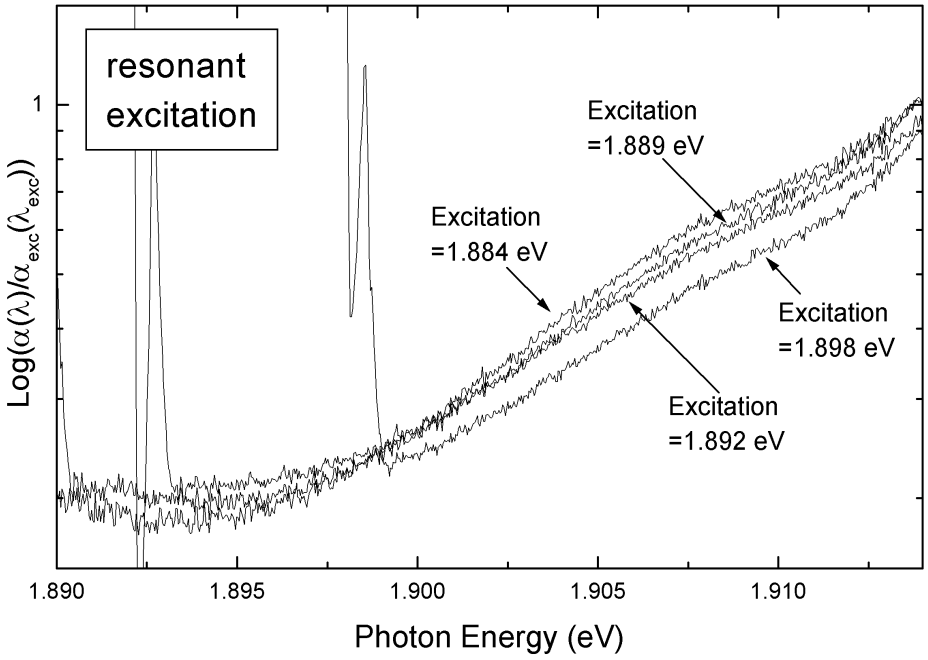


Figure 5.29: Logarithmic ratio of the absorption coefficients between $\alpha$ and $\alpha_{exc}(\lambda_{exc})$ under resonant excitation at various excitation energies.

# Chapter 6

# Conclusion

We have investigated the photoluminescence spectra of $Cd_{0.8}Mn_{0.2}Te$ single crystal as a function of temperature, magnetic field, excitation power, and excitation energy. From the lineshape analysis of the photoluminescence spectra, it has been found that the photoluminescence peak under band-to-band excitation is composed of two components. It has been understood that the higher energy component ($\sigma^+$ polarization) is ascribed to EMP, while the lower energy one ($\sigma^-$ polarization) is due to deep $A^0$XBMP recombination. These results have been obtained by taking into account the giant Zeeman splitting of localized exciton and bound exciton to acceptor. From this consideration the MP effect would completely fade at 4T and 3T for EMP and $A^0$XBMP, respectively. For EMP it has been evaluated that the localization energy due to MP effect and APF are equal to 15 meV and 11 meV, respectively. Therefore in this material it has been concluded that contribution of both effects to the exciton localization would be comparable in energy. We have also considered the value of $A^0$XBMP by varying the exchange integral $N_0\beta$ for a bound hole in deep acceptor. By theoretical analysis of the peak position at various magnetic fields it has been deduced $N_0\beta = 0.35$ eV. This value is half of one for bound hole in shallow acceptor (0.65 eV). This is because the number of Mn ion spins with which a hole bound to deep acceptor can interact is less than that to shallow acceptor, since the binding energy of the former should be much larger than that of the latter.

The anti-Stokes photoluminescence has been also observed under excitation at energies lower than or equal to the dominant peak energy of the photoluminescence observed under band-to-band excitation. In case of non-resonant excitation the anti-Stokes line has resulted from the superposition of the $A^0$XBMP and EMP lines through a two step process. However, the excitation power dependence of the integrated photoluminescence

intensity has been found less than 2 because of the saturation of deeply localized states with small density of states. Due to reabsorption effects both lines appear at lower energy than the photoluminescence under band-to-band excitation. According to the theoretical consideration of the absorption of excitation light and reabsorption of anti-Stokes photoluminescence, EMP line is more absorbed in the medium than $A^0$XBMP line with increasing magnetic field. This is due to the vanishing of the MP effect. In case of resonant excitation not only anti-Stokes photoluminescence but also another photoluminescence line that appear at lower energy side than the excitation energy have been observed. The former line results from the superposition of the $A^0$XBMP and EMP lines while the latter is attributed to only EMP. With increasing excitation power the peak positions of both photoluminescence shift towards high energy. This is due to a saturation of the $A^0$X and the localized states of exciton with large spatial size and at high content of Mn.

This study would contribute to the possibility of photo-induced magnetization for application, e.g. delicate control of circular polarization, applied magnetic field, and temperature. Through the anti-Stokes photoluminescence it would be very important to investigate the state of the Mn ion spins. This is because the exciton would modify the Mn ion spin state when the exciton exists at intermediate state in the two-step process. Furthermore it must be essentially understood the complex effects due to EMP and $A^0$XBMP.

# Part II

# Magnetic flux patterns in the intermediate state of thin type-I superconductors

# Chapter 7

# Historical background

## 7.1 History

In 1911, H. Kamerlingh Onnes found that below 4.15K the resistance of mercury dropped to zero (zero-resistance), which was the discovery of superconductivity (type-I superconductor). Twenty-two years later, in 1933, Meissner and Ochsenfeld found that when a spherical superconductor is cooled down to its transition temperature in a magnetic field, it excludes the magnetic flux (perfect diamagnetism). The report of the perfect diamagnetism led the London brothers *et al.* to propose equations that explain this effect and predict how far a static external magnetic field can penetrate into a superconductor. The next theoretical advance came in 1950 with the theory of V. L. Ginzburg and L. D. Landau, which described superconductivity in terms of an order parameter and provided a derivation for the London equation (Ginzburg-Landau theory). A present theoretical understanding of the nature of superconductivity is based on the BCS microscopic theory proposed by J. Bardeen, L. Cooper, and J. R. Schrieffer in 1957. The Ginzburg-Landau and London results fit well into the BCS formalism. In the same year unprecedented superconductor (type-II superconductor) was discovered by A. A. Abrikosov. This kind of superconductors has mixed phase where the magnetic flux is able to penetrate in quantized units by forming cylindrically symmetric domains between the lower critical magnetic field and upper critical magnetic field. The difference between type-I and type-II superconductor can be explained with the penetration depth $\lambda$ by which the exponential drop of magnetic field is characterized, and the coherence length $\xi$ which is the range of interaction creating the superconducting state. In type-I superconductors the coherence length is large $\xi > \lambda$, while $\xi < \lambda$ is true for type-II superconductors. Therefore the

thickness of the interface ($\Delta \propto \xi - \lambda$) and the interfacial energy of type-I superconductors are positive. In 1986, a breakthrough in materials, namely, high-temperature superconductivity was discovered by J. G. Bednorz and K. A. Müller. These materials are type-II superconductors. In recent years many other types of superconductors have been studied, particularly the heavy fermion systems.

For this study, it is very important to mention especially the history of research on the intermediate state in type-I superconductors. In the 1970's, a lot of experimental studies were demonstrated with Faraday microscopy and there were many evidences of flux tubes array, flux lamella pattern, and labyrinthine pattern[84][85]. But there were no analysis on the domain structure transition between each patterns. In the 1980's and the beginning of the 1990's, very few studies were reported on the intermediate state. As for the dynamics of flux pattern, a few papers were published[86][87][88][89][90].

## 7.2 Meissner effect

One of the most important properties of the superconductor is perfect diamagnetism called 'Meissner effect'. Below the critical temperature and critical magnetic field the superconductor exhibits perfect diamagnetism. The critical magnetic field decreases with increasing temperature, empirically according to the law,

$$H_c(T) \approx H_c(0)\left(1 - \frac{T^2}{T_c^2}\right), \tag{7.1}$$

where $H_c(T)$ is the critical magnetic field at the temperature $T$, and $T_c$ is the critical temperature.

Table 7.1 shows the critical magnetic field $H_c(0)$ and the critical temperature $T_c$ of the superconducting elements[91].

Table 7.1: Values of $H_c(0)$ and $T_c$ of the superconducting elements.

| | Zn | Cd | Hg | Al | Ga | In | Tl | Sn | Pb |
|---|---|---|---|---|---|---|---|---|---|
| $H_c(0)$(mT) | 5.3 | 3.0 | 41.1 | 9.9 | 5.1 | 28.3 | 16.2 | 30.6 | 80.3 |
| $T_c$(K) | 0.88 | 0.56 | 4.15 | 1.19 | 1.09 | 3.41 | 1.37 | 3.72 | 7.18 |

## 7.3 Intermediate state in type-I superconductors

Intermediate state in type-I superconductors is a mixed state consisting of fully diamagnetic, superconducting domains and normal state, flux-bearing domains. They can be observed in slabs placed in a perpendicular magnetic field as explained below.

In case of a long, thin cylindrical superconductor in parallel external magnetic field, the magnetic field $H$ at the surface equals the applied magnetic field. For other geometries, the magnetic field at a certain part of the surface will exceed the applied magnetic field, as is illustrated in Fig. 7.1. In case of a spherical superconductor the magnetic

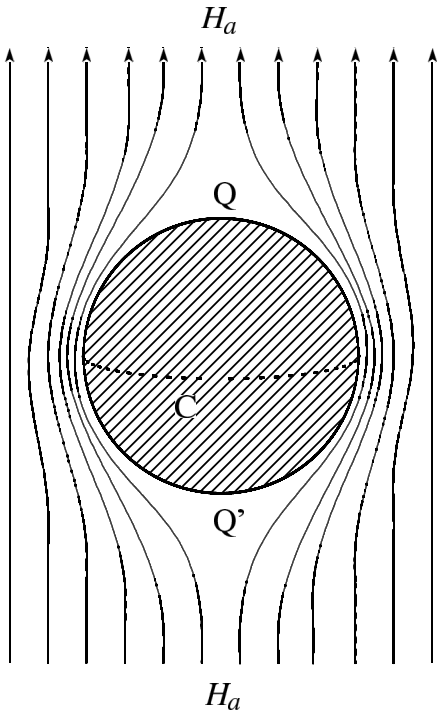


Figure 7.1: The magnetic field distribution around the superconducting sphere. For applied magnetic field $H_a$ less than $\frac{2}{3}H_c$, there is a complete Meissner effect and the magnetic field at the equator (at any point circle C) is $\frac{3}{2}H_a$, the magnetic field at the poles (Q,Q') is zero. For $\frac{2}{3}H_c < H_a < H_c$, the sphere is in the intermediate state.

field at the equator is $3/2$ of the applied magnetic field $H_a$ therefore there must be a coexistence of superconducting and normal regions for $2/3 < H_a/H_c < 1$ . By using the demagnetizing factor $\eta$, the intermediate state is observed in the following range:

$$1-\eta < \frac{H_a}{H_c} < 1. \tag{7.2}$$

The demagnetizing factor is found equal to 0 for the long, thin cylinder or thin plate in a parallel magnetic field, to 1/3 for a sphere, to 1/2 for a cylinder in a transverse magnetic field.

In case of the flat slab (film) in a perpendicular magnetic field, the demagnetizing factor for this case is $\sim$1. Therefore the intermediate state can be nearly always seen.

At very low applied magnetic field compared with $H_c$ the sample is in the complete diamagnetic state: the magnetic flux is totally expelled. Due to the demagnetizing factor, the local magnetic field near the sharp edges of the sample is larger than the applied magnetic field and reaches the critical magnetic field for a very low value of the applied magnetic field. Then the magnetic flux can start to penetrate in the sample with further applied magnetic field up to the complete transition to the normal state.

The morphology of observed patterns consists in coexisting normal state domains with cylindrical shape (bubbles) and branched/intricate fingered shape (lamellae) surrounded by superconducting matrix as shown in the schematic drawing of Fig. 7.2. Pattern formation is essentially due to the competition between long-range forces between domains and short-range forces described by an interfacial tension between the two phases. The former is due to the repulsive magnetic interaction between flux bearing domains. It tends to distribute the magnetic flux into a large number of small size domains in order to minimize the curvature of magnetic field lines above and below the sample. On the other hand the interfacial tension tends to gather all the flux in a single domain in order to minimize the interface length.

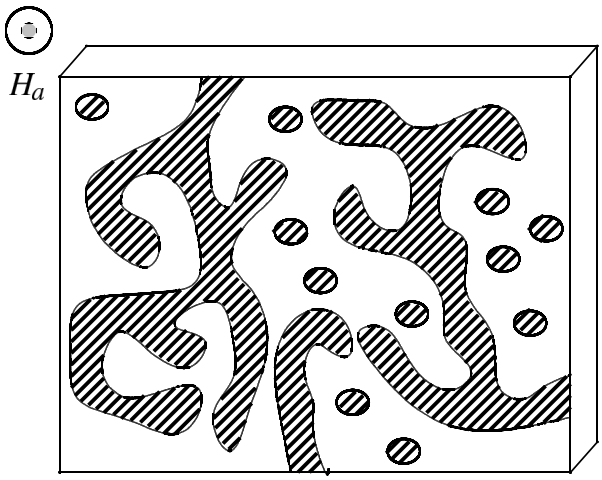


Figure 7.2: A thin slab of type-I superconductor viewed along the applied magnetic field $H_a$. Dark regions represent normal state.

# Chapter 8

# Motivation, purpose, and research plan

As we mentioned in Sec. 7.1, in the 80's and the beginning of 90's, very few studies of the intermediate state were reported. In 1996, there were renewed studies about the intermediate state from the theoretical side[92]. In those days the domain structures and comparison of different kinds of systems were studied[92][93][94][95][96]. Nowadays the improvement of the Faraday imaging technique with novel magneto-optic layers makes it possible to study the flux pattern with high resolution[97][98]. This kind of study will be possibly extended towards investigation of the flux dynamics in type-I superconductors. Furthermore, it is potentially useful for the understanding of magnetic flux jumps caused by vortex bundles, in conventional as well as high-$T_c$ superconductors.

The purpose of our study is to investigate the flux tube pattern formation in the intermediate state of type-I superconductors with the high resolution Faraday imaging technique. The most important questions are the formational mechanism of the shape of flux tubes array and the cause of their size. This study will be applied to the analysis of the transformation from flux tubes to lamellae.

## Research plan

Our research plan consists of 3 steps as follows.

1. Design, optimization and fabrication of the sample with the magneto-optic layers.
2. Design and optimization of the cryostat.
3. Study of the magnetic flux patterns in the intermediate state of type-I superconducting thin indium and lead films.

Through this study, we should compare the experimental results and the predictions of models. Moreover, the key parameters that control the flux tube and lamella size should be determined towards better understandings of flux penetration mechanism.

# Chapter 9

# Theoretical background

There are several models that analyze the magnetic flux patterns in the intermediate state of type-I superconductors. A theoretical consideration of the intermediate state structure in type-I superconductors was first given by Landau in 1937 (Landau model)[99]. In 1971 a highly simplified but useful model of the intermediate state patterns were proposed by R. N. Goren and M. Tinkham (Goren-Tinkham model)[100][101]. A next developed theory was proposed in 1996 by A. T. Dorsey and R. E. Goldstein[92][95] in which the normal state domains are modeled as current loops (Current Loop model). This model is shown to be equivalent to the Surface Charge model[102]. Since transition between normal state and superconducting state is assumed to be reversible, each model considers the thermodynamic free energy to find the size and shape of the superconducting and normal regions. In this section, these models, which consider an infinite flat slab of thickness $d \gg \lambda$ in a perpendicular magnetic field, are reviewed. An extension of the Current Loop model, the Constrained Current Loop model, very recently developed for superconductors, will be also presented[102].

## 9.1 Landau model for magnetic flux lamellae

In the Landau model the intermediate state is assumed to have an one-dimensional periodic lamella structure, in which the normal lamellae near the surface broaden in order to reduce the magnetic energy above the surface as sketched in Fig. 9.1.

Such structures arise from a competition between the magnetic energy, the condensation energy of the superconducting regions, and the interfacial energy between the normal and superconducting regions. In this theory the energy of normal regions is regarded as

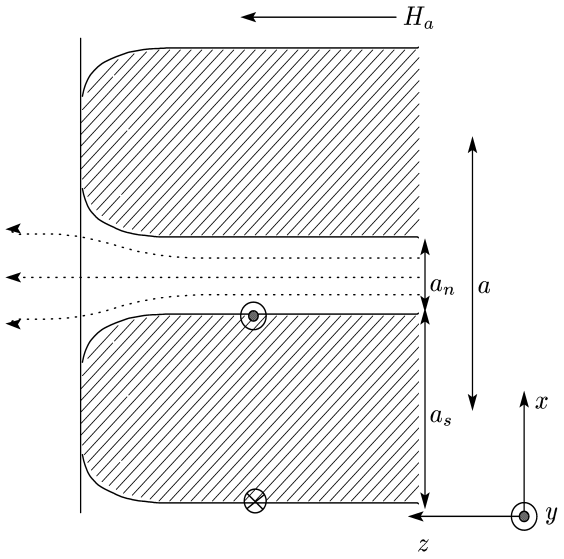


Figure 9.1: Lamellae in the intermediate state. Superconducting regions are shaded.

zero.

The condensation energy per area is[99]

$$\frac{E_c}{A} = -\frac{H_c^2 d}{8\pi} + \frac{H_c^2 d}{8\pi}\left\{\frac{a_n}{a} + \frac{a}{d} f_c\left(\frac{H_a}{H_n}\right)\right\}, \tag{9.1}$$

with

$$f_c(h) = \frac{1-h^2}{2\pi}[(1+h)^2\ln(1+h) + (1-h)^2\ln(1-h) - (1+h^2)\ln(1+h^2)], \tag{9.2}$$

where $d$ is sample thickness, $H_a$ is applied magnetic field, $H_n$ is the magnetic field at normal region. The third term is due to the condensation energy lost from the thinning of superconducting regions near the slab surfaces.

The magnetic energy per area is[99]

$$\frac{E_m}{A} = \frac{H_a^2}{8\pi} L_z + \frac{H_n H_a}{8\pi} d + \frac{H_n^2}{4\pi} a f_{mag}\left(\frac{H_a}{H_n}\right), \tag{9.3}$$

with

$$f_{mag}(h) = \frac{h}{2\pi}[(1+h)^3\ln(1+h) - 2h\ln(8h) - (1-h)^3\ln(1-h) \\ -h(1+h^2)\ln(1+h^2)], \tag{9.4}$$

where $L_z$ is some large distance away from the top surface of the sample. The first term in Eq. (9.3) is the energy of the external magnetic field in the absence of the sample, the second is the bulk magnetic energy of a uniformly magnetized sample and the third arises from demagnetizing magnetic field.

The interfacial energy is phenomenologically given

$$\frac{E_{int}}{A} = \frac{H_c^2}{8\pi}\frac{2\Delta d}{a}, \tag{9.5}$$

where $\Delta$ is the width of the interfaces.

Summing these contributions and using flux conservation $a_n H_n = aH_a$, the free-energy density (the energy per area) is

$$\begin{aligned}\frac{E}{A} = \frac{H_a^2}{8\pi}L_z &+ \frac{H_c^2 d}{8\pi}\left[-1+\left\{\frac{a_n}{a}+\left(\frac{H_a}{H_c}\right)^2\frac{a}{a_n}\right\}\right. \\ &+ \left. 2\left(\frac{\Delta}{a}+\frac{a}{d}\left\{\frac{1}{2}f_c\left(\frac{H_a}{H_n}\right)+\left(\frac{H_n}{H_c}\right)^2 f_{mag}\left(\frac{H_a}{H_n}\right)\right\}\right)\right].\end{aligned} \tag{9.6}$$

It is difficult to minimize this expression with respect to both $a_n$ and $a$. The usual procedure is to minimize the bulk terms with respect to $a_n$ which yields $H_n = H_c$: the magnetic field in the normal areas is equal to the critical magnetic field. Then we substitute $H_n$ by $H_c$ in the expression of the energy and we minimize with respect to $a$. The equilibrium period of the intermediate-state structures is obtained by minimizing the free energy with respect to $a$:

$$a = \sqrt{\frac{d\Delta}{f_L(H_a/H_c)}}, \tag{9.7}$$

where $f_L(h)$ is

$$\begin{aligned} f_L(h) &= \frac{1}{2}f_c(h)+f_{mag}(h) \\ &= \frac{1}{4\pi}[(1+h)^4\ln(1+h)+(1-h)^4\ln(1-h)-(1+h^2)^2\ln(1+h^2)-4h^2\ln(8h)]. \end{aligned} \tag{9.8}$$

Since the mathematical techniques to solve the problem of the one-dimensional lamellae array cannot be used for a two-dimensional tubes array, this model is not appropriate for the tubes array.

## 9.2 Goren-Tinkham model for magnetic flux tubes and lamellae

First, as shown in Figure 9.2, the intermediate state at the surface of a sample with thickness $d$ is assumed to consist of a triangular array of normal flux tubes spaced a distance $a$ apart. They are hexagonal in shape with width $D$ in order to insure that they are close packed at the critical magnetic field. The equilibrium period of this spot pattern is found

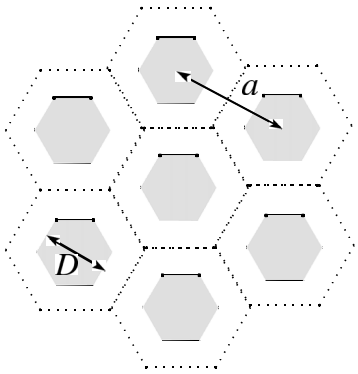


Figure 9.2: Triangular array of hexagonal normal tubes, shown shaded.

by minimizing the following two $a$-dependent terms in the total free energy.

1. the surface energy $E_1$ of the normal-superconducting interfaces,

$$E_1 = \frac{\Delta H_c^2}{8\pi} \times \left\{ \begin{array}{c} \textit{the area of the interface} \\ \textit{between normal and superconducting regions} \end{array} \right\} = \frac{H_c^2 \Delta D d}{2\pi a^2}, \tag{9.9}$$

   where $H_c(\approx H_n)$is the magnetic field at normal region, $\Delta(\propto \xi - \lambda)$ is the thickness of the interface.

2. the energy $E_2$ due to magnetic field distortion near the sample surface,

$$E_2 = \frac{H_c^2}{8\pi}\rho_n(1-\rho_n) \times 2L = 2L\frac{H_c^2}{8\pi}\rho_n\rho_s, \tag{9.10}$$

   where $\rho_s(=1-\rho_n)$ is the fraction of the superconducting surface area, $L$ given below is the height above the surface in which the magnetic field inhomogeneity is greatly reduced on both sides of the sample (see figure 9.3). It is approximately given by:

$$L \simeq \left(\frac{1}{a_s} + \frac{1}{a_n}\right)^{-1} \simeq \left(\frac{1}{D} + \frac{1}{a-D}\right)^{-1}. \tag{9.11}$$

The loss of condensation energy due to broadening of the normal regions near the sample surfaces is neglected here since the result of this contribution is small.

The total $a$-dependent free energy is found as

$$E_1 + E_2 = \frac{H_c^2}{8\pi}\left\{\frac{4\Delta D d}{a^2} + \frac{2D(a-D)}{a}\rho_n\rho_s\right\}. \tag{9.12}$$

Minimizing the sum with respect to $a$, the equilibrium spacing and diameter is given

$$a(h)^{tube} = \left(\frac{2d\Delta}{h(1-h)(1-\sqrt{h})}\right)^{\frac{1}{2}}, \qquad D(h) = h^{\frac{1}{2}}a(h), \tag{9.13}$$

where $h$ is the reduced magnetic field ($h = D^2/a^2 = H_0/H_c = \rho_n$).

From these equations, we can roughly estimate the behavior of spacing and diameter as a function of reduced magnetic field,

$$\begin{aligned} a &\rightarrow \sqrt{\frac{2d\Delta}{h}}, \quad D \rightarrow \sqrt{2d\Delta} \quad (h \rightarrow 0), \\ a &\rightarrow \infty, \qquad\qquad D \rightarrow a \qquad\quad (h \rightarrow 1). \end{aligned} \tag{9.14}$$

Next, the lamella intermediate shape (Figure 9.3) is calculated with the same procedure,

$$E_2^{lamella} = \frac{H_c^2}{4\pi}\rho_n^2\rho_s^2 a, \tag{9.15}$$

where $a = a_s + a_n$. Then the equilibrium spacing for the case of normal lamellae is given

$$a(h)^{lamella} = \frac{\sqrt{d\Delta}}{\rho_n\rho_s} = \frac{\sqrt{d\Delta}}{h(1-h)}. \tag{9.16}$$

Compared with Landau model, the magnitude of the difference in free energy is very small. The free energy of tubes and lamellae are expressed as followed

$$E^{lamella} = \frac{H_c^2}{2\pi}\sqrt{d\Delta h^2(1-h)^2}, \tag{9.17}$$

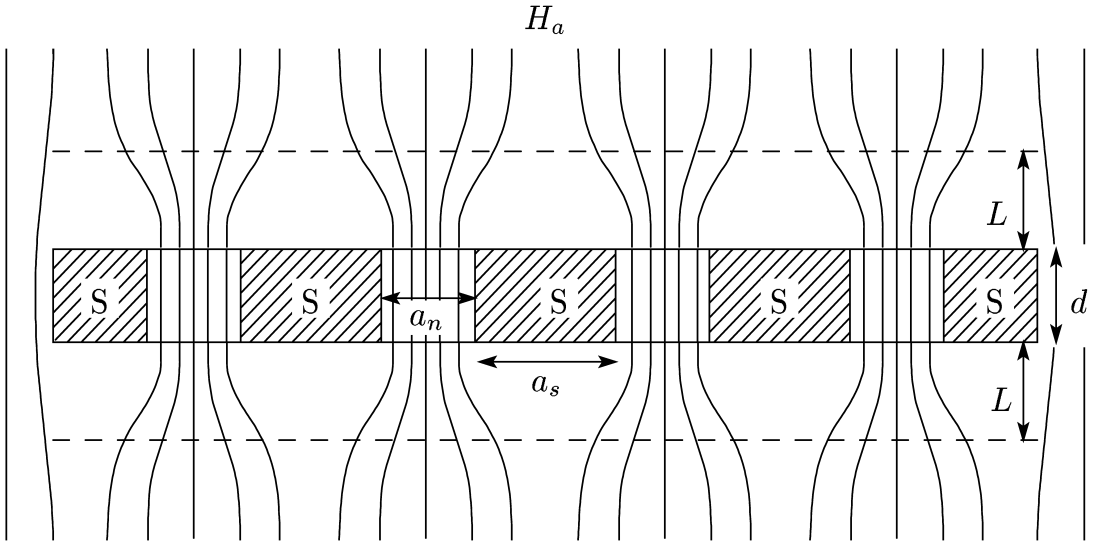


Figure 9.3: Schematic drawing of magnetic flux through the sample in the intermediate state. Flux density is $H_a$ at large distances, zero in the superconducting regions (shown shaded), and $H_n$ ($\approx H_c$) in the normal regions.

$$E^{tube} = \frac{H_c^2}{2\pi}\sqrt{2d\Delta h^2(1-h)(1-\sqrt{h})}. \tag{9.18}$$

For both flux-pattern geometries, surface energies ($E_1$ and $E_2$) are equal for all $d$ when the pattern spacing has adjusted to optimum value. Thus it can be found that optimally sized flux tubes are so close in energy to lamella layers that it is not possible to determine the ground state of the system. The path of the flux entering the sample can be important in determining the flux pattern. Therefore, further detailed calculation is needed to analyze a transformation from flux tubes to flux lamellae structures.

## 9.3 Current Loop model

The Current Loop model was introduced by Dorsey and Goldstein[95]. In this model the intermediate state pattern is considered as a set of domains of any shapes with straight domain walls. Supercurrents that provide the screening of the applied magnetic field flow along the normal superconducting interfaces. They are confined in a thickness of the order of $\lambda$, considered as negligible compared with other distances. The domains are interacting with each other due to the magnetic fields created by these currents. This

interaction is calculated as if these currents were interacting in the free space. Surface supercurrents that flow along the slab top and bottom surfaces are neglected. The Current Loop model allows to consider problems which are impossible to solve by the previous models, for example the tube-to-lamella transition.

In the macroscopic approach, the total free energy $E$ of a configuration of flux domains arises from the condensation energy $E_c$, the interfacial energy $E_{int}$, and the magnetic energy $E_m$. Then the total free energy is $E = E_c + E_{int} + E_m$. $E_c$ and $E_{int}$ are

$$E_c = V\frac{H_c^2}{8\pi}\rho_n, \qquad E_{int} = \frac{H_c^2}{8\pi}\Delta d\sum_i L_i, \tag{9.19}$$

where $V$ is the total volume containing the two phases, $H_c$ is the critical magnetic field, $\rho_n = A_n/A$ is the area fraction of the normal phase, $\Delta$ is the width of the interfaces, $d$ is the sample thickness, $L_i$ is the perimeter of the superconducting zones.

In this model, the magnetic energy inside the sample is calculated with the interactions of screening currents flowing at the interfaces between the normal and superconducting zones. The direction of the flow is so as to cancel the applied magnetic field in the superconducting regions and augment it in the normal regions. Therefore, the magnetic energy is computed as a sum of three terms:

$$E_m = \frac{H_a^2}{8\pi}V + \frac{H_nH_a}{4\pi}(1-\rho_n)V - \frac{M^2}{2}\sum_{ij}\int_0^d dz\int_0^d dz'\oint ds\oint ds'\frac{\vec{t}_i\cdot\vec{t}_j}{R_{ij}}, \tag{9.20}$$

where $M = -H_n/4\pi$ is the domain magnetization in the presence of the external magnetic field, $\vec{t}_i$, $\vec{t}_j$ are the unit vectors tangent to the current flow (see appendix B.1). The first term is the energy due to the magnetic field without the sample, the second is due to the interaction between $H_a$ and the supercurrent, and the third is ascribed to the self- and mutual interaction of the supercurrent. The free-space current-current interaction is Coulombic, with $R_{ij} = \{[\vec{r}_i - \vec{r}_j]^2 + (z-z')^2\}^{\frac{1}{2}}$. Performing the $z$ and $z'$ integrals, the magnetic energy becomes[95]

$$E_m = \frac{H_a^2}{8\pi}V + \frac{H_nH_a}{4\pi}(1-\rho_n)V - M^2d\sum_{ij}\oint ds\oint ds'\vec{t}_i\cdot\vec{t}_j\Phi(R_{ij}/d). \tag{9.21}$$

$\Phi(R/d)$ is the potential,

$$\begin{aligned}\Phi(R/d) &= \frac{1}{2d}\int_0^d dz\int_0^d dz'[R^2+(z-z')^2]^{-\frac{1}{2}} \\ &= \sinh^{-1}(d/R) + R/d - \sqrt{1+(R/d)^2},\end{aligned} \tag{9.22}$$

where $R = |\vec{r} - \vec{r'}|$ the in-plane vector between points. In Sec.11.3.2 we shall use Eq. (9.19),(9.20) to calculate the energy of the flux tube lattice. This model leads to an analytical expression of the energy. Unfortunately this expression contains a slowly converging series (see appendix B.2). From the point of view of numerical calculation the equivalent Surface Charge model, which is presented in the next section, is more appropriate.

## 9.4 Surface Charge model

It is well known in magnetostatics that the magnetic field created by a distribution of surface currents (or equivalently by a uniformly magnetized medium with magnetization $M$) can be obtained from the electric field that would created by the same medium with unit volume charge. A uniformly polarized medium with polarization $\vec{P}$ can be equivalently described by a distribution of surface charges with surface charge density $\sigma = \vec{P} \cdot \vec{n}$. Therefore the current loops which circulate on the interfaces between normal and superconducting regions in the intermediate state can be also replaced by a collection of domains with virtual magnetic surface charges on the top and bottom surfaces. With this model the magnetic energy can be expressed by the magnetic scalar potential $\psi$ which includes the sum of two explicit single layer potentials created by the surface charges with densities $\pm H_n/4\pi$ at $z = 0$ and $z = d$, respectively:

$$\psi = -\frac{H_n}{4\pi} \int \frac{dS'}{\{(\vec{r} - \vec{r}')^2 + (z-d)^2\}^{1/2}} + \frac{H_n}{4\pi} \int \frac{dS'}{\{(\vec{r} - \vec{r}')^2 + z^2\}^{1/2}}. \tag{9.23}$$

Due to $\vec{H} = \nabla\psi$ the magnetic energy $E_m$ can be written as:

$$\begin{aligned} E_m &= \frac{H_a^2}{8\pi} V + \frac{H_n H_a}{4\pi}(1-\rho_n)V - \frac{1}{8\pi}\int \vec{H}^2 \, dV \\ &= \frac{H_a^2}{8\pi} V + \frac{H_n H_a}{4\pi}(1-\rho_n)V - M^2 \iint \left( \frac{1}{\vec{r} - \vec{r}'} - \frac{1}{\{(\vec{r} - \vec{r}')^2 + d^2\}^{1/2}} \right) dS' dS, \end{aligned} \tag{9.24}$$

where $M = -H_n/4\pi$ is the effective magnetization of the normal phase. This equation leads to an easier calculation of the magnetic energy than with the Current Loop model. This model enables us to compare the free energies of the tube and the lamella lattice,

which is impossible in Landau or Goren-Tinkham models. Moreover, a tube-to-lamella transition can be predicted to occur when the volume fraction of the normal state increases.

## 9.5 Constrained Current Loop model

In both the Current Loop model and the Surface Charge model the domains are interacting with each other as in the free space. As it was already mentioned the Current Loop model as well as the equivalent Surface Charge model neglect the screening currents flowing along the top and bottom surface of the slab in the superconducting regions as shown in left sketch of Fig. 9.4. These currents actually prevent the magnetic field created in the normal regions from penetrating in the superconducting regions as shown in right sketch of Fig. 9.4.

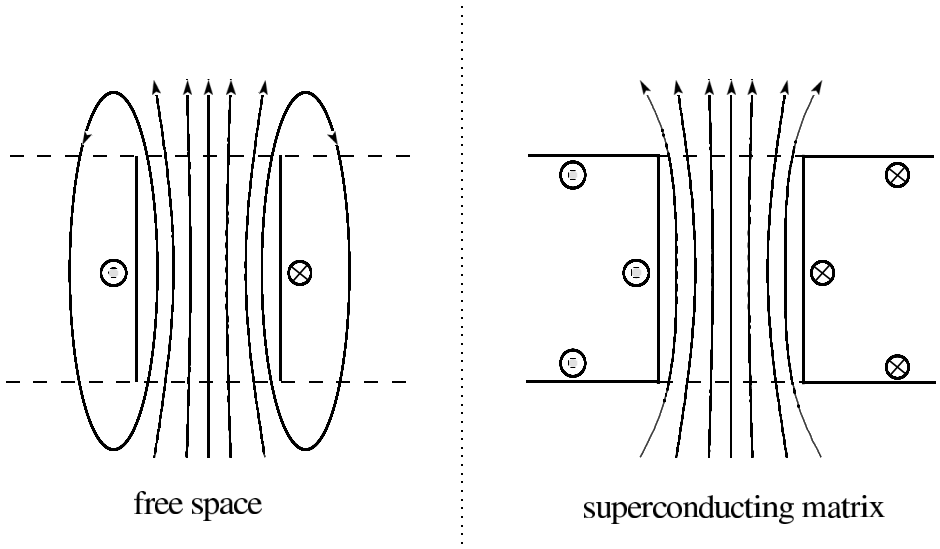


Figure 9.4: Schematic drawing of local magnetic field in the vicinity of the flux tube in the free space (left) and in a superconducting matrix (right).

The Constrained Current Loop model, which is a modification of the Current Loop model and Surface Charge model, can easily deal with the effect of surface screening on the top and bottom surfaces of the superconducting regions by taking into account only the magnetic interaction between surface charges of same face. This is realized by taking $d \to \infty$ in Eq. (9.23) (9.24). Therefore this model is named Constrained Current Loop

model due to this limit. As we shall see in Sec. 11.4.3, the Constrained Current Loop model provides much better agreement with the experimental results than the previous models especially for thin samples.

# Chapter 10

# Experiments

## 10.1 Concept of magneto-optical measurement

The magnetic flux patterns in the intermediate state have been experimentally studied by various techniques,

1. moving a tiny magnetoresistive or Hall effect probe over the surface,
2. making powder patterns with either ferromagnetic or superconducting (diamagnetic) powders (Bitter decoration technique),
3. using the Faraday magneto-optic effect in transparent magnetic materials in contact with the surface of a superconducting film as magneto-optic layer (MOL).

In order to get a high-resolution image of the magnetic flux pattern, one of these methods, Faraday microscopy (the above 3.), is the most useful[97][98]. A schematic drawing of the Faraday imaging technique is shown in Figure 10.1.

The linearly polarized light enters the MOL in which the Faraday effect occurs and is reflected at the mirror layer. In areas without flux, no Faraday rotation takes place. This light is not able to pass the analyzer that is set in a crossed position with respect to the polarizer, hence the superconducting regions stay dark in the image. On the other hand, in regions where flux is penetrating, the polarization plane of the incident light is rotated by Faraday effect so that some light passes through the crossed analyzer, thus the normal areas will be brightly imaged.

Fig. 10.1 shows the case of non-zero reflection angle, whereas in the experiment it is usual to use perpendicular incident light (Faraday configuration).

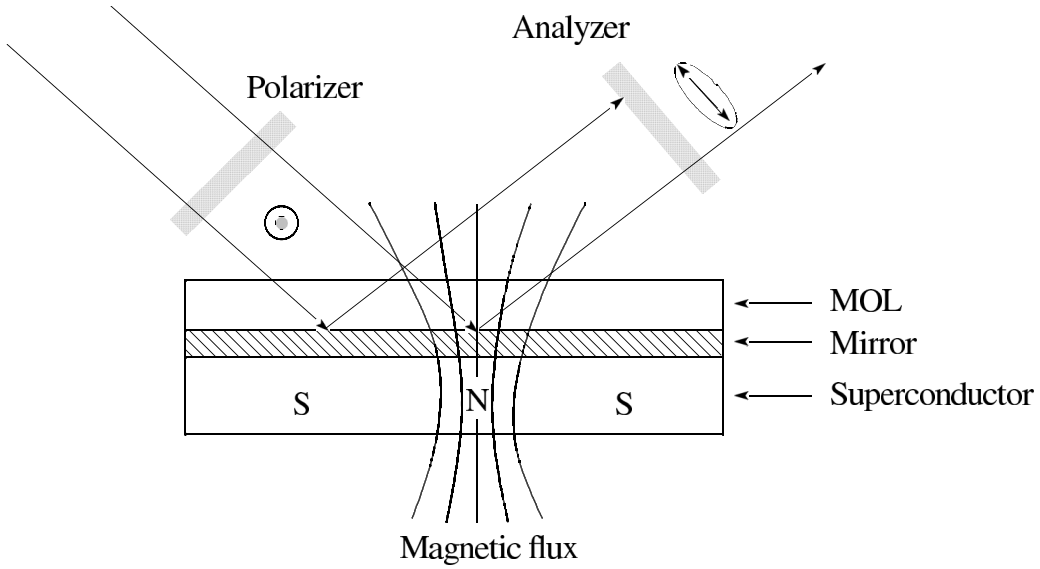


Figure 10.1: Schematic drawing of the Faraday effect.

The Faraday rotation angle is transformed into light intensity levels. The sample surface is imaged onto a CCD detector array. In case of crossed polarizer and analyzer the intensity of the signal out of the CCD detector is

$$I(r,\lambda,B) = I_0(r,\lambda)\sin^2(\theta_F(r,\lambda,B)) + I_1(r,\lambda), \tag{10.1}$$

where $r$ is the spatial coordinate on the CCD surface, $\lambda$ is the wavelength of incident light, $B$ is the applied magnetic field, $\theta_F$ is the Faraday angle, and $I_0$ is the light intensity reflected by the sample. $I_1$ is the background signal ascribed to the dark signal of CCD and residual transmission of crossed polarizer and analyzer. When the analyzer is uncrossed by $\theta$,

$$I(r,\lambda,B) = I_0(r,\lambda)\sin^2(\theta + \theta_F(r,\lambda,B)) + I_1(r,\lambda). \tag{10.2}$$

The angular position $\theta$ of the analyzer should be adjusted to obtain the best contrast between superconducting ($\theta_F = 0$) and normal ($\theta_F \neq 0$) areas. Changing the sign of $\theta$ normal areas can appear brighter or darker than superconducting areas. In our experiment the angle $\theta$ is set to get black normal areas and gray superconducting areas.

## 10.2 Magneto-optic layers

### 10.2.1 Conventional magneto-optic layers

As for the typical conventional MOLs, essentially, thin layers of Eu-based MOL (Eu chalcogenides, e.g. EuS and $EuF_2$ mixtures, EuSe) and doped yttrium iron garnet (YIG) films have been used[103]. Eu compounds are usable up to critical temperature of ferromagnetic-paramagnetic transition ($\sim 15-20$ K) because their Verdet constants decrease with increasing temperature. Garnets can be used up to room temperature.

Since EuS undergoes ferromagnetic ordering below $T_c \approx 16.3$ K, a mixture of EuS with $EuF_2$ is better used. $EuF_2$ stays paramagnetic down to very low temperatures, therefore the ordering temperature of the mixture can be tuned by the ratio EuS : $EuF_2$. But there are several problems; difficulty of preparation due to difference of melting temperatures, and necessity of a co-evaporation technique.

Then the single-component EuSe layer has been further used because even in the bulk EuSe is paramagnetic down to 4.6 K and it has a larger Verdet constant. Below 4.6 K, EuSe becomes 'metamagnetic', however, the reappearance of magnetic domains in the EuSe layers is not seen down to 1.5 K. But there is also a problem owing to the toxicity of Se compounds.

On the other hand, due to their high transition temperature (Curie temperature), bismuth- and gallium-doped yttrium-iron garnets (YIG) have been developed and used for the study of high-$T_c$ superconductors. They are disadvantageous since they show ferrimagnetic domains, however, these MOLs are developed further by the introduction of ferrimagnetic garnet films with in-plane anisotropy. Using such films, the optical resolution is about 3 $\mu$m, but a direct observation of the magnetic flux patterns is possible and the advantages of the garnet films, i.e. high magnetic field sensitivity, large temperature range, are kept.

Generally this kind of MOL often has the demerit of poor spatial resolution because of the thickness of several micrometers. Furthermore, self-magnetic ordering that may modify the flux distributions in superconducting samples could limit their use. However, it was recently reported that an optimized ferrite garnet film allowed the observation of single flux quanta in superconducting $NbSe_2$[104].

### 10.2.2 Novel magneto-optic layers

In this section we refer to an alternative type of MOL[97][98] based on semimagnetic semiconductor (SMSC) $Cd_{1-x}Mn_xTe$ developed at Groupe de Physique des Solides (GPS). It consists of SMSC (or also called diluted magnetic semiconductor (DMS)) $Cd_{1-x}Mn_xTe$ quantum wells (QWs) embedded in a semiconductor-metal optical cavity. SMSC is well known to exhibit a large Faraday rotation mainly due to the giant Zeeman splitting of the excitonic transition ascribed to *sp-d* exchange interactions between spins of magnetic material and band electron spins. The most advantageous point is no self-magnetic ordering due to paramagnetic behavior of Mn ions. Therefore, it is very convenient since there is no possibility to modify the magnetic flux patterns of intermediate state of type-I superconductors. There are several other advantages of this MOL. It is easy to increase Faraday rotation by making an optical cavity (metal/semiconductor/vacuum) with a thickness $\simeq (2n+1)\lambda/4$. Multiple reflections of light take place inside the cavity. Moreover, in order to adjust the cavity thickness at the desired wavelength, a wedged structure is constructed. The highest spatial resolution is obtained when the superconducting film is evaporated directly onto the MOL. This is because the smaller the distance between the MOL and the sample is, the better the magnetic imaging becomes since there is little stray magnetic field effect.

In addition to these ideas already proposed for conventional MOL (EuSe)[103], there is another strong point. Using QWs is also interesting due to low absorption, easy adjustment of the balance between absorption and Faraday rotation by choosing the number of QWs, and the possibility to have a thin active layer (QWs) in a thick MOL in order to keep a good spatial resolution. When a $Cd_{1-x}Mn_xTe$ QW is inserted in an optical cavity the Faraday rotation can be further increased by using a Bragg structure, that is, placing the QWs at antinodes of the electric field in the optical cavity.

In order to make an optical cavity, Al or the superconductor itself if it is a good reflector, should be evaporated on top of the cap layer as a back mirror. In order to obtain the largest Faraday rotation, a minimum of the reflectivity spectrum has to be matched with the QWs transition. This is the resonance condition. However, the reflectivity, which decreases at the QW transition when the resonance condition is fulfilled, has to be kept to a reasonable level compatible with a good signal-to-noise ratio. Therefore an optimum number of QWs has to be found in multi-quantum well structures. The Mn composition

of the QWs also has to be optimized. It governs not only the Zeeman splitting of the excitonic transition but also the linewidth.

The time decay of the magnetization of the Mn ions in SMSC is known to be fast, in the sub-nanosecond range, since it is governed by spin-spin relaxation rather than by spin-lattice relaxation[105][106]. This opens the way for time-resolved imaging studies with good temporal resolution, e.g. the study of the dynamics of flux penetration.

On the other hand, there are also problems at the fabrication. It is troublesome to remove GaAs substrate by chemical etching with keeping fragile layers. Furthermore, the chemical etching solution strongly reacts with some metals e.g. lead.

## 10.3 Sample preparation and characterization

### 10.3.1 Lead with europium sulfide magneto-optic layers

Since lead is very reactive with the chemical etching solution used to remove the GaAs substrate from the SMSC sample, we tried to use EuS as a MOL. The sample is shown in Fig. 10.2.

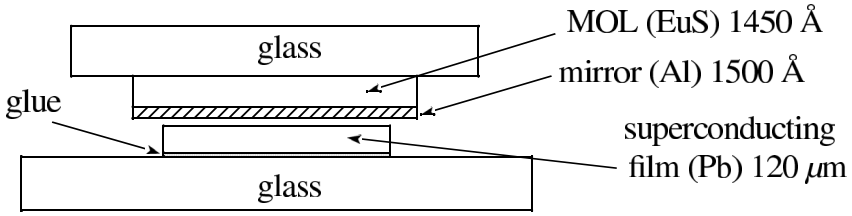


Figure 10.2: Schematic drawing of Pb with EuS sample. The thickness of EuS, Al, and Pb are 1450 Å, 1500 Å, and 120 $\mu$m, respectively. EuS is fabricated by Joule-effect evaporation. The EuS MOL is fixed on the Pb by pressing all night.

The thickness of EuS MOL fabricated by Joule-effect evaporation on a 0.4 mm glass substrate is 1450 $\pm$ 150 Å hence it is thin enough for good spatial resolution. A 1500 Å thick Al layer is evaporated on the EuS MOL as a mirror in order to get high reflectivity. The EuS MOL is pressed on Pb with a weight and left one night. Lead is purchased from Goodfellow Company in sheets of controlled thickness.

A typical reflectivity spectrum and Faraday angle curve of EuS MOL used for our experiment are displayed in Fig. 10.3.

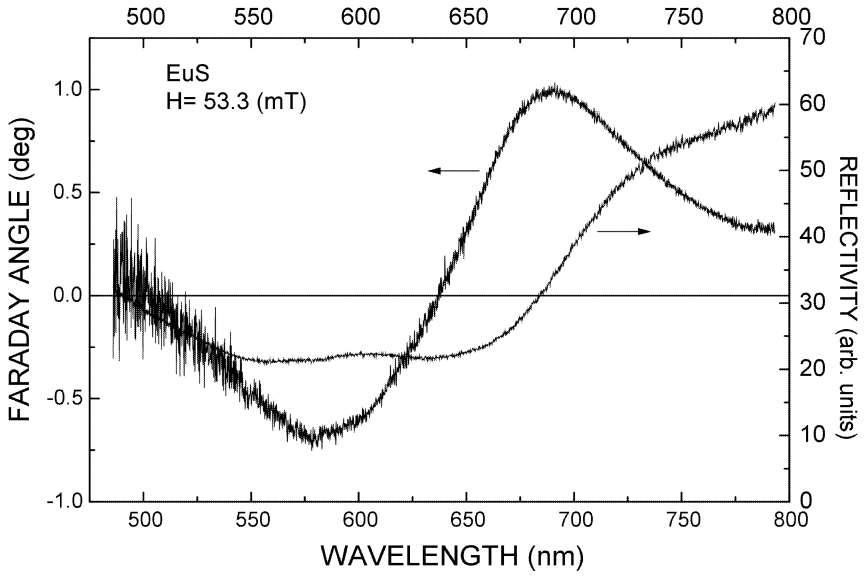


Figure 10.3: Right scale: light reflection spectrum for zero applied magnetic field $H$=0 mT at $T$=2 K. Left scale: Faraday rotation-angle spectrum for $H$=53.3 mT.

For our experiment we use a tungsten-halogen lamp and an interference filter at 700 nm to get good reflected light and large Faraday rotation angle from the sample. Indeed EuS MOL may be expected to disturb the flux pattern, but no self-domain could be observed in our EuS sample, consequently it is usable for the Faraday microscopy. Using microprobe analysis we found a layer content of oxygen in EuS. The layer probably consists of a mixture of EuS and EuO. This may explain why we did not observe magnetic domains in the MOL.

### 10.3.2 Indium with quantum well magneto-optic layers

The sample consists of an indium layer as superconducting materials and a $Cd_{1-x}Mn_xTe$/ $Cd_{1-y}Mg_yTe$ heterostructure as MOL. The structure is sketched in Fig. 10.4[98].

The semiconductor heterostructure was grown by molecular beam epitaxy at the Institute of Physics in Warsaw. The $Cd_{0.85}Mg_{0.15}Te$ buffer was deposited on (001) GaAs

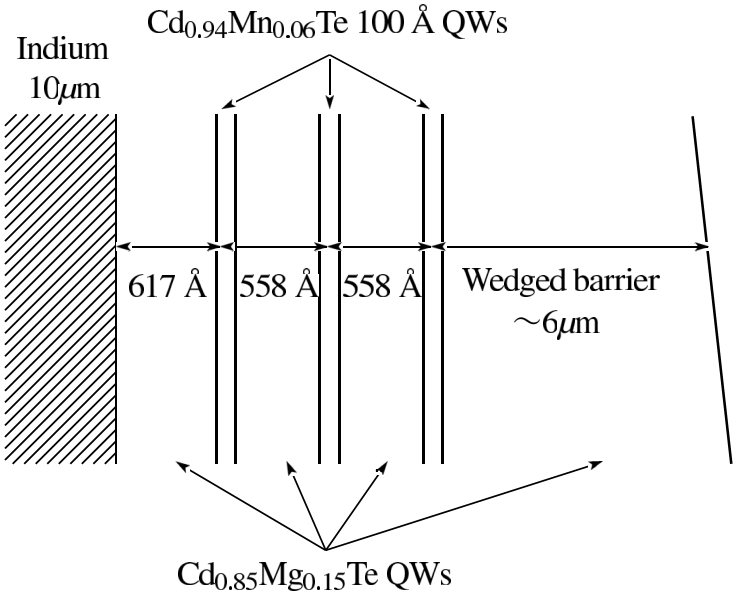


Figure 10.4: Schematic representation of the sample composition (not to scale) after the etching of the GaAs substrate.

substrate without rotation of the sample holder resulting in a slight gradient of both the thickness of the buffer and its refractive index. The buffer was followed by three 100 Å $Cd_{0.94}Mn_{0.06}Te$ QWs separated by $Cd_{0.85}Mg_{0.15}Te$ barriers 558 Å thick. A 10 $\mu$m thick indium layer was then evaporated directly on top of the 617 Å $Cd_{0.85}Mg_{0.15}Te$ cap layer. The MOL is designed as an optical cavity and indium serves both as superconducting layer and cavity back mirror. The first and third QWs are nearly located at antinodes of the electric field in the cavity in order to enhance Faraday rotation. The indium-covered side was glued on a glass plate and the GaAs substrate was removed by mechanical thinning and selective chemical etching. For the Faraday microscopy the spatial resolution was checked to be 1 $\mu$m, magnetic resolution 10 mT, the range of temperature for use should be up to 20 K.

A typical reflectivity spectrum and Faraday angle curve are displayed in Fig. 10.5. The reflectivity spectrum presents an interference pattern associated to the metal/semiconductor/vacuum optical cavity. This pattern shows a spectral shift when the illuminating spot is scanned along the sample surface, according to the thickness variation of the cavity. The maximum Faraday angle is observed when a minimum of reflectivity is matched with the QW transition energy (the cavity resonance condition). The peak Faraday angle

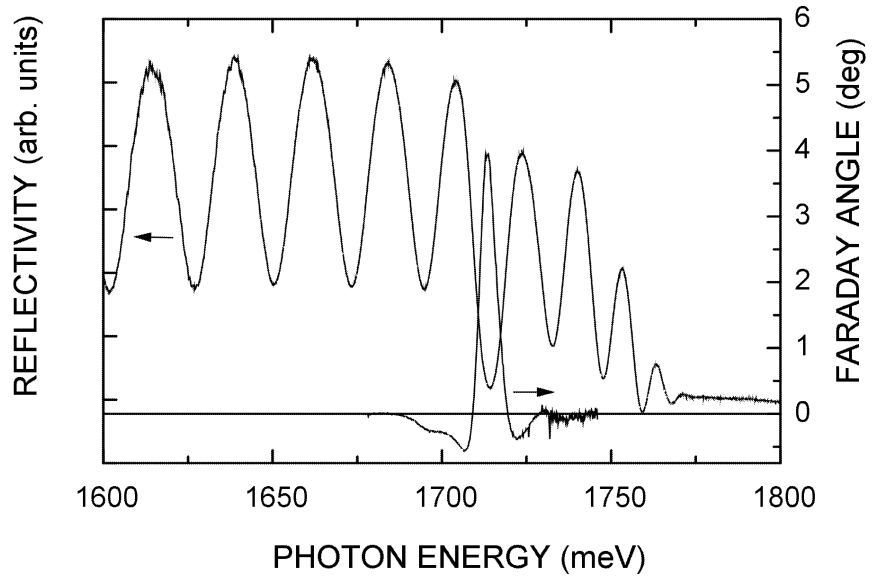


Figure 10.5: Left scale: light reflection spectrum for zero applied magnetic field $H$ = 0 mT at $T$=2 K. Right scale: Faraday rotation-angle spectrum for $H$=56 mT.

was found to vary linearly with the applied magnetic field $H$. The measured slope equals to 54.4 deg $T^{-1}$ at the QWs (e1-hh1) exciton transition.

## 10.4 Experimental set-up

Magneto-optical imaging is performed using pumped liquid helium immersion-type cryostat equipped with a microscope objective. This objective with the numerical aperture 0.4 is placed in the vacuum part of the cryostat and can be controlled from outside. The samples are studied in a magnetic field applied from exterior coils. The optical setup is similar to a reflection polarizing microscope as shown in Fig. 10.6. Before measuring the samples are zero magnetic field cooled down to 1.8 K. The indium-with-QWs sample is illuminated with linearly polarized light from a Ti-Sapphire laser, through a rotating diffuser to remove laser speckle. In case of lead-with-EuS sample a tungsten lamp with an interference filter is used as a light source. Reflected light from the sample passes through a crossed or slightly uncrossed analyzer and is focused onto the CCD camera. The spatial resolution of 1 $\mu$m is limited by the numerical aperture of the microscope objective.

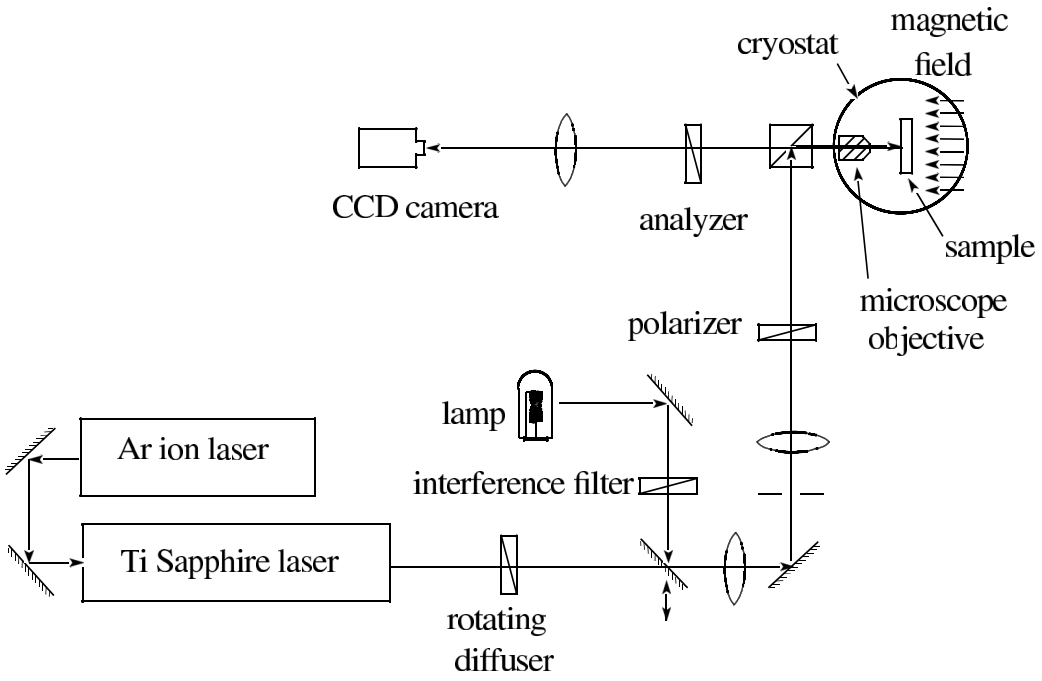


Figure 10.6: Experimental setup for Faraday imaging technique.

# Chapter 11

# Results and discussions

## 11.1 Magnetic flux pattern in indium: general features

In this section we show the typical evolution of intermediate flux patterns as a function of magnetic field in superconducting thin film using Faraday imaging technique. Fig. 11.1 shows an intermediate state structure at the surface of the indium superconducting layer obtained at $T$=1.9 K for various magnetic field values from 0.5 to 15.0 mT. From Eq. (7.1) the critical magnetic field of indium at 1.9 K is 19.4 mT.

Black and gray areas are normal and superconducting state, respectively. The intricate flux pattern results from the competition between long-range repulsive magnetic interactions between normal zones and short-range interactions due to the positive interfacial energy between normal and superconducting areas.

The raw images have to be processed in order to correct the intensity fluctuations of the reflected light due to thickness fluctuations of the MOL and of the sensitivity of CCD detector. In order to obtain an intensity level proportional to the Faraday angle the gray level of each pixel should be calculated as

$$I' = \frac{I_H^\alpha - I_{H=0}^\alpha}{I_{H=0}^\alpha - I_{H=0}^{\alpha=0}} \approx \frac{2}{\alpha}\theta, \tag{11.1}$$

where $I_H^\alpha$ is the raw gray level obtained for an applied magnetic field $H$ and an analyzer angle $\alpha$ and $\theta$ is the Faraday angle. However actually the intensity level of each pixel is calculated as

$$I' = \frac{I_H^\alpha}{I_{H=0}^\alpha}. \tag{11.2}$$

This procedure is faster and sufficient to enhance the contrast and facilitate the analysis of the magnetic flux pattern spacing and of the area of normal zones. As it can be seen in Fig. 11.1, the normal state areas (black level) are separated by superconducting regions (gray

level) in the intermediate state. At low applied magnetic field, first, several flux tubes (dark spots) appear (a) and the intermediate state patterns transform from normal state flux tubes to long lamellae (dark corrugated stripes) (b). This transformation continues (c) - (f) until when the lamellae become almost dominant (g). Then the intermediate state patterns is composed of dense lamellae, namely, labyrinthian pattern. With larger applied magnetic field the width of lamellae gradually increases (h) - (j), and then the normal state prevails over the superconducting state. Additionally, with increasing magnetic field the lamella width and length of superconducting state decreases and the superconducting spots can be observed (k) - (n).

At low applied magnetic field, typically smaller than one third of the critical magnetic field, we observe the coexistence of a disordered array of flux tubes and a lamella-like quasi-periodic pattern. Indeed the free energy of the flux tube periodic array and of the periodic lamella pattern are known to be very close[102]. When the magnetic field increases the lamella pattern becomes dominant over the tube pattern. The white regions observed in images (a) - (j) correspond to places where the magnetic flux was trapped in the reference image at $H = 0$. Once the magnetic flux is trapped inside the sample due to impurities and defects it stays even when the magnetic field is decreased to zero. Especially at low magnetic field we can follow the movement of flux tubes by comparing the position of black and white spots (a) - (c). As shown at the right-hand side of the images in (a), (b), there is no magnetic flux in the $\sim$50 $\mu$m wide region from the right edge of the sample, which is called 'diamagnetic band'. The diamagnetic band exists in applied magnetic field up to 2 - 5 mT and is associated with a geometrical metastable barrier[107]. In this magnetic field range, the flux tubes penetrate irreversibly into the sample[108]. This band disappears with further increase of the applied magnetic field. Therefore the flux can reversibly enter from the edges, and the lamella shape of the flux becomes dominant. The transition from tube to lamella pattern was reported for other systems: fractional monolayer covering of Pb on Cu[109], $Fe_3O_4$ kerosene-based ferrofluids[110], and it was predicted by theoretical calculations[94]. As can be seen in (k) - (n) the evolution of superconducting state pattern is different from that of normal state pattern. The width of superconducting lamellae slightly decreases from 8 $\mu$m at $h = 0.4$ to 3.5 $\mu$m at $h = 0.8$. Moreover, the superconducting ring can be found while the ring of normal state does not exist. Among these interesting results of indium thin film, we study the behavior of the flux tubes with applied magnetic field in detail in Sec. 11.4.

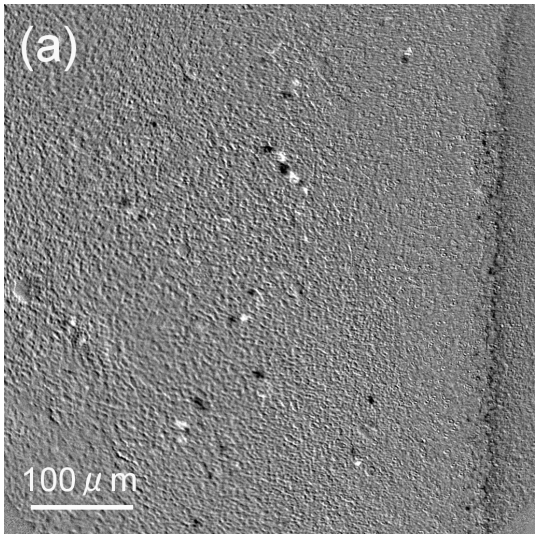


$h = H_a/H_c = 0.026$

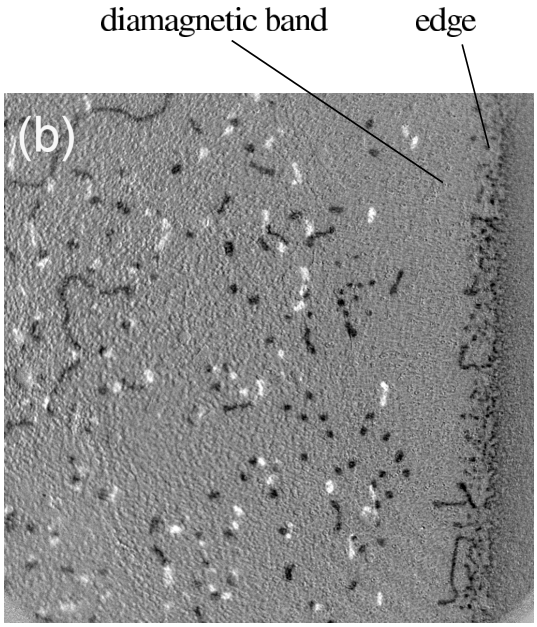


$h = H_a/H_c = 0.057$

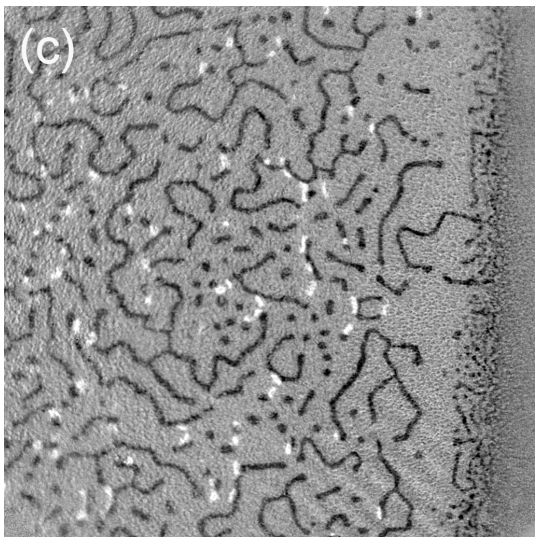


$h = H_a/H_c = 0.129$

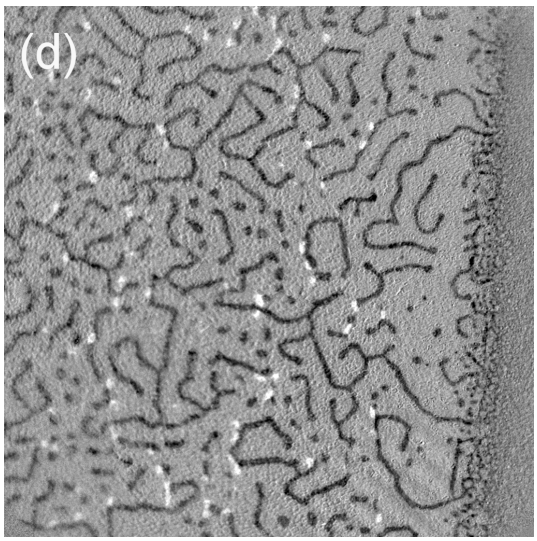


$h = H_a/H_c = 0.155$

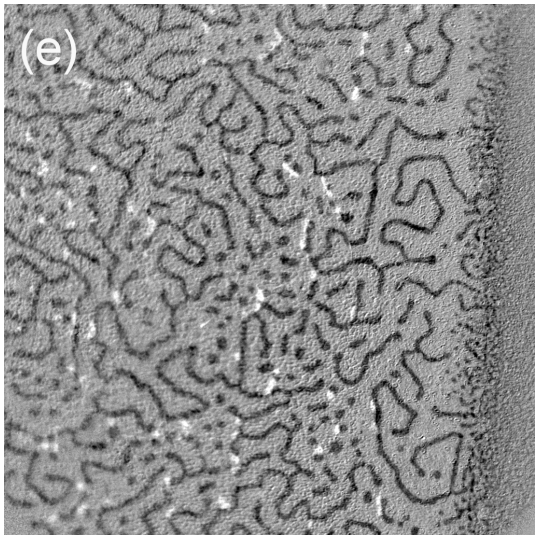


$h = H_a/H_c = 0.186$

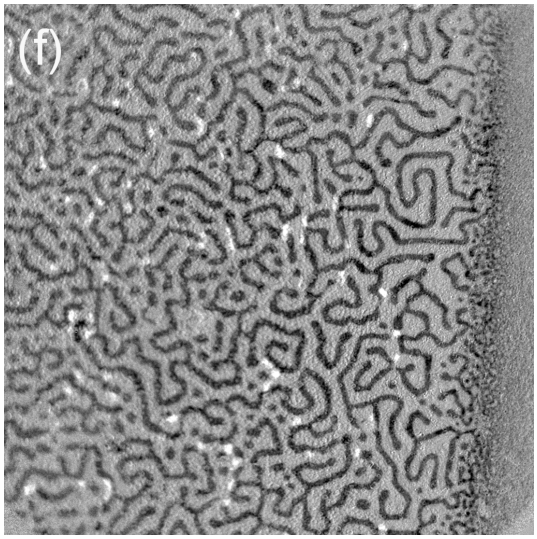


$h = H_a/H_c = 0.284$

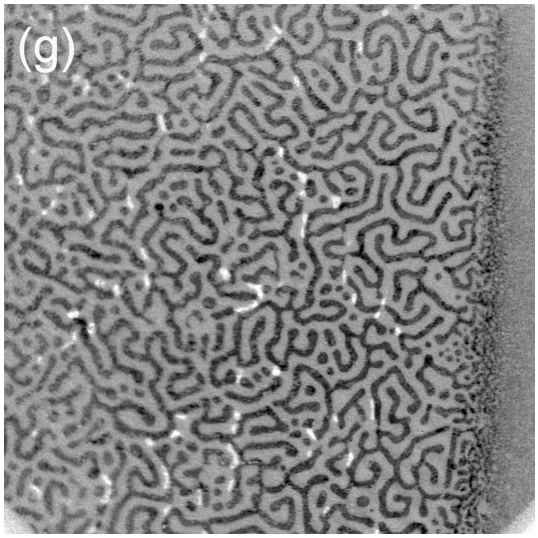


$h = H_a/H_c = 0.325$

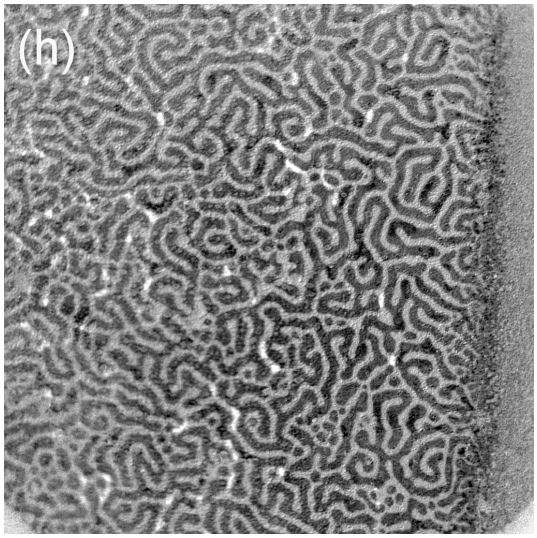


$h = H_a/H_c = 0.469$

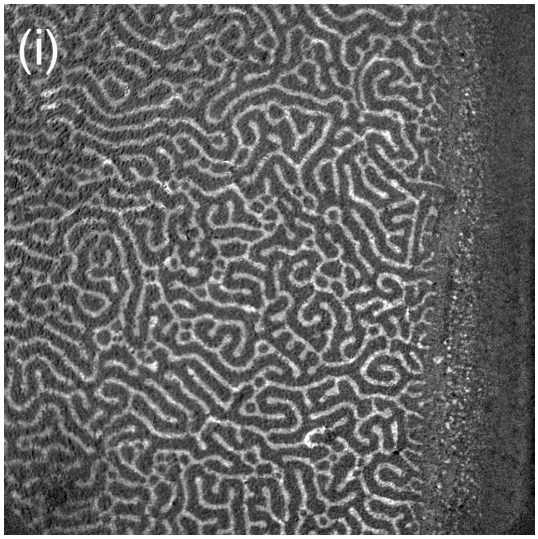


$h = H_a/H_c = 0.536$

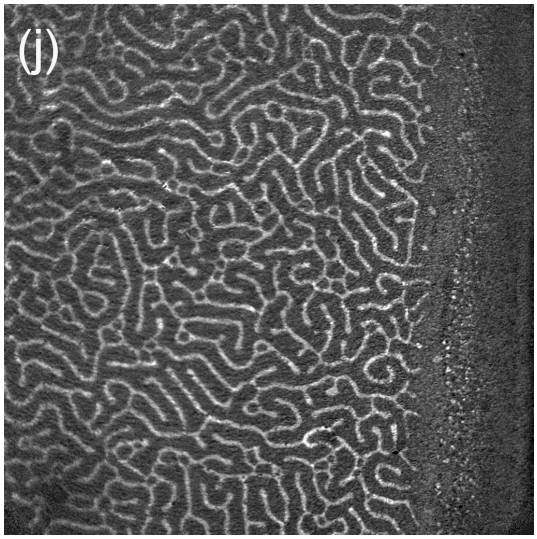


$h = H_a/H_c = 0.608$

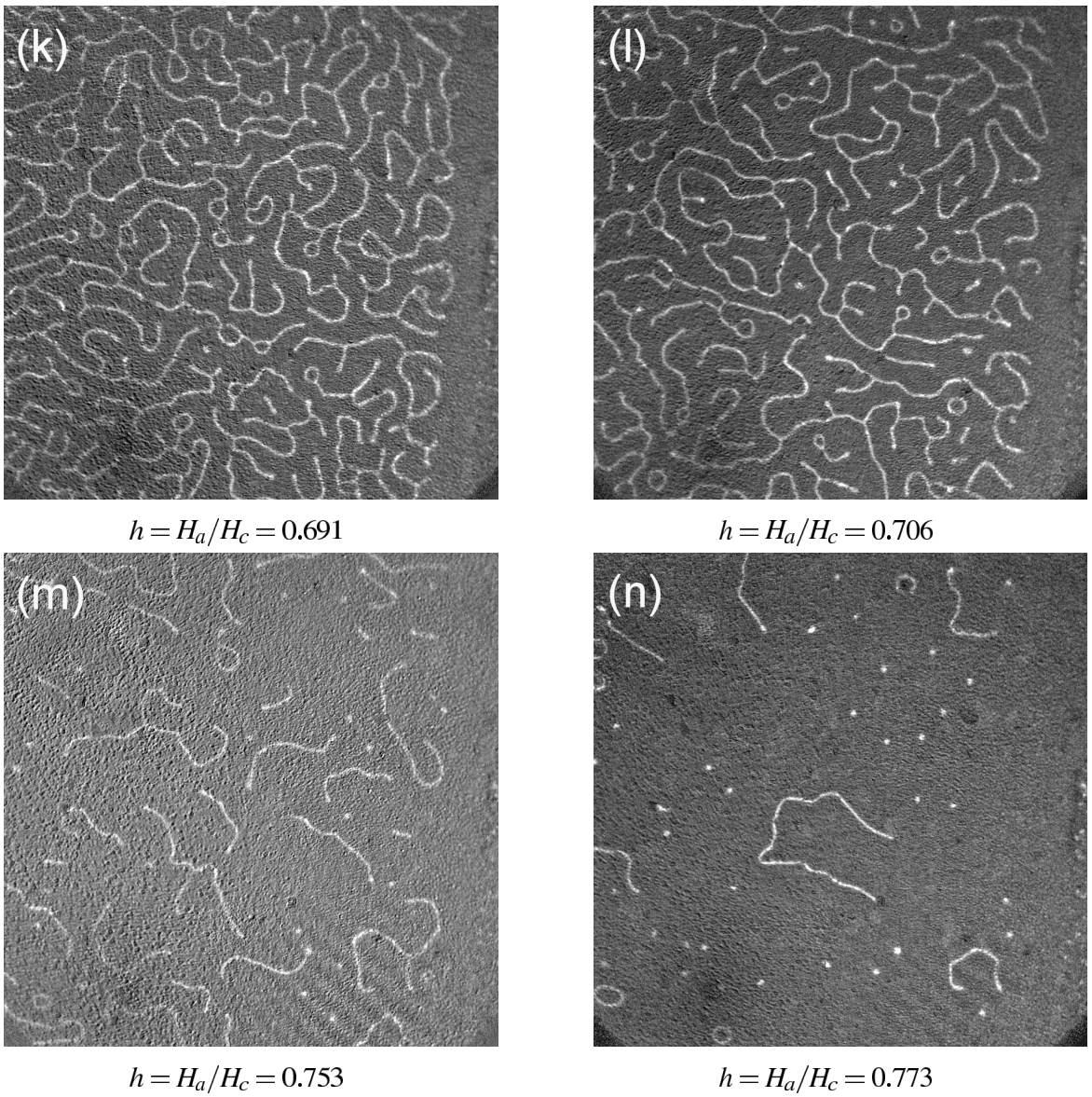


Figure 11.1: The images of the magnetic flux patterns at the surface of 10 $\mu$m thick superconducting In film revealed with the $Cd_{1-x}Mn_xTe$ QWs structure as magneto-optical layer in applied magnetic field (a)0.5 mT ($h = 0.026$), (b)1.1 mT ($h = 0.057$), (c)2.5 mT ($h = 0.129$), (d)3.0 mT ($h = 0.155$), (e)3.6 mT ($h = 0.186$), (f)5.5 mT ($h = 0.284$), (g)6.3 mT ($h = 0.325$), (h)9.1 mT ($h = 0.469$), (i)10.4 mT ($h = 0.536$), (j)11.8 mT ($h = 0.608$), (k)13.4 mT ($h = 0.691$), (l)13.7 mT ($h = 0.706$), (m)14.6 mT ($h = 0.753$), and (n)15.0 mT ($h = 0.773$). Normal and superconducting domains appear in black and gray, respectively. The edge of the indium film can be seen on the right-hand side of images where the flux pattern disappears. The image size is 527 $\mu$m $\times$ 527 $\mu$m. The analyzer was uncrossed by $\alpha = 20^\circ$ with respect to the polarizer. The temperature is $T$=1.9 K. For images (k) - (n) the reference image was taken at high magnetic field with the sample in the normal state.

## 11.2 Magnetic flux pattern in lead

Fig. 11.2 shows the images of the magnetic flux pattern evolution at the surface of a 120 $\mu$m thick superconducting lead film for magnetic field values from 16 mT to 56 mT. The temperature is 2 K, that is, much lower than the critical temperature of lead (7.18 K). The critical magnetic field of lead at 2 K is $H_c$(2 K)=74.1 mT.

In the same way as for the indium sample raw images were processed in order to eliminate intensity fluctuations of the reflected light due to thickness inhomogeneities of the MOL and sensitivity of CCD detector. The quality of the image is further improved by Fourier transform filtering. Actually the magnetic contrast observed in the images of Fig. 11.2 is not very good. This is most probably due to the poor quality of the EuS layer that contains a lot of oxygen. Moreover the lead sample is pressed onto the MOL, not evaporated onto the MOL as for indium. The contact between lead and the MOL may not be as good as for an evaporated metallic sample.

As it can been seen in Fig. 11.2, at low magnetic field, we observed circular domains bearing magnetic flux, that is, flux tubes. With increasing magnetic field, the magnetic flux shape gradually transforms from tubes to lamellae structures. At low magnetic field, the flux tubes are arranged in a disordered array that becomes regularly ordered as the magnetic field increases (a), (b). When the applied magnetic field reaches 24 mT, the flux lamella pattern begins to appear in one direction. Applying larger magnetic fields, the lamellae grow in all directions while connecting each flux tube.

In the following we shall study the magnetic field dependence of the size of these structures and we shall compare the results to the theoretical calculations.

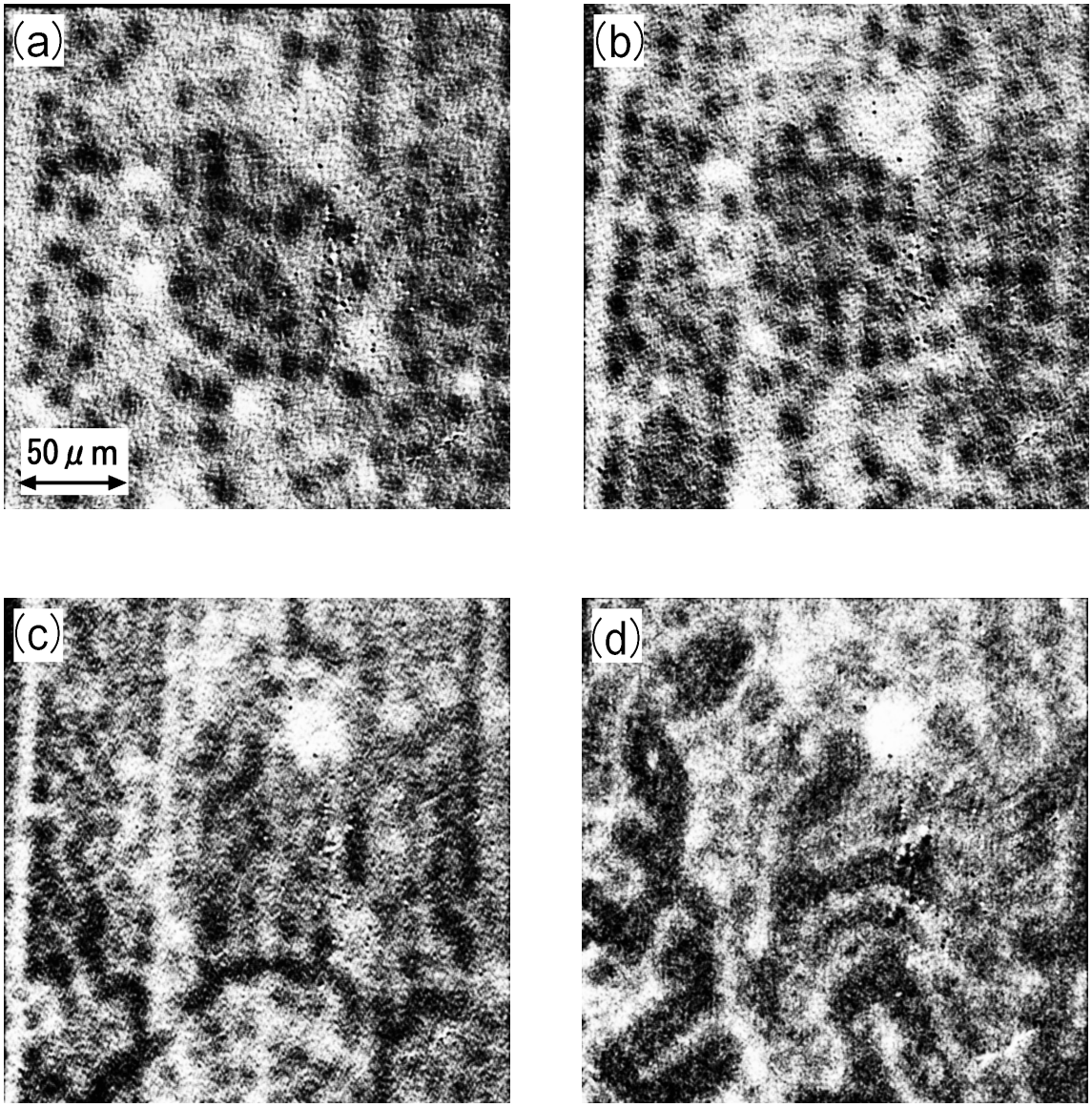


Figure 11.2: The images of the magnetic flux patterns at the surface of 120 $\mu$m thick superconducting Pb film revealed with the EuS magneto-optical layer in applied magnetic field (a)16 mT ($h = 0.216$), (b)20 mT ($h = 0.270$), (c)28 mT ($h = 0.378$), and (d)56 mT ($h = 0.756$). Normal and superconducting domains appear in black and gray, respectively. The image size is 233 $\mu$m$\times$ 233 $\mu$m. The temperature is $T = 2$ K.

## 11.3 Theory

As shown in the previous section, a flux tube-to-lamella transition can be observed. Therefore it is useful to compare the free energy of flux tube lattice and lamella lattice and to determine the parameters that govern the flux tube-to-lamella transition. Furthermore, for a quantitative analysis of the experimental data it is needed to calculate the tubes and lamellae size and period as a function of the magnetic field and material parameters.

We first review the theory for flux lamella structure. Then, we consider flux tube lattice and isolated flux tube since the theoretical studies for them were not well developed until now. This enables us to compare the flux tubes and lamellae behavior as a function of adjustable parameters.

Here we mention the essential parameters. The reduced magnetic field $h \equiv H_a/H_c$, where $H_a$ is the applied magnetic field and $H_c$ is the critical magnetic field of the superconductors, is important as the externally adjustable parameter. It governs the ratio of normal area over superconducting one in the intermediate state. As the parameter indicating the thickness and the nature of the sample, the magnetic Bond number $N_B = d/\pi\Delta$, where $d$ is thickness of the sample and $\Delta$ ($\propto \xi - \lambda$) is the width of the interfaces between normal and superconducting regions, is also important. The Bond number represents the magnitude of the magnetic energy compared to interface energy.

### 11.3.1 Flux lamella lattice in the Current Loop model

In this section we briefly review the theory for flux lamella pattern in order to consider the difference of behavior between flux tube and flux lamella. The flux lamella structure in the intermediate state of thin type-I superconductors has been analyzed in detail by using the Current Loop model[95].

We assume that the number of straight normal regions, bounded by superconducting-normal interfaces, is $i$ with perimeter $L_i$ and width $w_n$. The intermediate state is occupied with normal regions with volume $V_n = dw_n \sum_i L_i$ and superconducting regions with volume $V - V_n$ ,where $V$ is the total volume. The total free energy is $E = E_c + E_{int} + E_m$, where $E_c$, $E_{int}$, and $E_m$ are the condensation energy, the interfacial energy, and the magnetic energy, respectively. $E_c$ and $E_{int}$ are written in Eq. (9.19) and $E_m$ is expressed as[95]

$$
\begin{aligned}
E_m &= \frac{H_a^2}{8\pi}V + \frac{H_n H_a}{4\pi}(1-\rho_n)V \\
&\qquad -\frac{wM^2}{\pi^2}V\sum_{n=1}^{\infty}\frac{[1-\cos(2\pi n w_n/w)]}{n^3}\times\left(\frac{2\pi n}{w}+\frac{e^{-2\pi dn/w}-1}{d}\right) \\
&= \frac{H_a^2}{8\pi}V + \frac{H_n^2}{8\pi}\rho_n(1-\rho_n)V - \frac{wM^2}{\pi^2}V\sum_{n=1}^{\infty}\frac{[1-\cos(2\pi n w_n/w)]\times(e^{-2\pi dn/w}-1)}{n^3 d},
\end{aligned}
\tag{11.3}
$$

where $w$, $d$, $\rho_n$, and $M$ are the period of the lamella structure, the thickness of the sample, the area fraction of the normal phase, and the magnetization $M = -H_n/4\pi \simeq -H_c/4\pi$, respectively. The first term of $E_m$ is the bulk magnetic energy and second is due to the self- and mutual interaction. By minimizing the $E_{int} + E_m$ with respect to $\rho_n$ and the reduced period $w/d$ we can determine the magnetic field value of the normal regions, the equilibrium period, and width of lamella structure with various magnetic field. In next sections and Sec. 11.4.3 we consider the flux tubes and the difference of behavior between flux lamellae and flux tubes, respectively.

### 11.3.2 Flux tube lattice in the Current Loop model

In this section, I calculate the size and spacing of the magnetic flux tubes by using the Current Loop model. We consider disk-like flux tubes with radius $R$ arranged in a triangular lattice with lattice constant $a$ as shown in Fig 11.3.

As explained in section 9.3, the total free energy of normal region is $E = E_c + E_{int} + E_m$, where $E_c$, $E_{int}$, $E_m$ are the condensation energy, the interfacial energy, and the magnetic energy, respectively. In the following we shall denote by $E_c$, $E_{int}$, $E_m$, energies per unit area. Taking zero for the energy of the superconducting state, the condensation energy (loss of condensation energy in normal zones) is expressed as:

$$
E_c = \frac{V}{S}\frac{H_c^2}{8\pi}\rho_n = N_A N_B \frac{\sqrt{3}}{2}a^2 d\frac{H_a H_c}{8\pi}\Bigg/\left(N_A N_B\frac{\sqrt{3}}{2}a^2\right) = d\frac{H_a H_c}{8\pi}, \tag{11.4}
$$

where $N_A$ and $N_B$ are the total number of unit cells in the $x$ and $y$ directions, respectively, $\rho_n = H_a/H_c$ is the fraction of the surface area in the normal state, $H_a$ being the applied magnetic field. The volume is $V = N_A N_B d(\sqrt{3}a^2/2)$ where $d$ is the thickness of the sample.

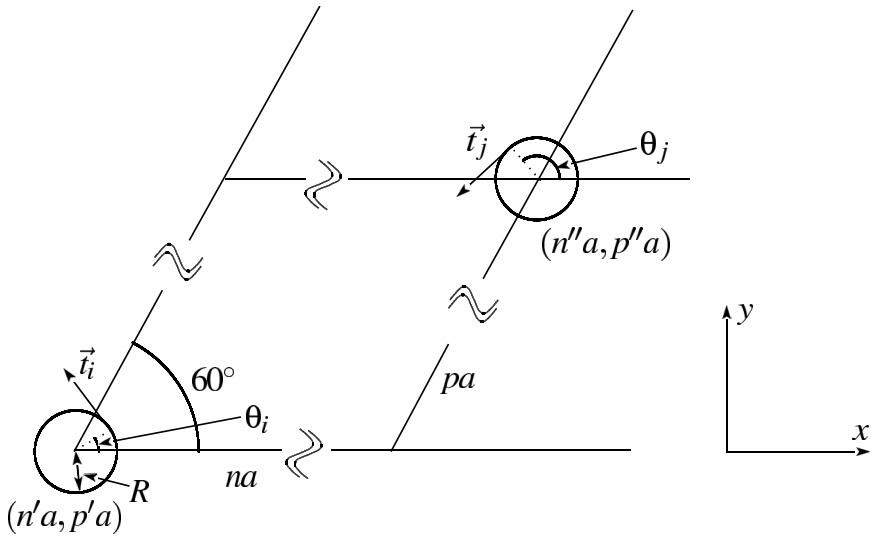


Figure 11.3: Triangular array of circular normal tubes. The unit tangent vector of current flow is expressed as $\vec{t}_i, \vec{t}_j$.

The interfacial energy per unit area is

$$E_{int} = \frac{H_c^2}{8\pi}\Delta d(2\pi R)N_A N_B \Big/ \left(N_A N_B \frac{\sqrt{3}}{2}a^2\right) = \frac{\Delta d R H_c^2}{2\sqrt{3}a^2}. \tag{11.5}$$

Then we compute the magnetic energy as a sum of two contributions. The first is the bulk magnetic energy. The second is the self- and mutual induction term of those tubes (see Sec. 9.3). We calculate the first contribution (see appendix B.1),

$$E_{m1} = \frac{V}{S}\frac{H_a^2}{8\pi} + \frac{V}{S}\frac{H_a H_c}{4\pi}(1-\rho_n) = d\frac{H_a^2}{8\pi} + d\frac{H_a H_c}{4\pi}(1-\rho_n). \tag{11.6}$$

The first term is the energy of the external magnetic field in the absence of the sample, and the second one is the interaction between the magnetization $M$ in the superconducting zones with the external magnetic field. We calculate the self- and mutual induction term as (see Sec. 9.3):

$$E_{m2} = -\frac{M^2}{2}\sum_i\sum_j \int_0^d dz_i \int_0^d dz_j \oint ds_i \oint ds_j \frac{\vec{t}_i \cdot \vec{t}_j}{R_{ij}}, \tag{11.7}$$

where $M = -H_n/4\pi \simeq -H_c/4\pi$ is the magnetization (see appendix B.2). The result is:

$$\begin{aligned} E_{m2} &= -2\pi d M^2 \rho_n(1-\rho_n) \\ &\quad + 2\frac{\pi R^2}{a^2} M^2 d \sum_{m=-\infty}^{\infty}{}' \sum_{t=-\infty}^{\infty}{}' \frac{J_1^2(4\pi d\sqrt{m^2+t^2-mt}/\sqrt{3}a)}{m^2+t^2-mt} \\ &\quad \times \frac{1-\exp(-4\pi d\sqrt{m^2+t^2-mt}/\sqrt{3}a)}{4\pi d\sqrt{m^2+t^2-mt}/\sqrt{3}a}. \end{aligned} \tag{11.8}$$

the prime indicates that the summation is taken all integers except $m = t = 0$. $J_1$ denotes the Bessel function of the first kind. $E_{m2}$ appears as a summation over all lattice vectors in the reciprocal space, each vector being defined as

$$\vec{k}_{m,t} = \frac{2\pi}{a} \begin{pmatrix} m \\ \frac{2t-m}{\sqrt{3}} \end{pmatrix}. \tag{11.9}$$

Note that $E_{m2}$ depends only on the modulus of the $\vec{k}_{m,t}$ vectors. The first term of $E_{m2}$ is a bulk term and second is a surface term depending on the ratios $a/d$ and $R/d$. This surface term becomes quantitatively important only when the thickness of the sample is comparable to the radius or the period of the flux tube lattice. This can be understood by considering the analogy with a collection of electrical circuits consisting of solenoids of finite length arranged in a periodic lattice. When the length of these solenoids becomes comparable to their radius or to the period of the lattice, the part of the magnetic energy related to the stray magnetic field becomes important.

The dependence of the total energy on the reduced magnetic field $h(=H_a/H_c)$ is shown in Fig. 11.4.

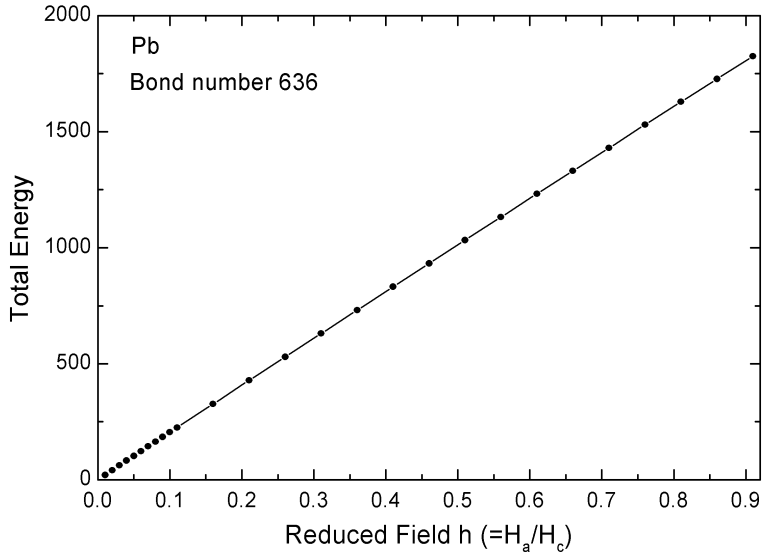


Figure 11.4: The total energy as a function of the reduced magnetic field.

The total energy is almost linear because the bulk term of free energy is proportional to $h$ and the 'surface' energy ($E_{int}$, second term of $E_{m2}$) is quantitatively small. But

qualitatively it is very important because this 'surface' energy is determined solely by the locations of the superconducting-normal interfaces. It follows that minimizing this energy enables to determine the domain structure, i.e. period and size.

It is convenient to use an energy per unit area expressed in units of $2\sigma_{SN}$: $\tilde{E}_{unit} = E_{unit}/2\sigma_{SN}$, where $\sigma_{SN} = H_c^2\Delta/8\pi$ is the interfacial tension, then

$$\tilde{E}_c = \frac{\pi}{2}N_B h \quad , \quad \tilde{E}_{int} = \frac{\sqrt{2\pi h}}{\sqrt{3}}\frac{1}{x}, \tag{11.10}$$

$$\tilde{E}_{m1} = \frac{\pi}{2}N_B h^2 + \pi N_B h(1-h), \tag{11.11}$$

$$\begin{aligned}\tilde{E}_{m2} &= -\frac{\pi}{2}N_B h(1-h) \\ &\quad + \frac{\sqrt{3}}{4}hN_B \sum_{m=-\infty}^{\infty}{}' \sum_{t=-\infty}^{\infty}{}' \frac{J_1^2(2\sqrt{2\pi h}\sqrt{m^2+t^2-mt}/\sqrt{3})}{m^2+t^2-mt} \\ &\quad \times \frac{1-\exp(-4\pi\sqrt{m^2+t^2-mt}/(\sqrt{3}x))}{4\pi\sqrt{m^2+t^2-mt}/(\sqrt{3}x)},\end{aligned} \tag{11.12}$$

where $N_B = 2M^2 d/\sigma_{SN} = d/\pi\Delta$ is the dimensionless magnetic Bond number associated with the nature of material and its size, $h = \rho_n = \pi R^2/(\sqrt{3}a^2/2) = H_a/H_c$ is the reduced magnetic field, and $x = a/d$.

In Fig. 11.5 we plot the sum of interfacial energy ($\tilde{E}_{int}$) and magnetic energy ($\tilde{E}_{m2}$) as a function of the reduced period $a/d$ for various reduced magnetic fields.

The bulk term of $\tilde{E}_{m2}$ only contributes as a constant energy term. Therefore this plot represents also the 'surface' energy but shifted on the energy scale. The minimum of each curve defines an equilibrium period $a/d$ which depends on the reduced magnetic field $h$ and the Bond number $N_B$. Fig. 11.6 and Fig. 11.7 show the reduced period and reduced diameter as a function of the applied magnetic field for various Bond numbers.

The diameter is related to the period by flux conservation, that is : $h = 2\pi R^2/\sqrt{3}a^2$. At low magnetic field, flux tubes are small and well separated. The period varies as $1/\sqrt{h}$. Therefore the flux tube diameter tends to a constant value. At large magnetic field the diameter increases up to the value of the period, that is, the limit of the close-packed lattice. In order to go beyond this limit, hexagonal flux tubes should be considered.

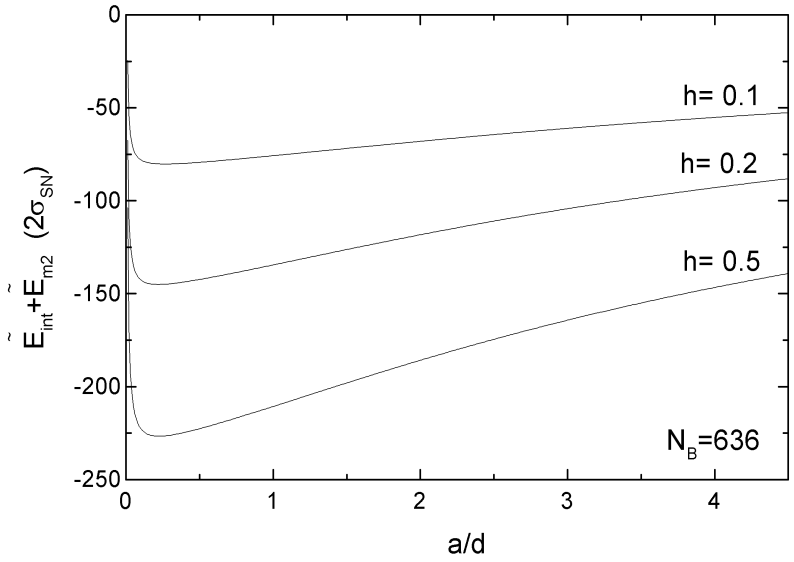


Figure 11.5: Sum of interfacial energy ($\tilde{E}_{int}$) and magnetic energy ($\tilde{E}_{m2}$) as a function of the reduced period $a/d$.

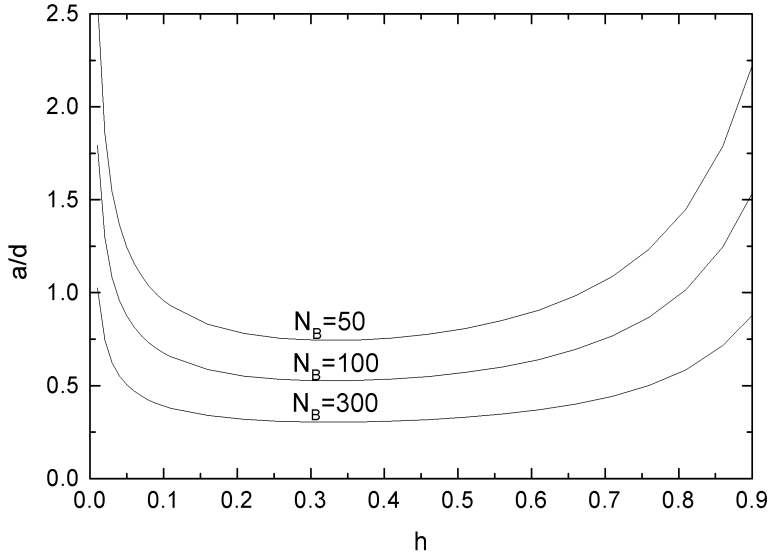


Figure 11.6: Reduced period $a/d$ as a function of the reduced magnetic field $h$.

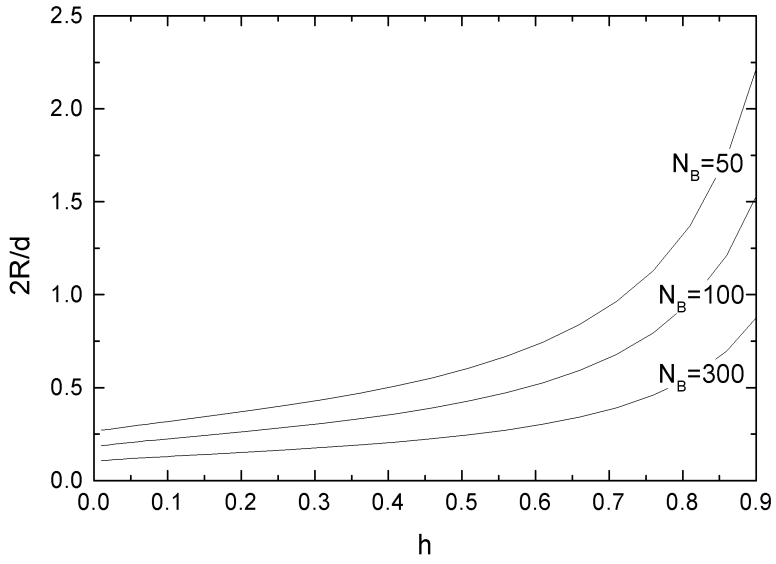


Figure 11.7: Reduced diameter $2R/d$ as a function of the reduced magnetic field $h$.

### 11.3.3 Isolated flux tube in the Current Loop model

Experimental data very often show a disordered flux tube array. At very low magnetic field we observe isolated flux tubes in the image frame. Therefore, it is interesting to understand what determines the diameter of a flux tube. It is valuable to compare the contribution of the self-induction part of the magnetic energy with that of the mutual induction part. In order to understand this point we calculate the interfacial and magnetic energy of an isolated flux tube.

The magnetic energy is[93]:

$$E_{mag} = \frac{16\pi}{3} M^2 R^3 f(k), \tag{11.13}$$

where $M$ is the uniform magnetization, $R$ is the radius of the flux tube (see appendix B.3). $f(k)$ is

$$f(k) = 1 - \frac{1}{k^3}\{(2k^2-1)E(k) + (1-k^2)K(k)\}, \tag{11.14}$$

where $E(k)$ and $K(k)$ are complete elliptic integrals of the first and second kind, respectively, and $k^2 = p^2/(1+p^2)$, $p = 2R/d$. The interfacial energy is

$$E_{int} = \sigma_{SN} d 2\pi R. \tag{11.15}$$

Then we get the energy in units of $4\sigma_{SN}$ par unit area $\tilde{E}$ :

$$\tilde{E} = \frac{E_{mag} + E_{int}}{4\sigma_{SN} \cdot \pi R^2} = \frac{d}{2R} + \frac{2RN_B}{3d} f(k) = \frac{1}{p} + \frac{1}{3} pN_B f(k), \tag{11.16}$$

where $N_B = 2M^2 d/\sigma_{SN}$ is the magnetic Bond number. Fig. 11.8 shows the dependence of $\tilde{E}$ on $2R/d$ for various magnetic Bond numbers. The minimum of this function defines an

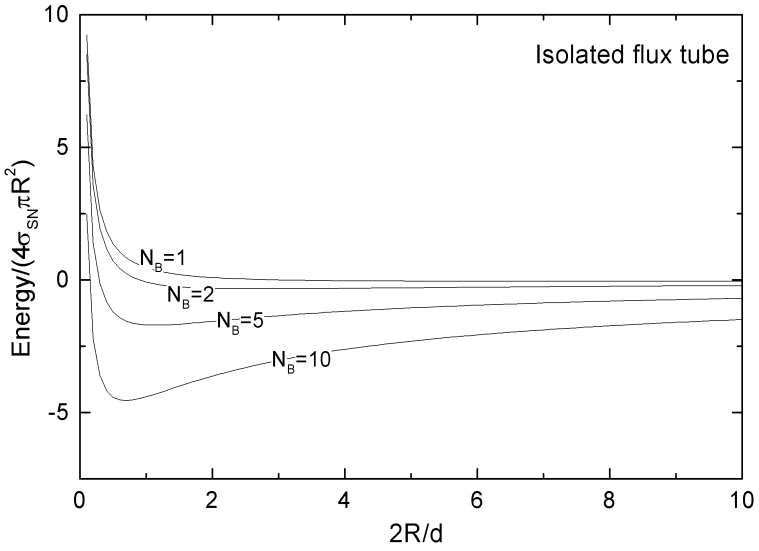


Figure 11.8: The energy in units of $4\sigma_{SN}$ per unit area of isolated flux tube for various magnetic Bond numbers.

equilibrium diameter $2R_{eq}/d$ for various Bond numbers. By minimizing $\tilde{E}$ in Eq. (11.16) with respect to $k$ the relation:

$$N_B = \frac{3(1-k^2)}{k^2} \left\{ 1 + \frac{1}{k^3}[(k^2-2)E(k) + 2(1-k^2)K(k)] \right\}^{-1}, \tag{11.17}$$

can be obtained[111], where $E(k)$, $K(k)$, and $k$ are explained above. The equilibrium diameter is the same as the one calculated for a lattice in the limit of low magnetic field $h \to 0$. This means that, although the magnetic interaction is a long-range interaction, at low magnetic field, the diameter of a flux tube in a lattice is mainly determined by the interfacial tension and the self-induction part of the magnetic energy.

For convenience we plot $2R_{eq}/\Delta$ (=$\pi \times N_B \times (2R_{eq}/d)$) as a function of $d/\Delta$ (=$N_B \times \pi$) in Fig. 11.9. This result can be readily compared with experimental data ($2R_{eq}$) obtained

for a given material ($\Delta$) as a function of the sample thickness ($d$). The dashed line indicates the limit of stability for a circular flux tube submitted to a perturbation that tends to elongate it into a lamella shape. It is expressed as[93]:

$$N_B = \frac{9k(1-k^2)}{k^3+(1-k^2)(8-3k^2)K(k)+(7k^2-8)E(k)}, \tag{11.18}$$

where $K(k)$, $E(k)$, and $k$ are explained above.

As it can be seen in Fig. 11.9, with reducing the sample thickness below a few times $\Delta$ the diameter of the flux tube grows again. However, when the thickness $d$ becomes comparable to the width of the interfaces $\Delta$, we reach the limit of validity of the model. Furthermore, it is known that type-I superconductors change into type-II superconductors in this range of film thickness. One needs to check experimentally whether tubes diameter increases or decreases with decreasing $d/\Delta$ below 10.

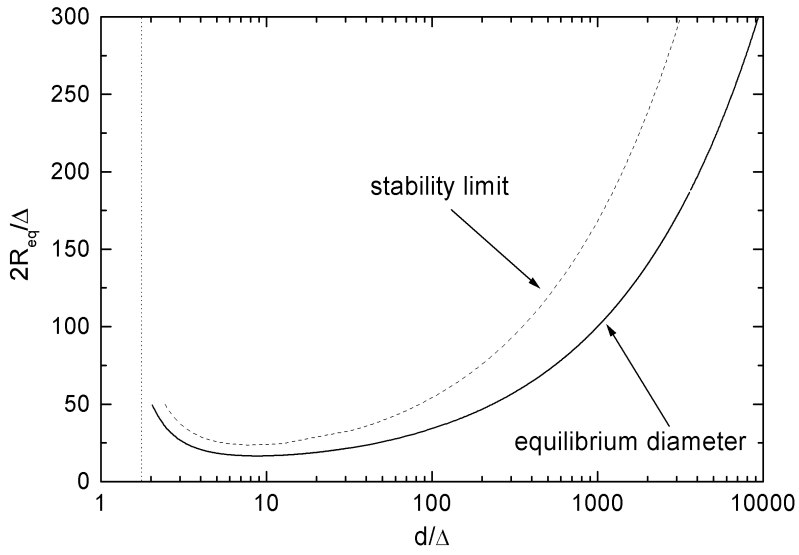


Figure 11.9: The equilibrium tube diameter as a function of material parameters. The solid curve represents the equilibrium tube diameter obtained from Eq. (11.17). The dashed curve indicates the limit of stability obtained from Eq. (11.18). The dotted line is a boundary between type-I and type-II superconductor.

### 11.3.4 Isolated flux tube in the Constrained Current Loop model

Let us compare the predictions of the Current Loop model and the Constrained Current Loop model concerning the equilibrium diameter of flux tubes in the low magnetic field limit. In the Constrained Current Loop model, for an isolated flux tube in a thin film of superconductor, the surface term of the magnetic energy $E_{m,s}$ (from Eq. (9.24)) and interfacial energy $E_{int}$ per unit area $\pi R^2$ are written as[102]:

$$\tilde{E}_s = \frac{E_{m,s} + E_{int}}{\pi R^2} = \frac{H_n^2 R}{3\pi^2} + \frac{2\sigma_{SN} d}{R}. \tag{11.19}$$

By minimizing Eq. (11.19) with respect to $R$, the relation:

$$\frac{2R}{d} = \sqrt{\frac{3}{N_B}} \tag{11.20}$$

can be obtained. For comparison with the Current Loop model this relation is plotted in Fig. 11.10 with double logarithm plot.

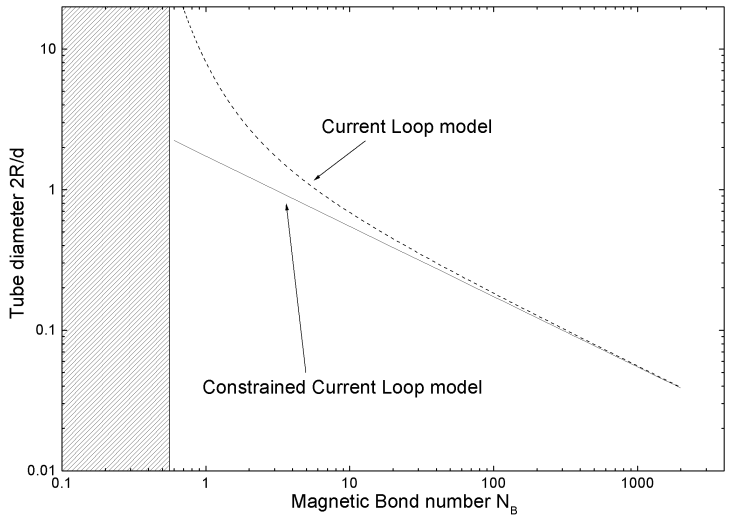


Figure 11.10: Logarithm-logarithm plot of the reduced tube diameter $2R/d$ as a function of the magnetic Bond number $N_B = d/\pi\Delta$. The shaded region corresponds to type-II superconductivity for very thin slabs. The dashed curve is obtained using the Current Loop model Eq. (11.17), the solid curve using the Constrained Current Loop model Eq. (11.20). Both curves represents the equilibrium tube diameter in the limit $H \to 0$, namely, neglecting tube-tube interactions.

As can be seen in Fig. 11.10 when the thickness of sample ($d$) is small, that is, the magnetic Bond number is small, the difference between both curves becomes remarkable. In Sec. 11.4.3 we will show that the Constrained Current Loop model provides a better agreement with our experimental data than the Current Loop model.

## 11.4 Flux tubes diameter and quasi-period

### 11.4.1 Distribution of flux tubes diameters and quasi-periods

**a) Lead**

The distributions of the tubes diameter and period are shown in Fig. 11.11 and in Fig. 11.12, respectively.

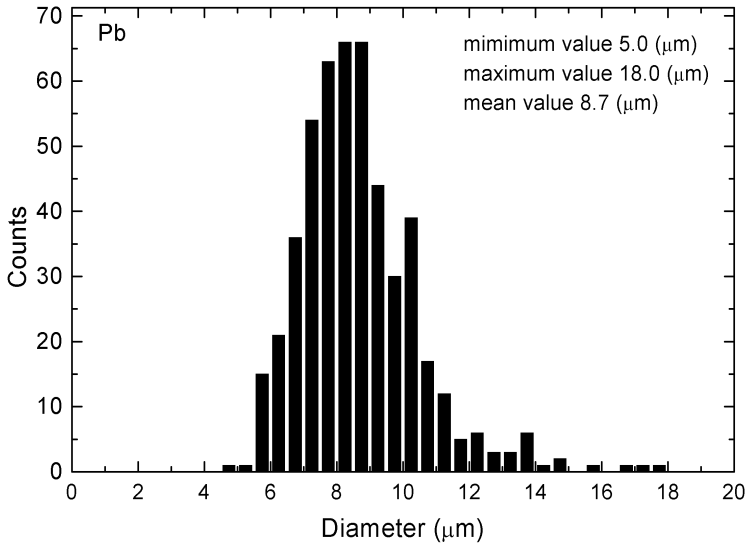


Figure 11.11: The distribution of the flux tube diameter in lead. All magnetic field values are considered.

First it appears that the mean value of the flux tubes diameters and the shape of the distributions are very close for all values of applied magnetic field. Therefore, we show in Fig. 11.11 the cumulative distribution of flux tubes diameters for all values of magnetic field. Note that the width of the distribution is much larger than our optical resolution. It means that this distribution has a physical significance. As it will be seen later, the largest size in the distribution is probably related to the stability limit. This distribution presents also two boundaries. The minimum diameter $\sim$5 $\mu$m is much larger than the optical resolution. Indeed no flux tubes with smaller size exists. The largest size is about 18 $\mu$m.

For the period, the distribution changes with the magnetic field. Fig. 11.12 shows

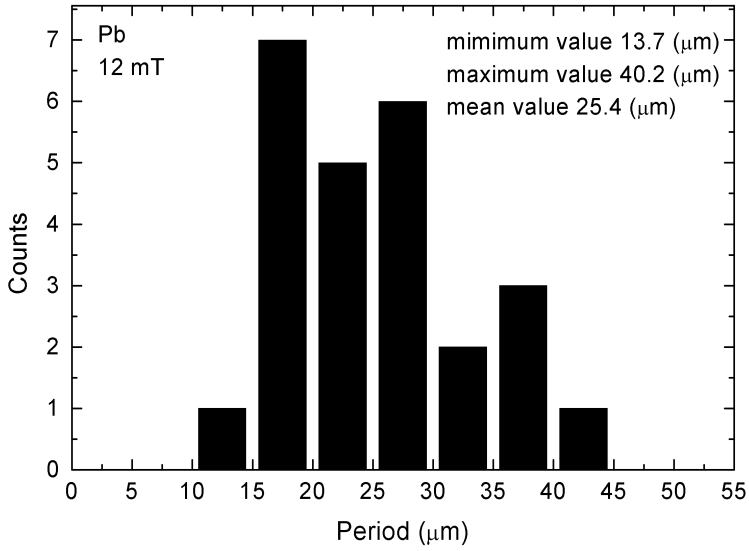


Figure 11.12: The distribution of flux tube quasi-period in lead at $H$=12 mT ($h$=0.16).

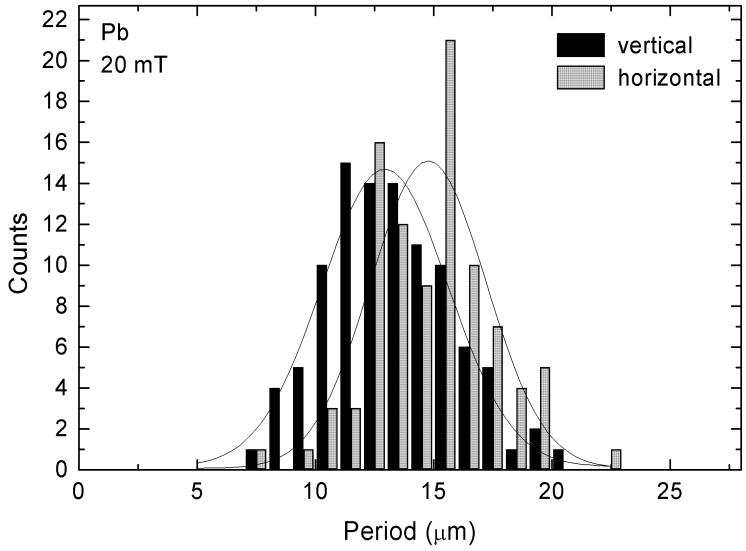


Figure 11.13: The distribution of flux tube quasi-period in lead at $H$=20 mT ($h$=0.27) for vertical direction (black) and horizontal direction (gray). The Gaussian fits are just guides for the eyes.

the distribution for a magnetic field of 12 mT. As it can been seen from image (Fig. 11.2 (b)) flux tubes seem to be roughly aligned along the vertical direction of the image. This is confirmed by the statistical analysis of the period value. As shown in Fig. 11.13 there are two distributions of period values for the vertical and horizontal direction of the image, respectively . Their mean values differ by $\sim 2\ \mu$m. We relate this result to the observation of scratches on the surface of the sample. These scratches are aligned in one direction. They may correspond to regions of slightly smaller thickness. Flux tubes tend to accumulate there because their volume energy is smaller.

**b) Indium**

The distributions of the tubes diameter and period are shown in Fig. 11.14 and in Fig. 11.15, respectively. The mean value of the flux tubes diameters are almost constant for various applied magnetic fields same as for lead. Therefore, we show the cumulative distribution of flux tubes diameter for all values of the magnetic field in Fig. 11.14. There is minimum and maximum size. An example of the period distribution for $h$=0.07 is shown in Fig. 11.15.

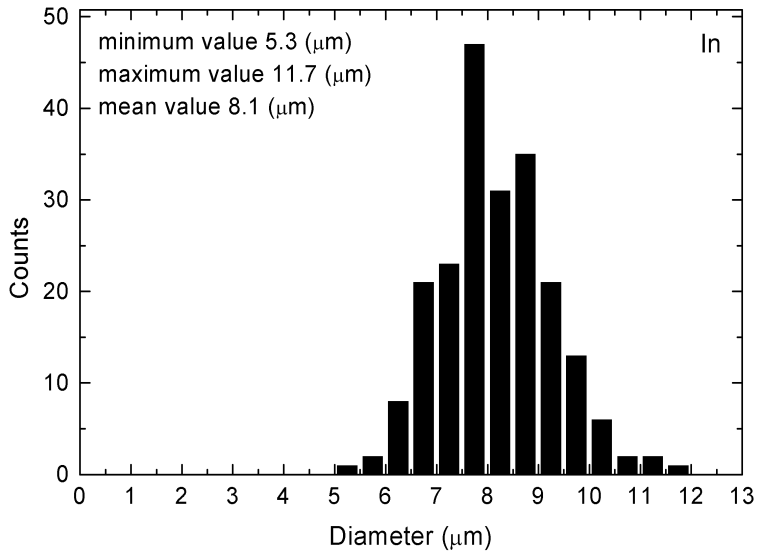


Figure 11.14: The distribution of the flux tube diameter in indium. All magnetic field values are considered.

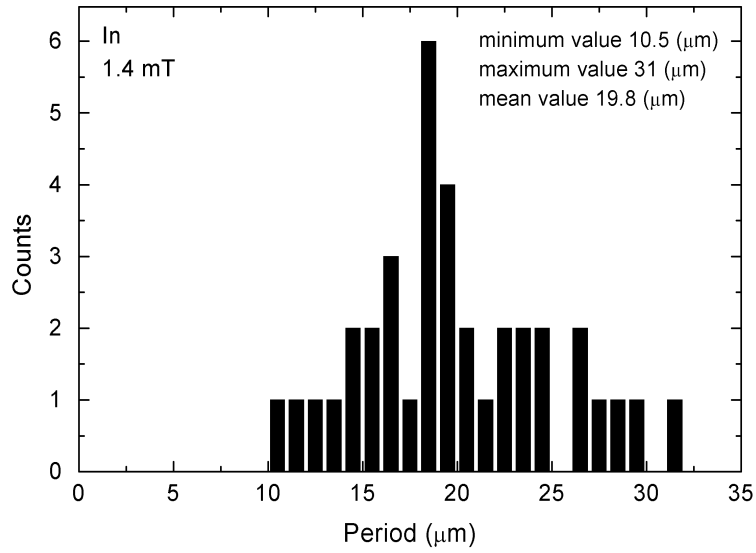


Figure 11.15: The distribution of flux tube quasi-period in indium at $H$=1.4 mT ($h$=0.07).

### 11.4.2 Flux conservation

Prior to further analysis, we must address the following problem: do we measure the real size of flux tubes? There are two possible reasons for measuring not the real size but an apparent size of flux tubes. According to theoretical models, the flux tubes have straight walls well inside the sample. But the normal zones flare out at the surface because the magnetic field can have only a component tangential to the surface due to boundary conditions. This effect is important only when the thickness is comparable to the size of flux tubes, e.g. a case of our indium sample. Furthermore, when there is a gap between the superconductor and the MOL, the divergence of the magnetic field lines may lead to an overestimation of the size of normal zones. We notice that these problems do not affect the measurement of the period. In order to understand whether we obtain a reliable measurement of the flux tube diameter, we consider the magnetic flux conservation.

**a) Lead**

The variation of the flux tube diameter and period for lead sample as a function of the applied magnetic field is shown in Fig. 11.16. The plotted data are average values obtained from the processed good-contrast images.

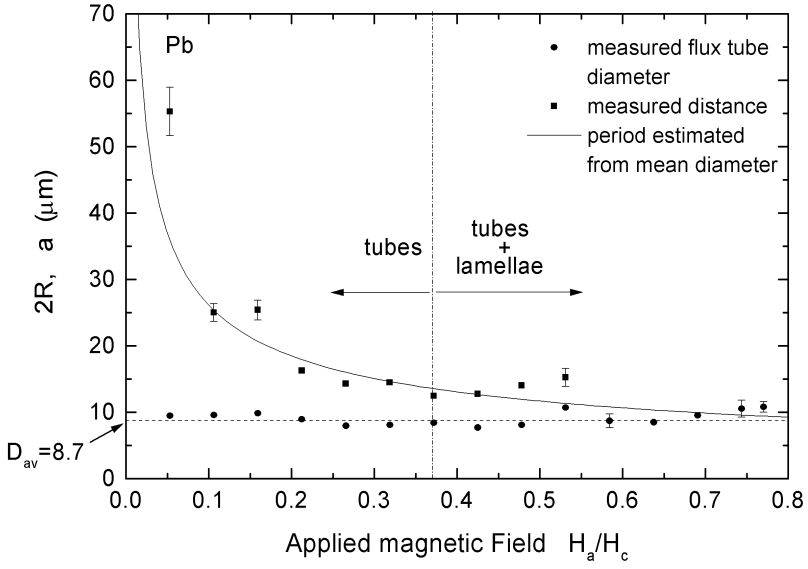


Figure 11.16: Measured flux tubes mean diameter (closed circle) and flux tubes mean period (closed square) as a function of applied magnetic field. The broken line represents the value of the flux tubes mean diameter averaged over all magnetic field values $D_{av}$. The solid line is the period calculated from $D_{av}$ using flux conservation (see text). The error bar is defined $\pm\sigma/\sqrt{n}$, where $\sigma$ and $n$ are the standard deviation and the number of data, respectively.

Assuming that the magnetic field in the normal tubes is equal to $H_c$, from flux conservation the fraction $\rho_n$ of the surface area which is normal must be $\rho_n = H_a/H_c$. As show in Sec. 11.3.2, when the flux lattice of normal tubes is assumed to consist of a triangular array, the flux conservation equation is

$$\rho_n = \frac{H_a}{H_c} = \frac{\pi R^2}{\sqrt{3}a^2/2}. \tag{11.21}$$

From this equation we can calculate the flux tube period (solid curve) from the flux tube mean diameter. This result is in good agreement with the experimental data (closed square) at the magnetic field values $0.1 < H_a/H_c < 0.42$. At low magnetic field $H_a/H_c \sim 0.05$ the experimental data are not reliable because the number of flux tubes in the image is quite small. For the magnetic field value $H_a/H_c > 0.37$ the flux tubes and the flux lamellae coexist. The existence of lamellae is not taken into account in Eq. (11.21). This can explain the small discrepancy between the experimental data and the calculated

curve. Since the flux lamellae dominate for $H_a/H_c > 0.58$, we can not measure distance between tubes correctly. We conclude from this analysis that, for lead, the measured diameter of flux tubes correspond to their real diameter.

**b) Indium**

The measured diameter and period of flux tubes for indium sample as a function of the magnetic field are shown in Fig. 11.17 by closed circles and closed squares, respectively. The solid line shows the period calculated from the measured diameter using flux conservation Eq. (11.21).

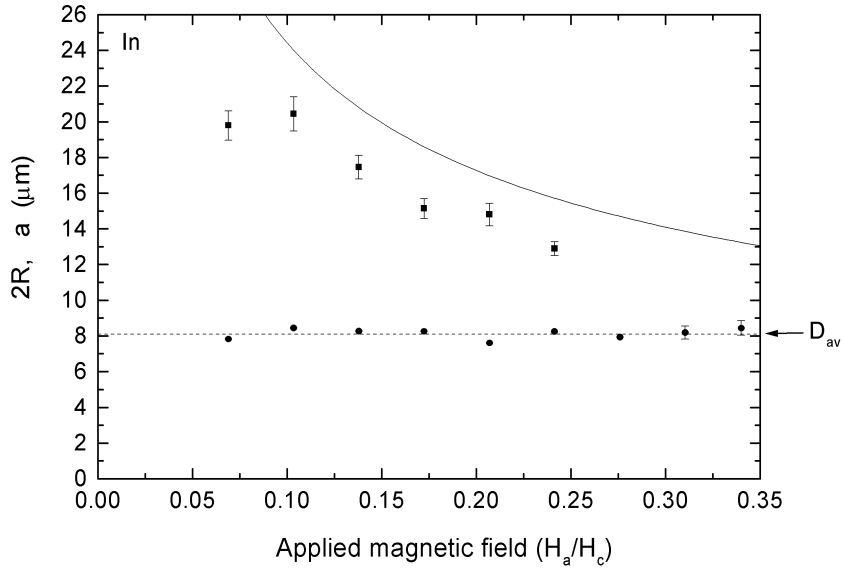


Figure 11.17: Measured flux tubes mean diameter (closed circle) and flux tubes mean period (closed square) as a function of applied magnetic field. The broken line represents the mean value of the flux tubes diameter $D_{av}$ averaged over all magnetic field values. The solid line is the period calculated from $D_{av}$ using flux conservation. The error bar is defined $\pm\sigma/\sqrt{n}$, where $\sigma$ and $n$ are the standard deviation and the number of data, respectively.

There is a discrepancy with the experimental results. This means either that there is not exact flux conservation or that the flux tubes have flared their walls with an inner diameter smaller than the one measured at the surface. The first explanation is reasonable since we image an area close to the edge of the sample. Due to pinning the area fraction of

the normal phase near the edge can be larger than in the interior of the sample. However, whatever the correct explanation, this does not affect the conclusions presented in the next sections. If we have $\rho_n > h$ the experimental data plotted as a function of $h$ should be plotted as a function of $\rho_n$ or equivalently slightly shifted to larger values of $h$. If the inner diameter is smaller than the measured one while $\rho_n = h$ the values of the flux tubes diameter should be slightly reduced (typically by $\sim 10\%$).

### 11.4.3 Comparison between theoretical and experimental results for tubes and lamellae

Here we compare the results of calculation for flux lamella width and flux tube diameter with the experimental results using the Current Loop model and Constrained Current Loop model.

Fig. 11.18 shows the mean width of lamellae as a function of the reduced applied magnetic field $H_0/H_c$ for the 10 $\mu$m indium sample (left) and the 120 $\mu$m lead sample (right). Error bars represent the full width at half maximum of the size distribution. The dashed and solid curves are the prediction of the Current Loop model and Constrained Current Loop model, respectively.

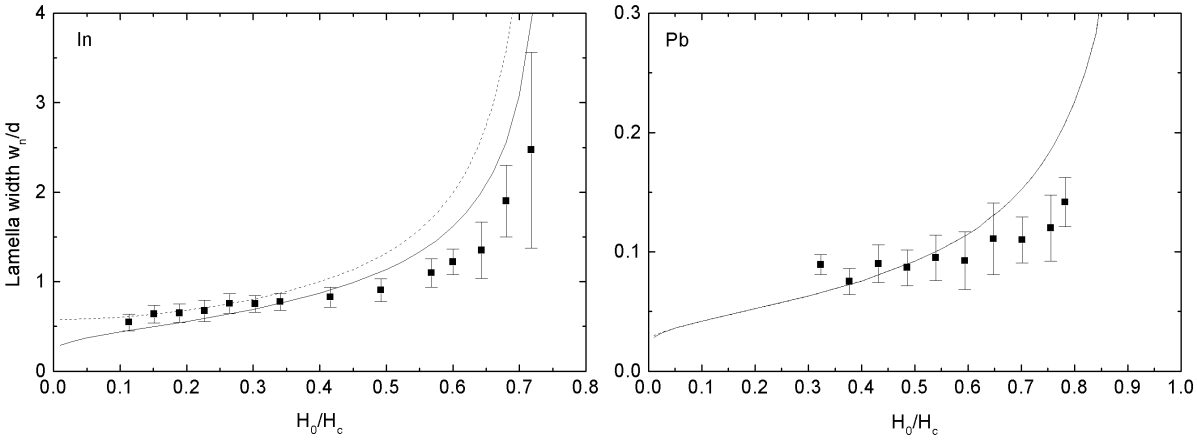


Figure 11.18: Mean reduced width $w_n/d$ as a function of the reduced magnetic field $H_0/H_c$ for a 10 $\mu$m thick indium slab (left) and a 120 $\mu$m thick lead slab (right) at $T = 2$ K. The error bars represent the full width at half maximum of the distributions of lamella width. The dashed and solid curves represent the calculated equilibrium width using the Current Loop model and Constrained Current Loop model with $\Delta = 0.51$ ($N_B = 6.2$) and $\Delta = 0.066$ ($N_B = 580$) for indium and lead, respectively. For lead both curves are superimposed.

In case of low magnetic field ($H_0/H_c < 0.4$ for indium and $H_0/H_c < 0.65$ for lead), the predicted and measured width present a reasonable agreement. It is important to notice that the magnetic Bond number $N_B$ is varied by two orders of magnitude for these two materials. The mean width of the lamellae increases with $H_0/H_c$ almost as predicted. This indicates that the observed lamellae patterns can be described by an equilibrium states, that is to say, the growth of the lamellae is essentially due to the competition between long-range magnetic interactions and short-range surface interactions. This could result from the fact that a number of lamellae are connected to the edges of the slab, thus allowing the magnetic flux to enter continuously from out of the sample. In case of high magnetic field, the width of the lamellae continues to grow. However, the measured values are smaller than the predictions. This discrepancy can be attributed to the effect of pinning. Indeed, in this regime, the intermediate flux pattern consists of a disordered network of interconnected superconducting lamellae. The pinning of domain walls might oppose the motion of superconducting lamellae, thus preventing the free growth of normal state domains.

Next we discuss the tube diameter. Fig. 11.19 shows the mean diameter of tubes for a 10 $\mu$m indium slab (left) and a 120 $\mu$m lead slab (right) as a function of the applied magnetic field. The dashed and solid curves represent the equilibrium diameter calculated using the Current Loop model and Constrained Current Loop model, respectively.

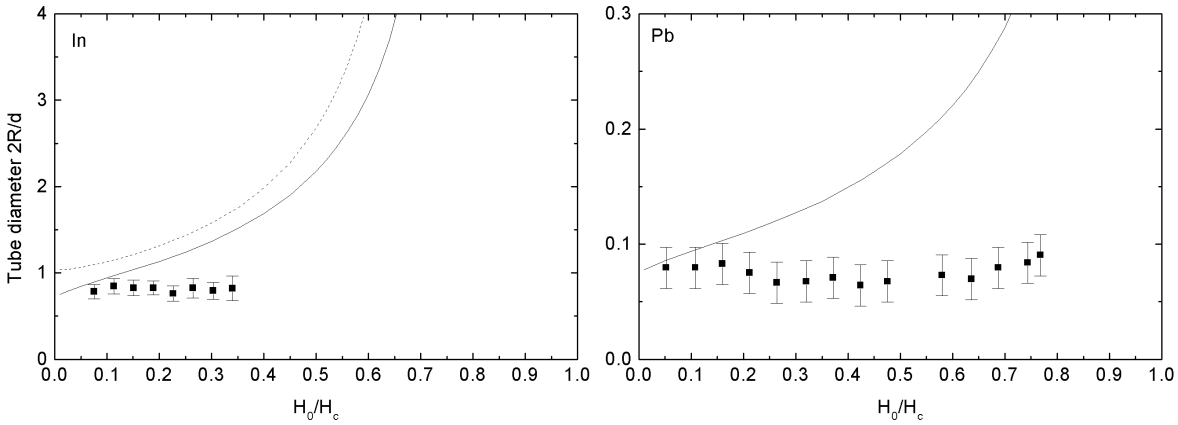


Figure 11.19: Mean tube diameter as a function of the reduced magnetic field $H_0/H_c$ for the 10 $\mu$m thick indium slab (left) and a 120 $\mu$m thick lead slab (right) at $T = 2$ K. The dashed and solid lines represent the equilibrium diameter calculated using the Current Loop model and Constrained Current Loop model with $\Delta = 0.51$ ($N_B = 6.2$) and $\Delta = 0.066$ ($N_B = 580$) for indium and lead, respectively. For lead both curves are superimposed.

Contrary to the lamella width, the tube diameter stays almost constant with increasing applied magnetic field, whereas theoretical results predict an increase of the diameter. This indicates that the mean diameter of tubes is independent of the magnetic interaction between normal state domains. There is agreement between experimental and theoretical values only in the limit $h \to 0$. We remind that, in this limit, the diameter of flux tubes obtained for the lattice model is the same as for an isolated flux tube.

In order to know whether the result of flux tube diameter reflects a general behavior of the flux tube system in superconductors, we collected data from various literatures[112] [113][114]. These data on flux tube diameter are obtained for various values of $d$. They are displayed together in Fig. 11.20 in reduced units $2R_{eq}/\Delta$ as a function of $d/\Delta$.

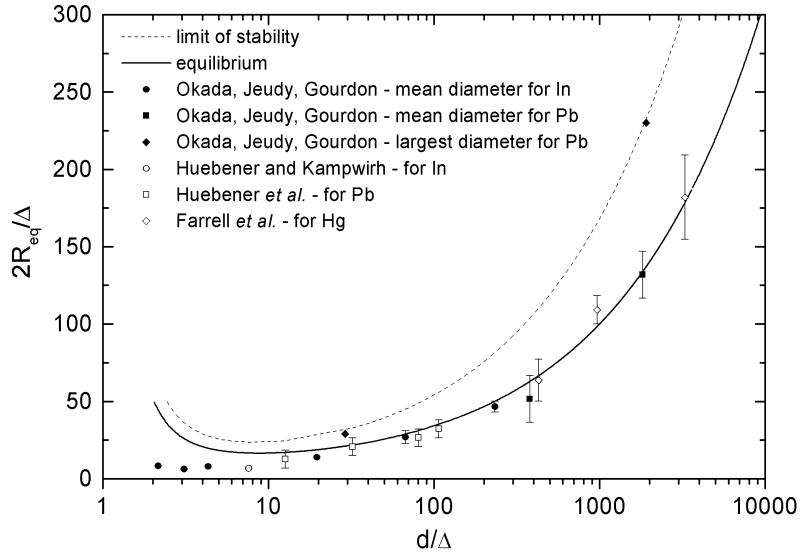


Figure 11.20: The equilibrium tube diameter as a function of material parameters. The solid curve represents the equilibrium tube diameter obtained from Eq. (11.17). The dashed curve indicates the limit of stability obtained from Eq. (11.18). The filled squares and circles were obtained with lead and indium slabs, respectively. The filled lozenges are the largest size of distribution. The references are: Huebener *et al.*[112] (open squares), Huebener and Kampwirth *et al.*[113] (open circles), and Farrell *et al.*[114] (open lozenges).

The values of $\Delta$ for lead, mercury, and indium are 0.066, 0.084, and 0.51, respectively. The solid and broken lines represent the calculated equilibrium diameter and stability

limit of an isolated flux tube, respectively. It is seen that, indeed, in many cases the diameter of flux tubes is close to that of isolated flux tubes. The largest size of distribution (filled lozenge in Fig. 11.20) fits with the dashed line corresponding to the stability limit. This suggests that flux tubes of larger size should be less stable than the flux lamellae.

At low $d/\Delta$ the experimental data are not in agreement with the prediction of the Current Loop model. This would indicate that the Current Loop model can not provide a good description of the system when the thickness of the sample $d$ becomes smaller by 10 times than the interface width between normal and superconducting domains $\Delta$.

In order to compare the predictions of the Current Loop model and of the Constrained Current Loop model with the experimental data it is useful to use the logarithm-logarithm plot of the reduced diameter $2R/d$ as a function of the magnetic Bond number $N_B$ as shown in Fig. 11.21.

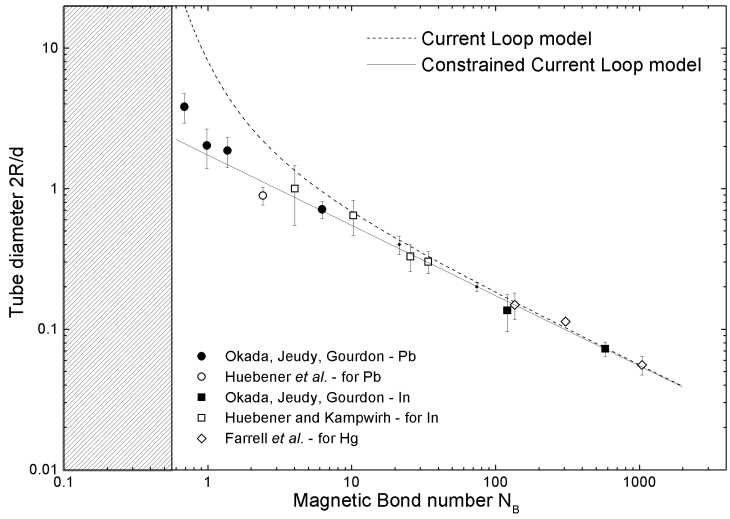


Figure 11.21: Logarithm-logarithm plot of the reduced tube diameter $2R/d$ as a function of the magnetic Bond number $N_B = d/\pi\Delta$. The filled circles and squares were obtained with indium and lead slabs, respectively. The empty squares, circles, and lozenges are reported for lead, indium, and mercury, respectively[112][113][114]. The shaded region corresponds to type-II superconductivity for very thin slabs. The theoretical curves represent the equilibrium tube diameter in the limit $H \to 0$: Current Loop model (dashed curve), Constrained Current Loop model (solid curve).

The dashed curve in Fig. 11.21 represents the diameter calculated in the framework of the Current Loop model in the limit $H \to 0$. A good quantitative agreement is found for $N_B > 20$, while for $N_B < 20$ the predicted diameter is larger than the measured one. The discrepancy increases when $N_B$ decreases. The solid curve in Fig. 11.21 represents the equilibrium diameter calculated using the Constrained Current Loop model. This prediction is in good agreement with the experimental data over three orders of magnitude of the magnetic Bond number ($N_B = 1 - 1000$). This means that the Constrained Current Loop model accurately describes the tube pattern.

It can be concluded i) that the tube mean diameter is solely determined by the competition between the interfacial energy and the energy of the stray magnetic field created by the screening current flowing around the tube, that is to say, tube-tube interaction plays no role, ii) that the Constrained Current Loop model describes experimental results much better than the Current Loop model. Therefore for the intermediate state flux pattern it is important not to consider the current loops interaction as in the free space but to take into account the shielding of magnetic field lines by surface currents on the top and bottom surfaces of the superconducting regions.

### 11.4.4 Impeded growth of flux tubes

In order to understand why the diameter of flux tubes seems to correspond to isolated flux tubes and not to flux tubes organized in a lattice, we measured flux tube diameters at the same value of the magnetic field for increasing and decreasing magnetic field. The results are displayed in Fig. 11.22.

It must be noted that, in the experimental procedure the magnetic field was raised above the tube-to-lamella transition. When the magnetic field in decreasing, part of the flux tubes are generated from lamellae. It is obvious from Fig. 11.22 that there is an hysteretic behavior of the flux tubes diameter as a function of the magnetic field. We conclude that the flux tube system is not in an equilibrium state contrary to the assumption of the theoretical models.

Then we consider a possible explanation. At low magnetic field, there is a diamagnetic band at the edge of the sample. Flux tubes entering the sample have little interaction with other tubes. Then it quite understandable that their diameter is the equilibrium diameter of an isolated tube. This impeded growth of flux tubes results from the nature of the superconducting phase. Here we consider the time variation of the magnetic flux $\Phi$

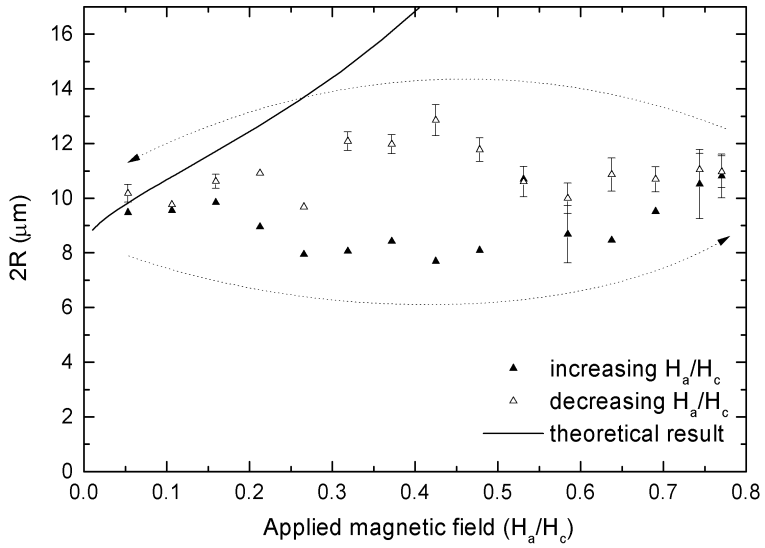


Figure 11.22: Flux tube diameters as a function of the applied magnetic field for increasing and decreasing magnetic field. The hysteresis can be readily observed. The solid line is the diameter calculated in the Current Loop model.

in a flux tube in the superconducting matrix. Maxwell-Faraday equation gives:

$$\frac{d\Phi}{dt} = -\oint \vec{E} d\vec{l}, \tag{11.22}$$

where $\vec{E}$ is the electric field. The contour of the line integral is taken as a closed loop encircling the flux tube in the superconducting matrix at a distance larger than the penetration depth. Since the electric field $\vec{E}$ is zero in the superconducting phase the magnetic flux $\Phi$ within the normal state flux tube must remain constant. Since the magnetic induction in the normal state domain is equal to the critical magnetic field then the size of a normal state flux tube must remain constant. Consequently, flux tube size variation can only result from the movement of an incoming normal state domain.

For the flux tube size to grow, not only another normal state domain has to reach the tube, but also it has to merge with it. However the fusion of two normal state domains is impeded by their repulsive interaction. Moreover, the formation of flux tubes with size much smaller than the equilibrium one is unlikely due to the positive interface energy. As a consequence the continuous growth of isolated normal state domains with the applied magnetic field is prevented.

# Chapter 12

# Conclusion

We studied the magnetic flux patterns in the intermediate state of type I superconducting thin indium and lead films with the high-resolution Faraday imaging technique, using not only conventional Eu-based thin layers but also semimagnetic semiconductor as magneto-optic layers.

Semimagnetic semiconductor $Cd_{1-x}Mn_xTe$ quantum wells were used as an application device: a novel type of magneto-optic layer. These magneto-optic layers were recently developed at GPS, in order to get high-resolution Faraday microscopy images. They consist of semimagnetic semiconductor $Cd_{1-x}Mn_xTe$ quantum wells embedded in a semiconductor-metal optical cavity. The most advantageous point of this kind of magneto-optic layer is that there is no self-magnetic ordering due to the paramagnetic behavior of Mn ions, hence there is no magnetic influence on the superconducting film.

Our results for the superconducting films showed that the magnetic flux pattern consisted of a disordered array of flux tubes at low applied magnetic field with a transition towards a labyrinthine structure of flux lamellae with increasing applied magnetic field. As in several other quasi-two dimensional systems with two phases, the domain structure is governed by the competition between long-range interaction (magnetic interaction between normal phase domains) and short-range forces due to the existence of a positive interfacial energy between the normal and superconducting phases.

We compared the experimental results at low magnetic field and the predictions in the frame of the Current Loop model (or equivalent Surface Charge Model) assuming that cylindrical flux tubes are arranged in a triangular lattice. For indium as well as for lead, the measured average tube diameter stays almost constant with increasing applied magnetic field whereas the theoretical results predict an increase of the diameter. This

behavior differs from the one of flux lamellae, the width of which increases with the applied magnetic field in much closer agreement with the theoretical predictions. This indicates that the flux tube pattern corresponds to an out-of-equilibrium system contrary to the usual assumptions in the intermediate state models.

However, the predicted diameter of flux tubes in the limit of vanishing magnetic field, i.e. neglecting inter-bubble magnetic interaction, is in good quantitative agreement with the measured average diameter at least when the sample thickness is large compare with the diameter of flux tubes. This means that the average flux tube diameter is only determined by the interfacial energy and the self-magnetic energy of the tube, the magnetic interaction between flux tubes playing no role. From these results we could determine that the only two parameters that control the flux tube diameter are the sample thickness and superconducting-normal interface parameter. These results also illustrate a specificity of the superconducting medium with respect to other two-dimensional two-phase systems. Once some flux has penetrated in the sample and forms an isolated normal domain completely surrounded by the superconducting matrix, Maxwell-Faraday equation insures flux conservation. This means that the growth of isolated flux tubes is impeded. This situation is different for flux lamellae since most of them are connected to the edge of the sample and continuous flux penetration can occur.

For thin samples we found that the Constrained Current Loop model, which is a modification of the Current Loop model and Surface Charge model, provides a much better agreement between the calculated equilibrium flux tube diameter in the limit of zero magnetic field and the measured average diameter of flux tubes. This model, by considering only the magnetic interaction between surface charges of the same face, allows to take into consideration the surface screening currents on the top and bottom surfaces of the films. This study will be published in paper[102].

The next step in this study would be to perform time-resolved Faraday imaging. One interesting feature to study is the influence of the magnetic field-sweeping rate on the domain pattern. For instance we observed a much better ordered stripe lattice when the magnetic field is abruptly raised. In some cases reorganization of domain patterns on a time scale of one minute was observed. The interplay of temperature, illumination intensity, magnetic field-sweeping rate has to be studied.

# Part III

# Appendix

# Appendix A

# Appendix for Part I

## A.1 Validity of approximation for Brillouin function

Since magnetization through $Mn^{2+}$ in $Cd_{1-x}Mn_xTe$ is described by the standard Brillouin function $B_S$, the Zeeman splitting of valence and conduction band also obeys the $B_S$. The Brillouin function is significant in paramagnetic theory, however its calculation is vexatious on account of hyperbolic cotangent. Therefore rough estimation for Brillouin function render us feel ease to cogitate $Mn^{2+}$ spin behavior. Here its approximation are explained and its validity are appraised for practical use.

The Brillouin function is written as:

$$B_S(u) = \frac{2S+1}{2S}\coth\left(\frac{2S+1}{2S}u\right) - \frac{1}{2S}\coth\left(\frac{1}{2S}u\right), \tag{A.1}$$

where $S$ is spin quantum number. Since $\coth(u) = \tanh^{-1}(u)$ and

$$\tanh(u) \simeq u - \frac{1}{3}u^3 + \frac{2}{15}u^5 - \frac{17}{315}u^7, \tag{A.2}$$

then

$$\begin{aligned} B_S(u) &\simeq \frac{2S+1}{2S}\frac{1}{v}\left(1-\frac{1}{3}v^2+\frac{2}{15}v^4\right)^{-1} - \frac{1}{2S}\frac{1}{w}\left(1-\frac{1}{3}w^2+\frac{2}{15}w^4\right)^{-1} \\ &= \frac{2S+1}{2S}\frac{1}{v}\left(1+\frac{1}{3}v^2-\frac{2}{15}v^4\right) - \frac{1}{2S}\frac{1}{w}\left(1+\frac{1}{3}w^2-\frac{2}{15}w^4\right) \\ &= \frac{1}{3u}(v^2-w^2), \end{aligned} \tag{A.3}$$

where $v = (2S+1)u/2S$ and $w = u/2S$. Therefore

$$B_S(u) = \frac{1}{u}\left(\frac{2S+1}{2S}\right)^2\frac{u^2}{3} - \frac{1}{u}\left(\frac{1}{2S}\right)^2\frac{u^2}{3} = \frac{u}{3}\frac{S+1}{S}. \tag{A.4}$$

$S = 5/2$ for half-filled $3d$-shell of $Mn^{2+}$, then

$$B_{5/2}(u) = \frac{7}{15}u. \tag{A.5}$$

With Eq. (A.5) the Zeeman splitting energy of conduction and valence band are obtained as:

$$\Delta E_v(B) = \frac{1}{2}N_0\alpha x S_{\mathrm{eff}}(x)B_{5/2}\left(\frac{5}{2}\frac{g_{\mathrm{Mn}}\mu_B B}{K_B(T+T_0(x))}\right) = \frac{7}{12}N_0\alpha x S_{\mathrm{eff}}(x)\frac{g_{\mathrm{Mn}}\mu_B B}{K_B(T+T_0)}, \tag{A.6}$$

$$\Delta E_c(B) = \frac{1}{2}N_0\beta x S_{\mathrm{eff}}(x)B_{5/2}\left(\frac{5}{2}\frac{g_{\mathrm{Mn}}\mu_B B}{K_B(T+T_0(x))}\right) = \frac{7}{12}N_0\beta x S_{\mathrm{eff}}(x)\frac{g_{\mathrm{Mn}}\mu_B B}{K_B(T+T_0)}, \tag{A.7}$$

respectively. $S_{\mathrm{eff}}(x)$ and $T_0(x)$ are written in Eq. (1.15). Each parameters in Eq. (A.6) and Eq. (A.7) are explained below Eq. (1.15). Fig. A.1 shows the Zeeman splitting of valence band $m_J = -3/2$ level without approximation (Eq. (1.14)) and with approximation (Eq. (A.5)) at 4 K in $Cd_{0.8}Mn_{0.2}Te$.

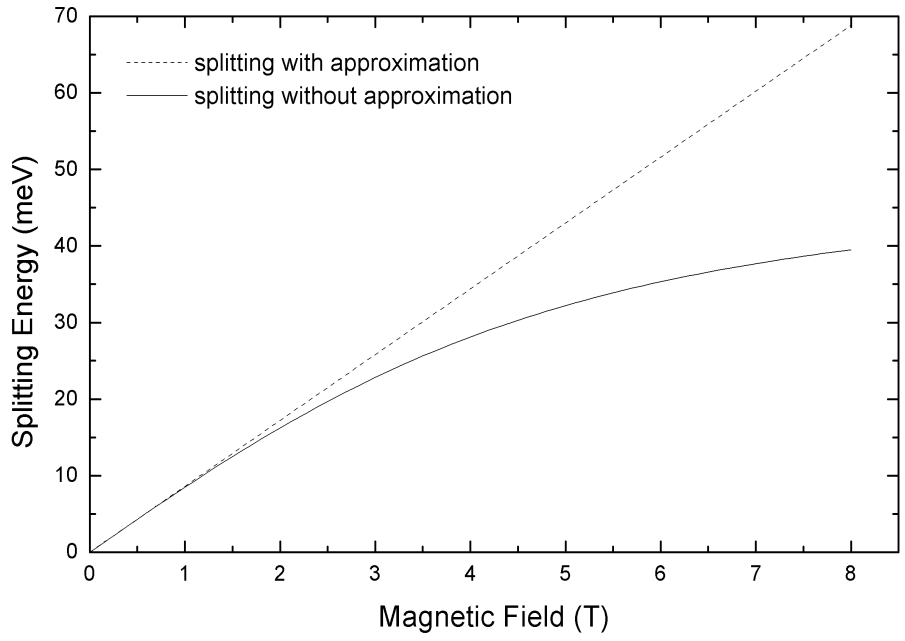


Figure A.1: The comparison of Zeeman splitting of valence band $m_J = -3/2$ level with (dashed line) and without (solid line) approximation at 4 K in $Cd_{0.8}Mn_{0.2}Te$.

The amplitude of Zeeman splitting grows 40 meV at 8 T without approximation (saturation value is 46 meV), while the rough calculation gives linear increasing function. An

approximate function is in error by less than 0.1 meV up to magnetic field $B \simeq 1$ T.
The effective $g$-factors are expressed as:

$$\begin{aligned} g_{\mathrm{eff},c} &= \frac{7}{12} N_0 \alpha x S_{\mathrm{eff}}(x) \frac{g_{\mathrm{Mn}}}{K(T+T_0)} \\ g_{\mathrm{eff},v} &= \frac{7}{12} N_0 \beta x S_{\mathrm{eff}}(x) \frac{g_{\mathrm{Mn}}}{K(T+T_0)}. \end{aligned} \tag{A.8}$$

## A.2 Exchange interaction between $Mn^{2+}$ ions

The magnetic moments of $Mn^{2+}$ in CdTe matrix are coupled with each other, especially through the exchange interaction. Both the nearest-neighbor exchange interaction described by the integral $J_{NN}$(=−6.3 K) and the next-nearest-neighbor exchange described by $J_{NNN}$(=−1.3 K) are antiferromagnetic.
The thermal average value $\langle S_z \rangle$ of each $Mn^{2+}$ in $Cd_{1-x}Mn_xTe$ is given with statistical equations as:

$$\langle S_z \rangle = -S_{\mathrm{eff}}(x) B_{5/2} \left( \frac{5}{2} \frac{g_{\mathrm{Mn}} \mu_B B}{k_B (T + T_0(x))} \right), \tag{A.9}$$

with

$$S_{\mathrm{eff}}(x) = \frac{5}{2} \left( P_1(x) + \frac{P_O}{3} + \frac{P_F}{15} \right), \tag{A.10}$$

where $P_1(x) = (1-x)^{12}$ is the probability of isolated $Mn^{2+}$, $P_O(x) = 18x^2(1-x)^{23}(7-5x)$ and $P_F(x) = 24x^2(1-x)^{22}$ are that of $Mn^{2+}$ that constitutes open and closed triplet, respectively. The probability of paired $Mn^{2+}$ is expressed as $P_2(x) = 12x(1-x)^{18}$, however, this pair dose not participate in magnetization.
Fig. A.2 shows the comparison of $xS_{\mathrm{eff}}$ with using Eq. (A.10) and empirical equation Eq. (1.15).
Since it is found big disparity between the statistical curve and the empirical one at $x > 0.05$, Eq. (A.10) could be valid at lower Mn concentration $x$ up to 0.05. The largest magnetization would come along at $x \simeq 0.08$ by statistics, while it might be happen at $x \simeq 0.16$ from the empirical equation.

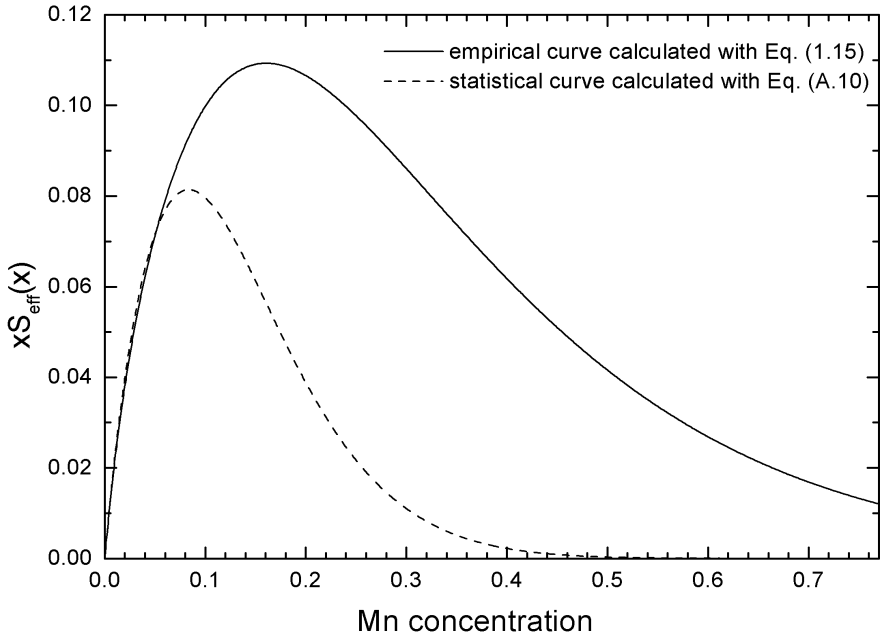


Figure A.2: The comparison of $xS_{\text{eff}}$ with empirical equation (solid line) and with theoretical equation (dashed line) as a function of Mn concentration.

# Appendix B

# Appendix for Part II

## B.1 Magnetic energy

The magnetic free energy at normal region $E_m$ is expressed

$$E_m = \frac{1}{8\pi}\int_{\substack{full\\space}} (\vec{H}_a + \vec{H}_M)^2\, dv = \frac{1}{8\pi}\int \vec{H}_a^2\, dv + \frac{1}{4\pi}\int \vec{H}_a\vec{H}_M\, dv + \frac{1}{8\pi}\int \vec{H}_M^2\, dv. \quad \text{(B.1)}$$

The first term of the right-hand side in Eq. (B.1) is

$$\frac{1}{8\pi}\int \vec{H}_a^2\, dv = \frac{H_a^2}{8\pi}V. \quad \text{(B.2)}$$

The second term of the right-hand side in Eq. (B.1) is

$$\begin{aligned}
\frac{1}{4\pi}\int \vec{H}_a\vec{H}_M\, dv &= \frac{1}{4\pi}\int (\vec{H}_a + \vec{H}_M - \vec{H}_M)\cdot\vec{H}_M\, dv \\
&= \frac{1}{4\pi}\int (\vec{H}_a + \vec{H}_M)\cdot\vec{H}_M\, dv - \frac{1}{4\pi}\int \vec{H}_M^2\, dv \\
&= \frac{1}{4\pi}\int (\vec{H}_a + \vec{H}_M)\cdot(\vec{H}_a + \vec{H}_M - \vec{H}_a)\, dv - \frac{1}{4\pi}\int \vec{H}_M^2\, dv \\
&= \frac{1}{4\pi}\int (\vec{H}_a + \vec{H}_M)^2\, dv - \frac{H_a}{4\pi}\int (\vec{H}_a + \vec{H}_M)\, dv - \frac{1}{4\pi}\int \vec{H}_M^2\, dv \\
&= \frac{1}{4\pi}H_n^2\rho_n V - \frac{1}{4\pi}H_aH_n\rho_n V - \frac{1}{4\pi}\int \vec{H}_M^2\, dv \\
&= \frac{1}{4\pi}H_nH_a(1-\rho_n)V - \frac{1}{4\pi}\int \vec{H}_M^2\, dv, \quad \text{(B.3)}
\end{aligned}$$

where the relation $H_n\rho_n = H_a$ is taken into account when changing the fifth equation into last one.

Then Eq. (B.1) is expressed

$$E_m = \frac{H_a^2}{8\pi}V + \frac{H_nH_a}{4\pi}(1-\rho_n)V - \frac{1}{8\pi}\int \vec{H}_M^2\, dv. \quad \text{(B.4)}$$

The third term of the right-hand side in Eq. (B.4) is

$$\begin{aligned} -\frac{1}{8\pi}\int \vec{H}_M^2\, dv &= -\frac{1}{8\pi}\int \vec{H}_M \cdot \mathrm{rot}\vec{A}_M\, dv \\ &= -\frac{1}{8\pi}\int \mathrm{div}(\vec{A}_M \times \vec{H}_M)\, dv - \frac{1}{8\pi}\int \vec{A}_M \cdot \mathrm{rot}\vec{H}_M\, dv. \end{aligned} \tag{B.5}$$

The first term of the right-hand side in Eq. (B.5) goes to zero,

$$\int_v \mathrm{div}(\vec{A}_M \times \vec{H}_M)\, dv = \oint\oint (\vec{A}_M \times \vec{H}_M)\, dS \overset{r\to\infty}{\longrightarrow} 0. \tag{B.6}$$

Then, using Maxwell equation $4\pi\vec{j}/c = \mathrm{rot}\vec{H}$, we obtain

$$\begin{aligned} -\frac{1}{8\pi}\int \vec{H}_M^2\, dv &= -\frac{1}{8\pi}\int \vec{A}_M \cdot \mathrm{rot}\vec{H}_M\, dv = -\frac{1}{2c}\int \vec{j}\cdot\vec{A}_M\, dv \\ &= -\frac{1}{2c}\sum_i \oint \vec{j}_s(\vec{r}_i)\cdot\vec{A}_M(\vec{r}_i)\, ds. \end{aligned} \tag{B.7}$$

The vector potential $\vec{A}_M(\vec{r}_i)$ is expressed

$$\vec{A}_M(\vec{r}_i) = \frac{1}{c}\sum_j \oint ds' \frac{\vec{j}_s(\vec{r}_j)}{|\vec{r}_j - \vec{r}_i|}, \tag{B.8}$$

then Eq. (B.5) is

$$\begin{aligned} -\frac{1}{8\pi}\int \vec{H}_M^2\, dv &= -\frac{1}{2c^2}\sum_{ij} \oint ds \oint ds' \frac{\vec{j}_s(\vec{r}_j)\cdot\vec{j}_s(\vec{r}_i)}{|\vec{r}_j - \vec{r}_i|} \\ &= -\frac{M^2}{2}\sum_{ij} \oint ds \oint ds' \frac{\vec{t}_i\cdot\vec{t}_j}{R_{ij}} = -\frac{M^2}{2}\sum_{ij} \oint ds \oint ds' \frac{\vec{t}_i\cdot\vec{t}_j}{R_{ij}}. \end{aligned} \tag{B.9}$$

With taking the sample thickness $d$ into consideration, Eq. (B.5) becomes

$$-\frac{1}{8\pi}\int \vec{H}_M^2\, dv = -\frac{M^2}{2}\sum_{ij}\int_0^d dz \int_0^d dz' \oint ds \oint ds' \frac{\vec{t}_i\cdot\vec{t}_j}{R_{ij}} \tag{B.10}$$

Finally $E_m$ takes the form

$$E_m = \frac{H_a^2}{8\pi}V + \frac{H_n H_a}{4\pi}(1-\rho_n)V - \frac{M^2}{2}\sum_{ij}\int_0^d dz \int_0^d dz' \oint ds \oint ds' \frac{\vec{t}_i\cdot\vec{t}_j}{R_{ij}}. \tag{B.11}$$

## B.2 Self- and mutual form magnetic energy

We calculate the self- and mutual-induction term as:

$$E_m = -\frac{M^2}{2}\sum_i\sum_j \int_0^d dz_i \int_0^d dz_j \oint ds_i \oint ds_j \frac{\vec{t}_i\cdot\vec{t}_j}{R_{ij}} \tag{B.12}$$

where $M=-H_n/4\pi$ is magnetization, $\vec{t}_i\cdot\vec{t}_j=\cos(\theta_j-\theta_i)$, $R_{ij}=|\vec{r}_j-\vec{r}_i|$, and $\vec{r}_i$, $\vec{r}_j$ are

$$\vec{r}_i=\begin{pmatrix} R\cos\theta_i \\ R\sin\theta_i \\ z_i \end{pmatrix}, \quad \vec{r}_j=\begin{pmatrix} na+\frac{1}{2}pa+R\cos\theta_j \\ \frac{\sqrt{3}}{2}pa+R\sin\theta_j \\ z_j \end{pmatrix},$$

respectively. By using Fourier transform:

$$\frac{1}{R_{ij}}=\frac{1}{(2\pi)^3}\int d^3q\,\frac{4\pi}{q^2}e^{i\vec{q}(\vec{t}_j-\vec{t}_i)}, \tag{B.13}$$

Eq. (B.12) is expressed

$$\begin{aligned}
E_m &= -\frac{M^2}{2}\sum_{n'}\sum_{n''}\sum_{p'}\sum_{p''}\int_0^d dz_i\int_0^d dz_j\int_0^{2\pi} R\,d\theta_i\int_0^{2\pi} R\,d\theta_j\cos(\theta_j-\theta_i) \\
&\quad\times\frac{1}{(2\pi)^3}\int d^3q\,\frac{4\pi}{q^2}e^{i[q_x\{na+\frac{1}{2}pa+R(\cos\theta_j-\cos\theta_i)\}+q_y\{\frac{\sqrt{3}}{2}pa+R(\sin\theta_j-\sin\theta_i)\}+q_z(z_j-z_i)]} \\
&= -\frac{M^2}{2}\cdot\frac{1}{2}\sum_{n'+n''}\sum_{n'-n''}\cdot\frac{1}{2}\sum_{p'+p''}\sum_{p'-p''}\int_0^d dz_i\int_0^d dz_j\int_0^{2\pi} R\,d\theta_i\int_0^{2\pi} R\,d\theta_j\cos(\theta_j-\theta_i) \\
&\quad\times\frac{1}{(2\pi)^3}\int d^3q\,\frac{4\pi}{q^2}e^{i[q_x\{na+\frac{1}{2}pa+R(\cos\theta_j-\cos\theta_i)\}+q_y\{\frac{\sqrt{3}}{2}pa+R(\sin\theta_j-\sin\theta_i)\}+q_z(z_j-z_i)]} \\
&= -\frac{M^2R^2}{4\pi^2}N_AN_B\sum_{n=-\infty}^{\infty}\sum_{p=-\infty}^{\infty}\int_0^d dz_i\int_0^d dz_j\int_0^{2\pi} d\theta_i\int_0^{2\pi} d\theta_j\cos(\theta_j-\theta_i) \\
&\quad\times\int d^3q\,\frac{1}{q^2}e^{i[q_x\{na+\frac{1}{2}pa+R(\cos\theta_j-\cos\theta_i)\}+q_y\{\frac{\sqrt{3}}{2}pa+R(\sin\theta_j-\sin\theta_i)\}+q_z(z_j-z_i)]},
\end{aligned} \tag{B.14}$$

where

$$2N_A=\sum_{n'+n''},\quad 2N_B=\sum_{p'+p''},\quad n'-n''=n,\quad p'-p''=p.$$

Using the following formulas:

$$\begin{aligned}
\sum_{n=-\infty}^{\infty}e^{iq_xna} &= \frac{2\pi}{a}\sum_{m=-\infty}^{\infty}\delta\left(q_x-m\frac{2\pi}{a}\right), \\
\sum_{p=-\infty}^{\infty}e^{i\frac{1}{2}(q_x+\sqrt{3}q_y)pa} &= \frac{2\pi}{a}\sum_{t=-\infty}^{\infty}\delta\left(\frac{1}{2}(q_x+\sqrt{3}q_y)-t\frac{2\pi}{a}\right),
\end{aligned}$$

then $E_m$ is written as:

$$\begin{aligned}
E_m &= -\frac{M^2R^2}{4\pi^2}N_AN_B\left(\frac{2\pi}{a}\right)^2\sum_{m=-\infty}^{\infty}\sum_{t=-\infty}^{\infty}\int_0^d dz_i\int_0^d dz_j\int_0^{2\pi}d\theta_i\int_0^{2\pi}d\theta_j\cos(\theta_j-\theta_i)\\
&\quad\times\int\frac{d^3q}{q^2}\delta\left(q_x-m\frac{2\pi}{a}\right)e^{iq_xR(\cos\theta_j-\cos\theta_i)}\\
&\quad\times\delta\left(\frac{1}{2}(q_x+\sqrt{3}q_y)-t\frac{2\pi}{a}\right)e^{iq_yR(\sin\theta_j-\sin\theta_i)}\times e^{iq_z(z_j-z_i)}\\
&= -\frac{M^2R^2}{4\pi^2}N_AN_B\frac{2}{\sqrt{3}}\left(\frac{2\pi}{a}\right)^2\sum_{m=-\infty}^{\infty}\sum_{t=-\infty}^{\infty}\int_0^d dz_i\int_0^d dz_j\int_0^{2\pi}d\theta_i\int_0^{2\pi}d\theta_j\cos(\theta_j-\theta_i)\\
&\quad\times\exp i\frac{2\pi R}{a}m(\cos\theta_j-\cos\theta_i)\cdot\exp i\frac{2\pi R}{a}\frac{2t-m}{\sqrt{3}}(\sin\theta_j-\sin\theta_i)\\
&\quad\times\int\frac{dq_z}{(2\pi/a)^2(4m^2+4t^2-4mt)/3+q_z^2}\exp iq_z(z_j-z_i),
\end{aligned}\tag{B.15}$$

where $dq_xdq_ydq_z=d^3q$, $(2\pi/a)^2(4m^2+4t^2-4mt)/3+q_z^2=q_x^2+q_y^2+q_z^2=q^2$.

First we calculate the integral with respect to $z$ component in Eq. (B.15).

$$\begin{aligned}
I_z &= \int_0^d dz_j\int_0^d dz_i\exp iq_z(z_j-z_i)=\int_0^d dz_j\exp(iq_zz_i)\int_0^d dz_j\exp(-iq_zz_i)\\
&= \frac{1}{iq_z}\{\exp(iq_zd)-1\}\cdot\frac{-1}{iq_z}\{\exp(-iq_zd)-1\}=\frac{2(1-cosq_zd)}{q_z^2},
\end{aligned}\tag{B.16}$$

then Eq. (B.15) becomes

$$\begin{aligned}
E_m &= -\frac{M^2R^2}{\sqrt{3}\pi^2}N_AN_B\left(\frac{2\pi}{a}\right)^2\sum_{m=-\infty}^{\infty}\sum_{t=-\infty}^{\infty}\int_0^{2\pi}d\theta_i\int_0^{2\pi}d\theta_j\cos(\theta_j-\theta_i)\\
&\quad\times\exp i\frac{2\pi R}{a}m(\cos\theta_j-\cos\theta_i)\cdot\exp i\frac{2\pi R}{a}\frac{2t-m}{\sqrt{3}}(\sin\theta_j-\sin\theta_i)\\
&\quad\times\int\frac{1-\cos q_zd}{q_z^2\left\{(2\pi/a)^2(4m^2+4t^2-4mt)/3+q_z^2\right\}}\,dq_z.
\end{aligned}\tag{B.17}$$

We calculate the $q_z$ component in Eq. (B.15). For $m=t=0$,

$$E_m=-\frac{M^2R^2}{\sqrt{3}\pi^2}N_AN_B\left(\frac{2\pi}{a}\right)^2\int_0^{2\pi}d\theta_i\int_0^{2\pi}d\theta_j\cos(\theta_j-\theta_i)\int_{-\infty}^{\infty}\frac{1-\cos q_zd}{q_z^4}\,dq_z=0\tag{B.18}$$

Therefore, henceforth we neglect for $m=t=0$. Eq. (B.17) becomes

$$\begin{aligned}
E_m &= -\frac{4M^2R^2}{\sqrt{3}a^2}N_AN_B\sum_{m=-\infty}^{\infty}{}'\sum_{t=-\infty}^{\infty}{}'\int_0^{2\pi}d\theta_i\int_0^{2\pi}d\theta_j\cos(\theta_j-\theta_i)\\
&\quad\times\exp i\frac{2\pi R}{a}\left\{m(\cos\theta_j-\cos\theta_i)+\frac{2t-m}{\sqrt{3}}(\sin\theta_j-\sin\theta_i)\right\}\\
&\quad\times\int_{-\infty}^{\infty}\frac{1-\cos q_zd}{q_z^2\left\{(2\pi/a)^2(4m^2+4t^2-4mt)/3+q_z^2\right\}}\,dq_z,
\end{aligned}\tag{B.19}$$

where the prime indicates that the summation is taken on all integers except $m = t = 0$. Using

$$\begin{aligned}\int_{-\infty}^{\infty} \frac{dq_z(1-\cos q_z d)}{q_z^2(q_z^2+A^2)} &= \frac{1}{A^2}\left(\pi d - \frac{\pi}{A}\left(1-\exp(-Ad)\right)\right) \\ &= \frac{\pi d}{A^2}\left\{1-\frac{1-\exp(-Ad)}{Ad}\right\}, \end{aligned} \tag{B.20}$$

where $A^2 \equiv (2\pi/a)^2(4m^2+4t^2-4mt)/3 \neq 0$, then Eq. (B.19) becomes

$$\begin{aligned} E_m &= -\frac{\sqrt{3}dM^2R^2N_AN_B}{4\pi} \sum_{m=-\infty}^{\infty}{}' \sum_{t=-\infty}^{\infty}{}' \frac{1}{m^2+t^2-mt} \int_0^{2\pi} d\theta_i \int_0^{2\pi} d\theta_j \cos(\theta_j-\theta_i) \\ &\quad \times \exp i\frac{2\pi R}{a}\left\{m(\cos\theta_j-\cos\theta_i)+\frac{2t-m}{\sqrt{3}}(\sin\theta_j-\sin\theta_i)\right\} \\ &\quad \times \left\{1-\frac{1-\exp(-4\pi d\sqrt{m^2+t^2-mt}/\sqrt{3}a)}{4\pi d\sqrt{m^2+t^2-mt}/\sqrt{3}a}\right\}. \end{aligned} \tag{B.21}$$

Next we calculate the integral with respect to θ component in Eq. (B.21),

$$\begin{aligned} I_\theta &= \int_0^{2\pi} d\theta_i \int_0^{2\pi} d\theta_j \cos(\theta_j-\theta_i) \exp i\frac{2\pi R}{a}\left\{m(\cos\theta_j-\cos\theta_i)+\frac{2t-m}{\sqrt{3}}(\sin\theta_j-\sin\theta_i)\right\} \\ &= \int_0^{2\pi} d\theta_i \int_0^{2\pi} d\theta_j (\cos\theta_j\cos\theta_i+\sin\theta_j\sin\theta_i) \\ &\quad \times \exp\{iz(\cos\gamma\cos\theta_j+\sin\gamma\sin\theta_j)\} \times \exp\{-iz(\cos\gamma\cos\theta_i+\sin\gamma\sin\theta_i)\} \\ &= \int_0^{2\pi} d\theta_j \cos\theta_j \exp\{iz\cos(\theta_j-\gamma)\} \int_0^{2\pi} d\theta_i \cos\theta_i \exp\{-iz\cos(\theta_i-\gamma)\} \\ &+ \int_0^{2\pi} d\theta_j \sin\theta_j \exp\{iz\cos(\theta_j-\gamma)\} \int_0^{2\pi} d\theta_i \sin\theta_i \exp\{-iz\cos(\theta_i-\gamma)\}, \end{aligned} \tag{B.22}$$

where

$$z = \frac{4\pi R}{\sqrt{3}a}\sqrt{m^2+t^2-mt} \quad , \quad \gamma = \tan^{-1}\frac{2t-m}{\sqrt{3}m}. \tag{B.23}$$

Using $J(z)$ and $K(z)$, $I_\theta$ is given by

$$I_\theta = J(z)J(-z)+K(z)K(-z) = -J^2(z)-K^2(z) = 4\pi J_1^2(z), \tag{B.24}$$

where $J_1$ denotes the Bessel function of the first kind,

$$\begin{aligned} J(z) &= \int_0^{2\pi} d\theta \cos\theta \exp\{iz\cos(\theta-\gamma)\} = \int_0^{2\pi} du \cos(u+\gamma)\exp(iz\cos u) \\ &= \int_0^{\pi} du(\cos u\cos\gamma-\sin u\sin\gamma)\exp(iz\cos u) \\ &\quad + \int_\pi^{2\pi} du(\cos u\cos\gamma-\sin u\sin\gamma)\exp(iz\cos u) \\ &= \int_0^{\pi} du\cos u\cos\gamma 2i\sin(z\cos u) - \int_0^{\pi} du\sin u\sin\gamma 2i\sin(z\cos u) \\ &= 2i\cos\gamma\int_0^{\pi} du\cos u\sin(z\cos u) = 2\pi i\cos\gamma J_1^2(z), \end{aligned} \tag{B.25}$$

$$
\begin{aligned}
K(z) &= \int_0^{2\pi} d\theta \sin\theta \exp\{iz\cos(\theta-\gamma)\} = \int_0^{2\pi} du \sin(u+\gamma)\exp(iz\cos u) \\
&= \int_0^{\pi} du(\sin u\cos\gamma+\cos u\sin\gamma)\exp(iz\cos u) \\
&\quad + \int_{\pi}^{2\pi} du(\sin u\cos\gamma+\cos u\sin\gamma)\exp(iz\cos u) \\
&= 2i\cos\gamma\int_0^{\pi} du\sin u\sin(z\cos u)+2i\sin\gamma\int_0^{\pi} du\cos u\sin(z\cos u) \\
&= 2i\sin\gamma\int_0^{\pi} du\cos u\sin(z\cos u) = 2\pi i\sin\gamma J_1^2(z),
\end{aligned} \tag{B.26}
$$

and $u=\theta-\gamma$. Then Eq. (B.21) is written as

$$
\begin{aligned}
E_m &= -\sqrt{3}\pi d M^2 R^2 N_A N_B d \sum_{m=-\infty}^{\infty}{}' \sum_{t=-\infty}^{\infty}{}' \frac{J_1^2(4\pi d\sqrt{m^2+t^2-mt}/\sqrt{3}a)}{m^2+t^2-mt} \\
&\quad \times\left(1-\frac{1-\exp(-4\pi d\sqrt{m^2+t^2-mt}/\sqrt{3}a)}{4\pi d\sqrt{m^2+t^2-mt}/\sqrt{3}a}\right).
\end{aligned} \tag{B.27}
$$

We consider the energy per unit cell $N_A N_B a^2\sqrt{3}/2$, and we obtain

$$
\begin{aligned}
E_{m,unit} &= -2\frac{\pi R^2}{a^2}M^2 d \sum_{m=-\infty}^{\infty}{}' \sum_{t=-\infty}^{\infty}{}' \frac{J_1^2(4\pi d\sqrt{m^2+t^2-mt}/\sqrt{3}a)}{m^2+t^2-mt} \\
&\quad \times\left(1-\frac{1-\exp(-4\pi d\sqrt{m^2+t^2-mt}/\sqrt{3}a)}{4\pi d\sqrt{m^2+t^2-mt}/\sqrt{3}a}\right).
\end{aligned} \tag{B.28}
$$

By the relation

$$
\sum_{m=-\infty}^{\infty}{}' \sum_{t=-\infty}^{\infty}{}' \frac{J_1^2(4\pi d\sqrt{m^2+t^2-mt}/\sqrt{3}a)}{m^2+t^2-mt} = \frac{2\sqrt{3}\pi}{3}(1-\rho_n), \tag{B.29}
$$

where $\rho_n = 2\pi R^2/\sqrt{3}a^2$, finally, we can get

$$
\begin{aligned}
E_{m,unit} &= -2\pi d M^2\rho_n(1-\rho_n) \\
&\quad +2\frac{\pi R^2}{a^2}M^2 d \sum_{m=-\infty}^{\infty}{}' \sum_{t=-\infty}^{\infty}{}' \frac{J_1^2(4\pi d\sqrt{m^2+t^2-mt}/\sqrt{3}a)}{m^2+t^2-mt} \\
&\quad \times\frac{1-\exp(-4\pi d\sqrt{m^2+t^2-mt}/\sqrt{3}a)}{4\pi d\sqrt{m^2+t^2-mt}/\sqrt{3}a}.
\end{aligned} \tag{B.30}
$$

## B.3 Isolated flux tubes

The self- and mutual induction form magnetic energy is expressed

$$\begin{aligned} E_{mag} &= -\frac{1}{2}M^2\sum_{ij}\int_0^d dz\int_0^d dz'\oint ds\oint ds'\frac{\vec{t}_i\cdot\vec{t}_j}{R_{ij}} \\ &= -M^2 d\sum_{ij}\oint ds\oint ds'\vec{t}_i\cdot\vec{t}_j\Phi\left(\frac{R_{ij}}{d}\right), \end{aligned} \tag{B.31}$$

where $\Phi(x)=\sinh^{-1}(1/x)+x-\sqrt{1+x^2}$ and $\vec{t}_i\cdot\vec{t}_j=\cos\theta$.

Using

$$\frac{R_{ij}}{d}=\frac{1}{d}2R\sin(\theta/2)=p\sin\frac{\theta}{2},$$

then

$$\begin{aligned} E_{mag} &= -M^2 d2\pi R^2\int_0^{2\pi}d\theta\left(\sinh^{-1}\frac{1}{p\sin\theta/2}+p\sin\frac{\theta}{2}-\sqrt{1+p^2\sin^2\frac{\theta}{2}}\right)\cos\theta \\ &= -M^2 d2\pi R^2(E_{mag1}+E_{mag2}+E_{mag2}) \end{aligned} \tag{B.32}$$

where $p=2R/d$ is aspect ratio, $ds'=Rd\theta$, and $\oint ds=2\pi R$.

$$\begin{aligned} E_{mag1} &= \int_0^{2\pi}d\theta\cos\theta\sinh^{-1}\frac{1}{p\sin\theta/2} \\ &= \int_0^{2\pi}d\theta\cos\theta\ln\left(\frac{1}{p\sin\theta/2}+\sqrt{\frac{1}{p^2\sin^2\theta/2}+1}\right) \\ &= \int_0^{2\pi}d\theta\cos\theta\left\{-\ln(p)-\ln(\sin\theta/2)+\ln\left(1+\sqrt{1+p^2\sin^2\theta/2}\right)\right\} \\ &= 0+(-\pi)+\left\{-\pi-\frac{4}{p^2}\frac{1}{\sqrt{1-k^2}}E(k)+4\frac{1+p^2}{p^2}\sqrt{1-k^2}K(k)\right\} \\ &= \frac{4}{3}\frac{k}{\sqrt{1-k^2}}\left\{\frac{-3(1-k^2)}{k^3}E(k)+\frac{3(1-k^2)}{k^3}K(k)\right\}, \end{aligned} \tag{B.33}$$

where $k^2\equiv p^2/(1+p^2)$, $K$ and $E$ are, respectively, complete elliptic integrals of the first and second kind.

$$\begin{aligned} E_{mag2} &= \int_0^{2\pi}d\theta p\cos\theta\cdot\sin\frac{\theta}{2}=p\int_0^{2\pi}d\theta\left(2\cos^2\frac{\theta}{2}-1\right)\sin\frac{\theta}{2} \\ &= p\int_0^{\pi}2dy\,2\cos^2 y\sin y-p\int_0^{\pi}2dy\sin y=-\frac{4}{3}p=-\frac{4}{3}\frac{k}{\sqrt{1-k^2}}. \end{aligned} \tag{B.34}$$

$$
\begin{aligned}
E_{mag3} &= -\int_0^{2\pi} d\theta \cos\theta \sqrt{1+p^2\sin^2\frac{\theta}{2}} = -\int_0^{2\pi} d\theta \left(2\cos^2\frac{\theta}{2}-1\right)\sqrt{\frac{1-k^2\cos^2\theta/2}{1-k^2}} \\
&= -\int_{\frac{\pi}{2}}^{-\frac{\pi}{2}} -2dy(2\sin^2 y-1)\sqrt{\frac{1-k^2\sin^2 y}{1-k^2}} \\
&= -4\int_0^{\frac{\pi}{2}} dy(2\sin^2 y-1)\sqrt{\frac{1-k^2\sin^2 y}{1-k^2}} \\
&= \frac{-8}{\sqrt{1-k^2}}\int_0^{\frac{\pi}{2}} dy 2\sin^2 y\sqrt{1-k^2}+\frac{4}{\sqrt{1-k^2}}E(k) \\
&= \frac{1}{\sqrt{1-k^2}}\left\{\frac{-8(1-k^2)}{3k^2}K(k)-\frac{8(2k^2-1)}{3k^2}E(k)+4E(k)\right\}. \qquad \text{(B.35)}
\end{aligned}
$$

Then we obtain

$$
\begin{aligned}
E_{mag} &= -M^2 d 2\pi R^2 \frac{4}{3}\frac{k}{\sqrt{1-k^2}}\left\{-1+\frac{2k^2-1}{k^3}E(k)+\frac{1-k^2}{k^3}K(k)\right\} \\
&= \frac{16\pi}{3}R^3M^2d\left\{1-\frac{1}{k^3}[(2k^2-1)E(K)+(1-k^2)K(k)]\right\}. \qquad \text{(B.36)}
\end{aligned}
$$

# References

## References for Part I


[1] J. K. Furdyna, J. Appl. Phys. **64**, R29(1988).

[2] O. Goede and W. Heimbrodt, Phys. stat. sol. (b) **146**, 11(1988).

[3] M. Z. Cieplak and P. Byszewski, Solid State Commun. **29**, 81(1979).

[4] R. L. Aggarwal, S. N. Jasperson, P. Becla, and R. R. Galazka, Phys. Rev. B**32**, 5132(1985).

[5] O. W. Shih, R. L. Aggarwal, and P. Becla, Phys. Rev. B**46**, 15859(1992).

[6] H. Alawadhi, I. Miotkowski, V. Souw, M. McElfresh, A. K. Ramdas, and S. Miotkowska, Phys. Rev. B**63**, 155201(2001).

[7] M. Haddad, P. Leisching, R. Frey, C. Flytzanis, and J. Cibert, Appl. Phys. Lett. **73**, 1940(1990).

[8] Hong-Zhou Ma, Liang-Yao Chen, Shi-Ming Zhou, Yu-Xiang Zheng, Ya-Dong Wang, You-Hua Qian, and Chen-Jia Chen, Appl. Phys. Lett. **67**, 1665(1995).

[9] S. Hugonnard-Bruyere, C. Buss, R. Frey, and C. Flytzanis, Appl. Phys. Lett. **66**, 2043(1995).

[10] C. Buss, R. Frey, C. Flytzanis, and J. Cibert, Solid State Commun. **94**, 543(1995).

[11] R. Pankoke, C. Buss, S. Hugonnard-Bruyere, P. Leisching, R. Frey, and C. Flytzanis, Appl. Phys. Lett. **68**, 2615(1996).

[12] C. Buss, R. Pankoke, P. Leisching, J. Cibert, R. Frey, and C. Flytzanis, Phys. Rev. Lett. **78**, 4123(1997).

[13] J. A. Kenrow, K. El Sayed, and C. J. Stanton, Phys. Rev. B**58**, R13399(1998).

[14] H. Krenn, W. Zawadzki, and G. Bauer, Phys. Rev. Lett. **55**, 1510(1985).

[15] D. D. Awschalom, J. Warnock, and S. von Molnár, Phys. Rev. Lett. **58**, 812(1987).

[16] H. Krenn, K. Kaltenegger, T. Dietl, J. Spalek, and G. Bauer, Phys. Rev. B**39**, 10918(1989).

[17] T. Kasuya, A. Yanase, and T. Takeda, Solid State Commun. **8**, 1543(1970).

[18] T. Kasuya, A. Yanase, and T. Takeda, Solid State Commun. **8**, 1551(1970).

[19] A. Mauger, Phys. Rev. B**27**, 2308(1983).

[20] S. Takeyama, in "Magneto-Optics", ed. by S. Sugano and N. Kojima, Springer Series in Solid State Science, Vol. **128**, (Springer, Berlin, 2000) p. 179.

[21] T. Wojtowicz, S. Kolesnik, I. Miotkowski, and J. K. Furdyna, Phys. Rev. Lett. **70**, 2317(1993).

[22] R. N. Bicknell, N. C. Giles-Taylor, J. F. Schetzina, N. G. Anderson, and W. D. Laidig, Appl. Phys. Lett. **46**, 238(1985).

[23] E. D. Isaacs, D. Heiman, J. J. Zayhowski, R. N. Bicknell, and J. F. Schetzina, Appl. Phys. Lett. **48**, 275(1986).

[24] S. Colak, J. Khurgin, W. Seemungal, and A. Hebling, J. Appl. Phys. **62**, 2633(1987).

[25] Y. Oka, Solid State Commun. **40**, 778(1998).

[26] Y. Oka, J. Shen, K. Takabayashi, N. Takahashi, H. Mitsu, I. Souma, and R. Pittini, J. Luminescence **83-84**, 83(1999).

[27] R. Pittini, H. Mitsu, M. Takahashi, J. X. Shen, and Y. Oka, J. Appl. Phys. **85**, 5938(1999).

[28] J. X. Shen, Y. Oka, W. Ossau, F. Fischer, A. Waag, and G. Landwehr, J. Appl. Phys. **85**, 5947(1999).

[29] K. Kayanuma, E. Shirado, M. C. Debnath, I. Souma, Z. Chen, and Y. Oka, J. Appl. Phys. **89**, 7278(2001).

[30] N. Takahashi, K. Takabayashi, I. Souma, J. Shen, and Y. Oka, J. Appl. Phys. **87**, 6469(2000).

[31] Z. H. Chen, M. C. Debnath, K. Shibata, T. Saitou, T. Sato, and Y. Oka, J. Appl. Phys. **89**, 6701(2001).

[32] K. Furdyna, J. Kossut, and A. K. Ramdas, in "Optical Properties of Narrow-Gap Low-Dimensional Structures", ed. by C. M. Sotomayor Torres, J. C. Portal, J. C. Maan, and R. A. Stradling, Nato Science Series: B, Vol. **152**, (Plenum Press, New York, 1987) p. 135.

[33] Y. Ohno, D. K. Young, B. Beschoten, F. Matsukura, H. Ohno, and D. D. Awschalom, Nature **402**, 790(1999).

[34] M. Oestreich, J. Hübner, D. Hägele, P. J. Klar, W. Heimbrodt, W. W. Rühle, D. E. Ashenford, and B. Lunn, Appl. Phys. Lett. **74**, 1251(1999).

[35] G. Schmidt and L. W. Molenkamp, J. Appl. Phys. **89**, 7443(2001).

[36] R. R. Galazka, S. Nagata, and P. H. Keesom, Phys. Rev. B**22**, 3344(1980).

[37] J. K. Furdyna, J. Appl. Phys. **53**, 7637(1982).

[38] J. A. Gaj, R. Planel, and G. Fishman, Solid State Commun. **29**, 435(1979).

[39] E. O. Kane, J. Phys. Chem. Solids. **1**, 249(1957).

[40] J. A. Gaj, W. Grieshaber, C. Bodin-Deshayes, J. Cibert, G. Feuillet, Y. Merle d'Aubigné, and A. Wasiela, Phys. Rev. B**50**, 5512(1994).

[41] W. Grieshaber, A. Haury, J. Cibert, Y. Merle d'Aubigné, A. Wasiela, and J. A. Gaj, Phys. Rev. B**53**, 4891(1996).

[42] B. E. Larson, K. C. Hass, H. Ehrenreich, and A. E. Carlsson, Phys. Rev. B**37**, 4137(1988).

[43] M. Ayadi, J. Ferre, A. Mauger, and R. Triboulet, Phys. Rev. Lett. **57**, 1165(1986).

[44] A. Mauger, J. Ferre, M. Ayadi, and P. Nordblad, Phys. Rev. B**37**, 9022(1988).

[45] A. L. Chudnovskiy, R. Oppermann, and B. Rosenow, D. R. Yakovlev, U. Zehnder, and W. Ossau, Phys. Rev. B**55**, 10519(1997).

[46] J. J. Zayhowski, R. N. Kershaw, D. Ridgley, K. Dwight, A. Wold, R. R. Galazka, and W. Giriat, Phys. Rev. B**35**, 6950(1987).

[47] G. Mackh, W. Ossau, D. R. Yakovlev, A. Waag, G. Landwehr, R. Hellmann, and E. O. Göbel, Phys. Rev. B**49**, 10248(1994).

[48] W. E. Hagston, T. Stirner, and J. Miao, J. Appl. Phys. **82**, 5653(1997).

[49] K. V. Kavokin, I. A. Merkulov, D. R. Yakovlev, W. Ossau, and G. Landwehr, Phys. Rev. B**60**, 16499(1999).

[50] M. Umehara, Phys. Rev. B**61**, 12209(2000).

[51] M. Umehara, Phys. Rev. B**67**, 035201(2003).

[52] M. Umehara, Phys. Rev. B**68**, 193202(2003).

[53] D. Heiman, P. Becla, R. Kershaw, D. Ridgley, K. Dwight, A. Wold, and R. R. Galazka, Phys. Rev. B**34**, 3961(1986).

[54] S. Takeyama, S. Adachi, Y. Takagi, and V. F. Aguekian, Jpn. J. Appl. Phys. **32**, Suppl. **32-3**, 425(1993).

[55] A. Golnic, J. Ginter, and J. A. Gaj, J. Phys. C:Solid State Phys. **16**, 6073(1983).

[56] P. A. Wolff and J. Warnock, J. Appl. Phys. **55**, 2300(1984).

[57] T. H. Nhung, R. Planel, C. Benoit à la Guillaume, and A. K. Bhattacharjee, Phys. Rev. B**31**, 2388(1985).

[58] J. Warnock and P. A. Wolff, Phys. Rev. B**31**, 6579(1985).

[59] R. Planel, J. Cernogora, J. Gaj, and C. Benoit à la Guillaume, in Proc. 17th Int. Conf. on the Physics of Semiconductors, San Francisco, 1984, ed. by J. D. Chadi and W. A. Harrison, (Springer-Verlag, New York, 1985), p. 1411.

[60] L. R. Ram-Mohan and P. A. Wolff, Phys. Rev. B**38**, 1330(1988).

[61] M. Bugajski, P. Becla, P. A. Wolff, D. Heiman, and L. R. Ram-Mohan, Phys. Rev. B**38**, 10512(1988).

[62] E. Molva and L. S. Dang, Phys. Rev. B**27**, 6222(1983).

[63] E. Molva and L. S. Dang, Phys. Rev. B**32**, 1156(1985).

[64] P. J. Dean and D. C. Herbert, in "Excitons", ed. by K. Cho, Topics in Current Physics, Vol. **14**, (Springer-Verlag, Berlin; New York, 1979), Chap. 3, p. 55.

[65] A. M. White, I. Hinchliffe, P. J. Dean, and P. D. Greene, Solid State Commun. **10**, 497(1972).

[66] W. Rühle and D. Bimberg, Phys. Rev. B**12**, 2382(1975).

[67] W. Schairer, D. Bimberg, W. Kottler, K. Cho, and M. Schmidt, Phys. Rev. B**13**, 3452(1976).

[68] P. J. Dean, H. Venghaus, J. C. Pfister, B. Schaub, and J. Marine, J. Lumin. **16**, 363(1978).

[69] A. M. White, P. J. Dean, and B. Day, J. Phys. C**7**, 1400(1974).

[70] M. Schmidt, T. N. Morgan, and W. Schairer, Phys. Rev. B**11**, 5002(1975).

[71] H. Mathieu, J. Camassel, and F. Ben Chekroun, Phys. Rev. B**29**, 3438(1984).

[72] A. K. Bhattacharjee, R. Planel and C. Bonoit à la Guillaume, in Proc. 17th Int. Conf. on the Physics of Semiconductors, San Francisco, 1984, ed. by J. D. Chadi and W. A. Harrison, (Springer-Verlag, New York, 1985), p. 1431.

[73] J. Mycielski and C. Rigaux, J. Physique **44**, 1041(1983).

[74] A. K. Bhattacharjee, Phys. Rev. B**58**, 15660(1998).

[75] D. Ouadjaout and Y. Marfaing, Phys. Rev. B**41**, 12096(1990).

[76] S. K. Lyo, Phys. Rev. B**48**, 2152(1993).

[77] S. Takeyama, S. Adachi, Y. Takagi, and V. F. Aguekian, Phys. Rev. B**51**, 4858(1995).

[78] S. Takeyama, S. Adachi, Y. Takagi, and V. F. Aguekian, Phys. Rev. B**52**, 1444(1995).

[79] R. Hellmann, A. Euteneuer, S. G. Hense, J. Feldmann, P. Thomas, E. O. Göbel, D. R. Yakovlev, A. Waag, and G. Landwehr, Phys. Rev. B**51**, 18053(1995).

[80] T. Itoh and E. Komatsu, J. Luminescence **38**, 266(1987).

[81] V. Y. Ivanov, Y. G. Semenov, M. Surma, and M. Godlewski, Phys. Rev. B**54**, 4696(1996).

[82] W. Heimbrodt, M. Happ, and F. Henneberger, Phys. Rev. B**60**, R16326(1999).

[83] J. X. Shen, R. Pittini, and Y. Oka, Phys. Rev. B**64**, 195321(2001).

# References for Part II

[84] "Superconductivity", ed. by R. D. Parks, (Marcel Dekker, New York, 1969).

[85] "Magnetic Flux Structures in Superconductors", R. P. Huebener, Springer Series in Solid State Science, Vol. 6, (Springer-Verlag, New York, 2001).

[86] D. E. Chimenti and R. P. Huebener, Solid State Commun. **21**, 467(1977).

[87] W. H. Fietz, J. Parisi, and R. P. Hubener, J. Low Temp. Phys. **54**, 159(1984).

[88] J. Parisi, B. Mühlemeier, R. P. Huebener, and W. Buck, J. Low Temp. Phys. **60**, 45(1985).

[89] M. R. Freeman, Phys. Rev. Lett. **69**, 1691(1992).

[90] J. C. Osborn and A. T. Dorsey, Phys. Rev. B**50**, 15961(1994).

[91] "Superconductivity of metals and alloys", P. G. de Gennes, Frontiers in Physics, (W. A. Benjamin, New York, 1966).

[92] R. E. Goldstein, D. P. Jackson, and A. T. Dorsey, Phys. Rev. Lett. **76**, 3818(1996).

[93] S. A. Langer, R. E. Goldstein, and D. P. Jackson, Phys. Rev. A**46**, 4894(1992).

[94] Kwok-On Ng and David Vanderbilt, Phys. Rev. B**52**, 2177(1995).

[95] A. T. Dorsey and R. E. Goldstein, Phys. Rev. B**57**, 3058(1998).

[96] C. R. Reisin and S. G. Lipson, Phys. Rev. B**61**, 4251(2000).

[97] C. Gourdon, G. Lazard, V. Jeudy, C. Testelin, E. L. Ivchenko, and G. Karczewski, Solid State Commun. **123**, 299(2002).

[98] C. Gourdon, V. Jeudy, M. Menant, Le Anh Tu, E. L. Ivchenko, and G. Karczewski, Appl. Phys. Lett. **82**, 230(2003).

[99] L. D. Landau, Phys. Z. Sowjet, **11**, 129(1937).

[100] R. N. Goren and M. Tinkham, J. Low Temp. Phys. **5**, 465(1971).

[101] "Introduction to Superconductivity", M. Tinkham, International Series in Pure and Applied Physics, (McGraw-Hill, New York, 1975).

[102] "Normal state bubbles and lamellae in type-I superconductors.", A. Cebers, C. Gourdon, V. Jeudy, and T. Okada, submitted to Phys. Rev. B.

[103] M. R. Koblischka and R. J. Wijngaarden, Supercond. Sci. Technol. **8**, 199(1995).

[104] P. E. Goa, H. Hauglin, M. Baziljevich, E. Il'yashenko, P. L. Gammel, and T. H. Johansen, Supercond. Sci. Technol. **14**, 729(2001).

[105] M. A. Butler, S. J. Martin, and R. J. Baughman, Appl. Phys. Lett. **49**, 1053(1986).

[106] D. Scalbert, J. Cernogora, and C. Benoit à la Guillaume, Solid State Commun. **66**, 571(1988).

[107] V. Jeudy, G. Jung, D. Limagne, and G. Waysand, Physica C**225**, 331(1994).

[108] V. Jeudy, C. Gourdon, G. Karczewski, and Le Anh Tu, Physica C**388-389**, 775(2003).

[109] R. Plass, N. C. Bartelt, and G. L. Lellogg, J. Phys.: Condens. Matter **14**, 4227(2002).

[110] Chin-Yih Hong, I. J. Jang, H. E. Horng, C. J. Hsu, Y. D. Yao, and H. C. Yang, J. Appl. Phys. **81**, 4275(1997).

[111] V. Jeudy, C. Gourdon, and T. Okada, Phys. Rev. Lett. **92**, 147001(2004).

[112] R. P. Huebener, R. T. Kampwirth, and V. A. Rowe, Cryogenics **12**, 100(1972).

[113] R. P. Huebener and R. T. Kampwirth, Phys. Stat. Sol. (a) **13**, 255(1972).

[114] D. E. Farrell, R. P. Huebener, and R. T. Kampwirth, J. Low Temp. Phys. **19**, 99(1975).

# Publications

[1] Anti-Stokes luminescence of magnetic polarons in CdMnTe. [T. Okada and T. Itoh: Proceedings of the 26th International Conference on the Physics of Semiconductors, Institute of Physics Conference Series Number171, H240 (2002)].

[2] Impeded growth of magnetic flux bubbles in the intermediate state pattern of type I superconductors. [V. Jeudy, C. Gourdon, and T. Okada: Phys. Rev. Lett. 92, 147001 (2004)].

[3] Normal state bubbles and lamellae in type I superconductors. [A. Cebers, C. Gourdon, V. Jeudy, and T. Okada: submitted to Phys. Rev. B].

[4] New spin-related optical phenomena in semimagnetic semiconductors of $Cd_{1-x}Mn_xTe$. [T. Okada and T. Itoh: in preparation].

# Related papers

[1] Magneto-photoluminescence of novel magnetic semiconductor $Zn_{1-x}Cr_xO$ grown by PLD method. [Issei Satoh, Takeshi Kobayashi, Kouichi Katayama, Takanori Okada, and Tadashi Itoh: Appl. Phys. A 00. 1-3(2004)].

# International conferences

[1] Anti-Stokes luminescence of magnetic polarons in CdMnTe. [T. Okada and T. Itoh: 26th International Conference on the Physics of Semiconductors (Edinburgh, 29 July - 2 August 2002)].

[2] PLD growth of novel magnetic semiconductor $Zn_{1-x}Cr_xO$ and its opto-spintronic properties. [Issei Satoh, Takeshi Kobayashi, Takanori Okada, Tadashi Itoh, Teruo Ono and Saburo Nasu: 2002 Materials Research Society Fall Meeting (Boston, 2002)].

[3] Magneto-photoluminescence of $Zn_{1-x}Cr_xO$: Comparison of experiments and simulation. [Issei Satoh, Takeshi Kobayashi, Takanori Okada and Tadashi Itoh: The Int. Symp. Carrier Interactions and Spintronics in Nanostructures (Kanagawa, 2003)].

[4] Magneto-photoluminescence of novel magnetic semiconductor $Zn_{1-x}Cr_xO$ grown by PLD method. [Issei Satoh, Takeshi Kobayashi, Kouichi Katayama, Takanori Okada and Tadashi Itoh:The 7th Int. Conf. on Laser Ablation (Crete, 2003)].

[5] Faraday microscopy with semimagnetic semiconductor quantum well sensor. [T. Okada, C. Gourdon, V. Jeudy, and T. Itoh: International Workshop on Materials Science and Nano-Engineering (Osaka, 11 - 14 December 2004)].